Yielding Transitions in Amorphous Materials

COCHRAN, JAMES,OLIVER

Yielding Transitions in Amorphous Materials

James Oliver Cochran

Submitted for the degree of Doctor of Philosophy

January 2023

Abstract: Amorphous materials form a part of a wide array of common materials, including foams, emulsions, colloidal and metallic glasses and polymeric systems. Many amorphous materials exhibit yielding transitions from a solid-like to a fluid-like state under shear, and characterising and predicting these transitions is of key importance in a variety of industrial and biological applications. We study the yielding of amorphous materials in three separate studies.

First, we use a thermal fluidity model to explore the yielding transitions of an amorphous material under a shear startup protocol and categorise the yielding transitions as either brittle or ductile. We find that ductile and brittle yielding both occur in systems with a stress overshoot as a function of strain, with no need for an overhang, in contrast to recent claims in the literature.

Second, we use the Soft Glassy Rheology (SGR) model and a thermal elastoplastic model (EPM) to study slow fatigue followed by sudden catastrophic failure of amorphous materials subjected to a large amplitude oscillatory shear strain protocol. We find that both models display delayed yielding, in which there is a significant stress drop after many cycles. We fit the number of cycles before yielding to functions of the relevant physical parameters. In the SGR model, we find a critical amplitude below which the yielding is delayed but insignificant, and in the EPM we find a temperature-dependant critical amplitude at which the yielding cycle diverges.

Third, we attempt to derive a continuum model of epithelial tissue rheology. We present several model variants, and compare them to published Self-Propelled Voronoi (SPV) model simulations of epithelial rheology. While we are unable to derive a model that fully captures all of the features seen in the SPV Model, we do identify several necessary ingredients of an eventual successful model.

Yielding Transitions in Amorphous Materials

James Oliver Cochran

A Thesis presented for the degree of
Doctor of Philosophy

Supervised by Prof. Suzanne Fielding
Department of Physics
Durham University
United Kingdom

January 2023

Contents

Abstract **i**

Publications **xvii**

1 Introduction **1**

1.1 Layout of Thesis 3

1.1.1 Background 3

1.1.2 Ductile and Brittle Yielding in Soft Glassy Materials . . . 4

1.1.3 Delayed Yielding in the SGR Model in LAOS 5

1.1.4 Delayed Yielding in an EPM Under LAOS 6

1.1.5 Shape Driven Rigidity Transitions in Epithelial Tissue . . . 6

1.1.6 Conclusion 7

2 Background **9**

2.1 Stress and Strain 10

2.1.1 Strain and Strain Rate Tensors 10

2.1.2 Stress Tensor 15

2.2 Rheology 17

2.2.1 Rheometer Geometry 17

2.2.2 Flow Curves 19
2.2.3 Shear Startup 21
2.2.4 Lissajous Figures 22
2.3 Shear Banding 24
2.4 Methodology 27
2.5 Conclusion 29

3 Ductile and Brittle Yielding in Soft Glassy Materials 31

3.1 Introduction 31
3.2 Model 33
3.3 Shear Protocol 35
3.4 Results 36
3.4.1 Homogeneous Dynamics 36
3.4.2 Linear Stability Analysis 40
3.4.3 Non-Linear Simulations 46
3.5 Discussion 56
3.6 Conclusion 58

4 Delayed Yielding in the SGR Model in LAOS 61

4.1 Introduction 61
4.2 Model 63
4.3 Shear Protocol 69
4.4 Results 71
4.5 Discussion 80
4.6 Conclusion 85

5 Delayed Yielding in an EPM Under LAOS 89

5.1 Introduction 89

5.2 Model 90

5.3 Results 93

5.3.1 Athermal Limit 98

5.4 Discussion 101

5.5 Conclusion 104

6 Shape Driven Rigidity Transitions in Epithelial Tissue 107

6.1 Introduction 107

6.2 Self Propelled Voronoi Model 110

6.2.1 Model 111

6.2.2 Results 113

6.3 Continuum Model 117

6.3.1 Simple Mean Field Model 121

6.3.2 Modified Elastic Modulus 128

6.3.3 Fixing Cell Area 130

6.3.4 Solid Phase Shape Deviations 132

6.3.5 Cellular Tilt 135

6.3.6 Dynamic Fluidity 142

6.4 Conclusion 148

7 Conclusions 153

7.1 Ductile and Brittle Yielding in Soft Glassy Materials 154

7.2 Delayed Yielding in the SGR Model in LAOS 156

7.3 Delayed Yielding in an EPM Under LAOS 157

7.4 Shape Driven Rigidity Transitions in Epithelial Tissue 158

7.5 Closing Remarks 161

Bibliography **163**

Declaration

The work in this thesis is based on research carried out under the supervision of Prof. Suzanne Fielding in the Department of Physics at Durham University. No part of this thesis has been submitted elsewhere for any degree or qualification.

Acknowledgements

Firstly, I am extremely grateful to Suzanne Fielding for her help, guidance and encouragement throughout my PhD. Her insightful and methodical research style has had a profound influence on the development of my own research skills and scientific problem solving. Under her supervision, I have grown significantly as a scientist, both in my ability to carry out investigations and in the ways in which I interact with the wider scientific community. I am also grateful to Dr Hugh Barlow, who provided a great deal of help and support during the first year of my doctorate, as well as Hal Endersby for the helpful discussions in the latter half. I also wish to thank Cristina Marchetti, Max Bi and Junxiang Huang, with whom I collaborated closely for an extended period while working on tissue rheology. My thanks also go to Peter Sollich and Jack Parley for a briefer but very fruitful collaboration.

My doctoral programme was funded by the SOFI CDT, which has also been an exceptional source of help and support throughout. The professional help and guidance provided during the early stages of my studies were influential in directing me towards the field of research I am now in, and the continual organisation of academic events have helped to provide me with an invaluable network of peers and research colleagues throughout my studies. For this I am extremely grateful to Lian Hutchings, Richard Thompson and the rest of the SOFI team. I am also extremely grateful to all of cohort 5, who have supported me throughout, professionally and personally, and without whom my PhD experience would have been very different.

I would like to thank all of the friends who have been continually alongside me throughout my studies. I first thank all the people at St. Nics for their friendship and

support over the last few years. They have supported and encouraged me throughout, and on occasion provided much needed distractions from my studies. I also wish to thank the many friends who have made the last few years an unforgettable time, including those from the Hillwalking society and from Cuth's, and especially the pool D team.

Finally, I wish to thank my family, who have been there for me continually, for all their care and support. Their encouragement not only during my doctoral studies but throughout my academic studies has been pivotal in my development as a scientist.

The work in this thesis was funded by the Soft Matter and Functional Interfaces Centre for Doctoral Training (EP/L015536/1).

But let justice flow like a river, and let goodness flow like a stream that never stops.

— *Amos 5:24*, NCV

Dedicated to

my family, without whose
persistent support this would not
have been possible.

Publications

H. J. Barlow, **J. O. Cochran** and S. M. Fielding, *Ductile and brittle yielding in thermal and athermal amorphous materials.* Physical Review Letters **125** (Oct, 2020).

J. Huang, **J. O. Cochran**, S. M. Fielding, M. C. Marchetti and D. Bi, *Shear-driven solidification and nonlinear elasticity in epithelial tissues.* Physical Review Letters **128** (Apr, 2022).

Manuscripts in Preparation

S. M. Fielding, **J. O. Cochran**, J. Huang, D. Bi and M. C. Marchetti, *Constitutive model for the rheology of biological tissue.*

J. O. Cochran, G. L. Callaghan, M. J. G. Caven and S. M. Fielding, *Slow fatigue and highly delayed yielding via shear banding in oscillatory shear.*

Chapter 1

Introduction

The world around us contains many materials that look or feel solid, and yet still change shape and deform over a broad range of length and timescales. Foodstuffs such as ketchup and mayonnaise can sit in apparently solid lumps, and yet flow out of their bottle with enough force, and flow to fill a container given enough time [1, 2]. Countless objects around us are made of plastic, which behaves as a solid under the right circumstances, and yet can deform, flow and slowly change shape or rupture suddenly and catastrophically [3]. In the biological world, the multicellular tissue that makes up plants and animals is normally solid, and yet during wound healing and embryonic growth it morphs and flows into a new shape [4–7].

All of the materials listed above are unified by the fact they have an amorphous microstructure: instead of forming crystalline structures over a regular lattice, they consist of a disordered arrangement of constituents. For example, emulsions such as mayonnaise comprise small droplets of one material embedded in a continuous background of another, which are randomly placed with no apparent spatial structure [8]. Polymeric systems such as plastics have long, chain-like molecules, which wrap around each other and tangle [3]. This amorphous structure leads to a wide variety of material responses to an applied deformation or load, as the substructure is able to rearrange and respond in a complicated way. Rheology is the study of how materials deform and flow, and the rheology of amorphous materials reveals a rich array of

phenomena and complex flows.

Many amorphous materials have multiple qualitatively distinct states or behaviours, which can be described as solid-like and fluid-like [9]. It is common for amorphous materials to display yielding transitions following the application of a deformation or load, in which they transition from a solid-like to a fluid-like state. These transitions can take a variety of formats, and are an essential part of understanding the behaviour of a material. Experiments applying a shear protocol to bentonite suspensions [10], microgels [11–13], fuel slurries [14], foams [15–17], emulsions [18–20] and attractive gels [21, 22] have revealed a transition from an initial, solid-like regime, in which stress is proportional to strain to a fluid-like regime at higher stress or strain, in which the stress is extremely non-linear in strain, and typically related instead to the strain rate. In strain-controlled protocols, this is often associated with a stress overshoot, so that there is a relaxation of stress as the system approaches its steady state [10, 15, 18, 21, 22].

The physical origin of yielding transitions has been connected with a variety of microscopic phenomena [9]. In colloidal suspensions and polymer melts, the system often has a characteristic relaxation timescale over which it is able to locally relax stress [23–27]. If a deformation is applied on a shorter timescale than the relaxation time, the system is unable to reconfigure to relax stress and flow, and so behaves in a solid-like way. If, in contrast, the applied deformation is slow compared to the relaxation time, the system is able to relax stress and flow in a fluid-like way. In foams, emulsions and colloidal suspensions with a sufficiently high packing fraction, solid behaviour at low load or deformation emerges because the particles are in contact with each other and jammed, so that they cannot move past each other [28–34]. When a stress or strain is applied to the system, this therefore deforms the particles, and their elastic response generates system-wide solid-like behaviour. At larger load or deformation, the particles rearrange locally in a way that relaxes stress, and if this happens sufficiently fast, fluid-like behaviour emerges.

In this work, we consider several different models of amorphous materials, which

are designed to capture the behaviour of a variety of systems, including foams, emulsions, metallic glasses, gels, colloidal glasses [35–39] and organic tissue [40, 41]. We will also consider the predictions of these models in several different commonly studied rheological protocols. We will find various different types of yielding transitions throughout, and will explore the nature of these transitions and the situations in which they occur.

1.1 Layout of Thesis

The work in this thesis consists of three separate investigations; two of them are contained in their own results chapters, and the third is split into two chapters. These chapters are presented after an initial background chapter to introduce some basic concepts. The thesis then has a final conclusions chapter, summarising the work, and suggesting further avenues for future study.

1.1.1 Background

In Ch. 2, we introduce the basic concepts needed for the rest of this thesis. We start by defining stress and strain, which are used throughout to measure applied force and deformation, and we show how to describe the total stress and strain on a material using the stress and strain tensors. We also consider some basic rheological protocols, which will be used throughout this thesis.

Next, we consider the methods that allow us to measure and characterise rheological behaviour. This includes a discussion of the experimental methods used in rheometry and some common rheometer geometries. We also describe a number of common shear protocols and the associated behaviour of some common classes of materials under these protocols.

Following this, we introduce the phenomenon of shear banding, which is crucial to much of the work in this thesis. We explain how it arises, and deduce some

common associated material responses.

Finally, we provide details of some of the computational methods that we will employ to simulate the rheological constitutive models used in this thesis. This focusses on the Runge-Kutta method and the Crank-Nicolson algorithm.

1.1.2 Ductile and Brittle Yielding in Soft Glassy Materials

A class of amorphous materials known as yield stress fluids behave in a solid-like way at low deformation or applied stress, but flow in a fluid-like when subject to larger deformations or a stronger applied stresses [42]. These materials therefore exhibit a yielding transition under shear, from an initially solid-like to a finally fluid-like state. The nature of this transition can have a sensitive dependence on the material's history before the application of shear [35, 38, 43]. The transition can be smooth and gradual, in which case we refer to it as "ductile", or it can be sudden and catastrophic, in which case we refer to it as "brittle" [44]. In Ch. 3, we use a continuum thermal fluidity model to consider this yielding transition, exploring its predictions for a shear startup protocol.

Recent studies have proposed that ductile and brittle yielding are separated by a qualitative change in a system's behaviour [43, 45]. In particular, Ref. [43] proposes that brittle yielding occurs when the shear startup curve displays an overhang in the stress as a function of strain, while ductile yielding occurs when there is merely an overshoot. We challenge this conclusion for thermal materials, and propose that ductile and brittle yielding both occur in systems with a stress overshoot, with no need for an overhang. Rather, we find that brittle yielding is caused by a shear banding instability, which causes the system to fluidise very rapidly when there is a large stress drop from the peak of the stress overshoot to the steady state. This allows us to draw a quantitative distinction between ductile and brittle yielding, and reveals that brittle yielding typically happens in systems that have been more strongly annealed prior to shear, and at lower strain rates.

1.1.3 Delayed Yielding in the Soft Glassy Rheology Model in Large Amplitude Oscillatory Shear

There is a great deal of evidence that solids, when subjected to cyclic loading, can very slowly accumulate fatigue over many loading cycles, before eventually failing catastrophically in a single cycle [46–50]. There have also been many experimental and theoretical studies into soft and amorphous materials under cyclic loading, which have revealed that many such materials likewise display a solid to fluid transition under cyclic loading, and that this can occur after many cycles [51–66]. What has been less well studied in amorphous materials is the number of deformation cycles that occur before this transition, how this depends on the relevant physical parameters, and the mechanism by which fatigue slowly accumulates and the material eventually yields.

In Ch 4, we study the Soft Glassy Rheology model under a Large Amplitude Oscillatory Shear (LAOS) Strain protocol to explore this phenomenon theoretically. We find that the number of cycles before a sample yields follows a power law in the degree to which the system is annealed prior to shear, as quantified by an ageing time. We also find that the number of cycles before yielding increases as the strain amplitude decreases, and this trend in principle continues down to zero amplitude. However, we also find that the magnitude of the stress drop associated with the yielding event drops to a very small value below a critical strain amplitude, so although in principle we find a very delayed yielding event at low amplitude, in practice we do not characterise it as *significant* delayed yielding.

We also find that prior to the yielding event, strain heterogeneity very slowly grows within the sample, which causes slow fatigue. Any significant yielding event is then associated with a pronounced shear banding instability: strong strain localisation arises and a shear band forms over the course of a few strain cycles. We additionally find that the transition to a fluid-like state is closely associated with the system being rejuvenated by the applied shear, which reverses the initial ageing.

1.1.4 Delayed Yielding in an Elastoplastic Model Under Large Amplitude Oscillatory Shear

To further improve our confidence and understanding of the results in Ch. 4, we explore the same phenomena within a simpler model in Ch. 5. We consider a thermal elastoplastic model which does not show ageing, and is instead annealed by equilibrating at a pre-quench temperature, before instantaneously quenching the system to a working temperature immediately before the imposition of shear strain. We again consider the predictions of the model in a LAOS Strain protocol.

We again find significantly delayed yielding effects. In particular, we show that the number of cycles before yielding can be fit to the exponentiated reciprocal of both the pre-quench temperature and the working temperature. We also find that the number of cycles before yielding is a decreasing function of increasing strain amplitude, γ_0. As γ_0 is reduced, we now find that N^* diverges at a finite critical amplitude, which depends on both the working temperature and the pre-quench temperature. We find that the yielding event in this model is again closely related to a shear banding instability, which grows dramatically over a few cycles as the sample yields, after a very slow accumulation of heterogeneity during the pre-failure regime.

1.1.5 Shape Driven Rigidity Transitions in Epithelial Tissue

The rheology of biological tissue is currently the subject of intense study, both theoretically and experimentally [5, 67–76]. Epithelial tissue is an important type of multicellular tissue which is found in animals, and consists of flat layers of cells, which in simple epithelial tissue exist as monolayers [7, 77]. The cells in these monolayers are almost space filling, and so form a collection of polygons. Epithelial tissue has a variety of interesting mechanical behaviours, due to its roles in wound healing,

tissue growth and organ protection [4–7, 77, 78]. Experimental study has revealed that in many situations, epithelial tissue behaves in a solid-like manner, and can provide a protective layer around organs. However, under certain conditions, the tissue needs to deform and reshape, particularly during embryo growth, or to repair damage to a tissue's structure. Growing evidence suggests that this is possible due to a spontaneous fluidity transition, which allows the tissue to behave in a more fluid-like manner for a period of time [67–72].

Epithelial tissue is commonly modelled theoretically using a Vertex Model [41, 74, 79–82], in which a monolayer of cells is represented by an ensemble of confluent polygons with no gaps between them. This approach has been successful at capturing the solid-fluid transition, as well as several other experimentally observed behaviours. However, it is computationally expensive, and the size of the system that can be modelled with this approach is therefore limited. There have therefore been some recent attempts to derive continuum models that capture the rheology of epithelial tissue [40, 83, 84], with the aim of applying these to explore phenomena that happen on longer length scales, such as shear banding effects.

In Ch. 6, we attempt to derive one such continuum model, aimed at capturing a selection of rheological behaviours seen in the Self-Propelled Voronoi (SPV) Model [41]. We present a number of different continuum model versions, of increasing complexity, which have varying degrees of success in capturing the desired behaviour. We have not been able to develop a final model that provides a good match to the SPV Model in all situations, but our findings represent good progress in that direction, and suggest a list of ingredients that are necessary in a successful model.

1.1.6 Conclusion

In Ch. 7, we summarise the key findings from each of our results chapters and consider the features which unify them. We also propose some potential avenues of future investigation to better understand the phenomena we have explored. This

includes some suggestion for future theoretical work, aimed at building on the results presented in this thesis. It also includes suggestions for experimental work, much of which relates to testable predictions that follow from this research.

Chapter 2

Background

In this thesis, we will consider several rheological constitutive models, which are applicable to a wide range of soft matter systems. We will also consider a range of deformation and flow protocols. However, each chapter is unified by two overarching themes: the first is that we consider the *rheology* of these systems, and the second is that we analyse *yielding transitions*, which represent a subset of rheological phenomena. Rheology refers to the study of deformation and flow, and involves studying how a material responds to the application of an applied stress or strain [85]. Yielding transitions arise when a material changes from having a solid-like response to a fluid-like response, following the imposition of a suitable deformation or stress [86].

In this chapter, we will discuss some of the underlying concepts behind both of these principles, and provide further context and definitions for the phenomena that we will explore. We start by introducing a range of important rheological behaviours, and consider some familiar materials under common protocols. We will then consider some important internal effects that arise in soft matter systems in general, and that will apply to the work presented later. Finally, we will lay out some of the basic computational principles that allow us to carry out the simulations presented in this thesis.

2.1 Stress and Strain

When considering the flow properties of a material, strain is the metric of deformation and stress is the metric of force. Strain is defined as the material's deformation in a given direction normalised by the material's size in a given direction [87, 88],

$$\gamma = \frac{\Delta x}{L}, \tag{2.1}$$

with Δx the deformation and L the material size. If Δx and L are parallel, the strain is called an extensional strain, and if they are perpendicular, it is a shear strain. We will explore this further below. The stress is the force applied to the material divided by cross sectional area [88–90],

$$\Sigma = \frac{F}{A}, \tag{2.2}$$

with F the applied force and A the cross sectional area. If the force acts perpendicular to the plane of the area, it is a normal stress, and if it acts within the plane, it is a shear stress.

2.1.1 Strain and Strain Rate Tensors

To consider strain, we start by considering a 3D material undergoing deformation. A point in the material that starts at position $\mathbf{r}$ will be moved to position $\mathbf{r}'$ by this strain. This can be described by a deformation tensor E_{ij} such that

$$r'_i = E_{ij} r_j, \tag{2.3}$$

where subscripts denote basis directions and repeated indices are summed over. For a small deformation, this generates a displacement $u_i = r'_i - r_i$, and the deformation tensor can be written as [91]

$$E_{ij} = \delta_{ij} + \gamma_{ij}, \tag{2.4}$$

with δ_{ij} the Dirac delta function and

$$\gamma_{ij} = \nabla_j u_i \tag{2.5}$$

the strain tensor. For a small region of material, each element of the strain tensor now describes the deformation in the j-direction of one edge of the region with respect to the opposite edge divided by the size of the region in i-direction, which is exactly the strain as written in Eq. 2.1. We now consider a time-dependent strain, which will generate a velocity field across the sample, given by

$$\mathbf{v}(\mathbf{r}) \equiv \partial_t \mathbf{u}. \tag{2.6}$$

We can then define a velocity gradient tensor,

$$\dot{\gamma}_{ij} = \nabla_j v_i = \partial_t \gamma_{ij}, \tag{2.7}$$

which is exactly the strain rate at any location in the sample, and is given in full as [92, 93]

$$\dot{\gamma}_{ij} = \begin{bmatrix} \frac{\partial v_x}{\partial x} & \frac{\partial v_x}{\partial y} & \frac{\partial v_x}{\partial z} \\ \frac{\partial v_y}{\partial x} & \frac{\partial v_y}{\partial y} & \frac{\partial v_y}{\partial z} \\ \frac{\partial v_z}{\partial x} & \frac{\partial v_z}{\partial y} & \frac{\partial v_z}{\partial z} \end{bmatrix}. \tag{2.8}$$

The diagonal components now describe normal strain, while the off diagonal elements describe shear strain. Fig. 2.1 shows a sketch of a material sample with the effect of two of these elements labelled, one diagonal and one off diagonal. We now consider a small strain increment, $\dot{\gamma}_{ij}\delta t$, which will generate a deformation given by

$$r_i(t + \delta t) = \left(\delta_{ij} + \dot{\gamma}_{ij}\delta t\right) r_j(t). \tag{2.9}$$

Let the time dependent deformation tensor $E_{ij}(t)$ describe deformation from time 0 to time t, then we have that

$$\begin{aligned} E_{ik}(t + \delta t)\, r_k(0) &= \left(\delta_{ij} + \dot{\gamma}_{ij}\delta t\right) E_{jk}(t)\, r_k(0) \\ \frac{E_{ik}(t + \delta t) - E_{ik}(t)}{\delta t} &= \dot{\gamma}_{ij} E_{jk}(t), \end{aligned} \tag{2.10}$$

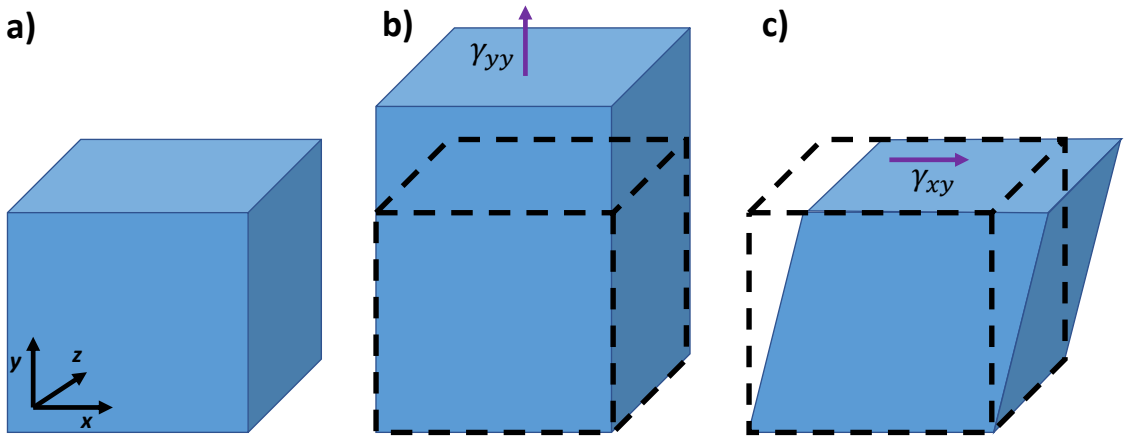

Figure 2.1: A sketch of a sample of material, showing **a)** the original shape, **b)** an extensional strain (which does not preserve volume) and **c)** a shear strain. Black dotted lines show the original shape.

and taking the limit as δt goes to zero,

$$\frac{\partial E_{ij}}{\partial t} = \dot{\gamma}_{ik} E_{kj}. \tag{2.11}$$

All the materials considered in this work are incompressible which means that all strains must preserve the volume. This requires that

$$\nabla \cdot \mathbf{v} = 0, \tag{2.12}$$

and restricts the strain rate tensor to be traceless. The strain rate tensor can be decomposed into a symmetric part, e_{ij} and an anti-symmetric part, which we call the vorticity, ω_{ij}:

$$\begin{aligned} e_{ij} =& \frac{1}{2}\left(\nabla_j v_i + \nabla_i v_j\right), \\ \omega_{ij} =& \frac{1}{2}\left(\nabla_j v_i - \nabla_i v_j\right), \end{aligned} \tag{2.13}$$

so that $\dot{\gamma}_{ij} = e_{ij} + \omega_{ij}$. We further decompose the symmetric part into a deviatoric part

$$d_{ij} = e_{ij} - \frac{1}{D}\nabla_k v_k \delta_{ij}, \tag{2.14}$$

with D the dimension of the tensor, and a compressional term $\frac{1}{D}\nabla_k v_k \delta_{ij}$, and note that for an incompressible material, the compressional term is zero and $e_{ij} = d_{ij}$.

One common deformational mode corresponds to the situation with no vorticity, and is referred to as pure shear. We forbid vorticity by setting

$$\nabla \times \mathbf{v} = \mathbf{0}, \tag{2.15}$$

which constrains the strain rate tensor to be symmetric. The resultant strain rate tensor is traceless and symmetric, and so for any such strain rate tensor, an appropriate change of bases will transform it into a diagonal traceless matrix, and we now work in the basis in which it is diagonal. The strain rate tensor then takes the form

$$\dot{\gamma}_{ij} = \begin{bmatrix} \dot{\gamma}_x & 0 & 0 \\ 0 & \dot{\gamma}_y & 0 \\ 0 & 0 & -\left(\dot{\gamma}_x + \dot{\gamma}_y\right) \end{bmatrix}, \tag{2.16}$$

with $\dot{\gamma}_x$ and $\dot{\gamma}_y$ the two degrees of freedom. All of these are extensional strain components, and this has the effect of extending the material along one or two axes, while it contracts along the remaining axes to preserve volume. However, a change of basis would transform this matrix into one with off-diagonal elements, which describe shear strain. We therefore see that for incompressible vorticity free flow, there will always be some axis along which there is shear strain and some axis along which there is extensional strain.

We now consider an additional deformational mode, which consists of a pure shear accompanied by a specific rotational mode, and is called simple shear. Simple shear has a strain rate tensor which in some basis takes the form

$$\dot{\gamma}_{ij} = \begin{bmatrix} 0 & \dot{\gamma} & 0 \\ 0 & 0 & 0 \\ 0 & 0 & 0 \end{bmatrix}, \tag{2.17}$$

where $\dot{\gamma}$ is the total applied strain rate. The trace of this is zero, so the material it describes is incompressible, but now both the vorticity and deviatoric tensor are non-zero, so we have a combination of pure shear and rotation. Assuming uniform strain, in which $\dot{\gamma}_{ij}$ is independent of position, we now have that the velocity field

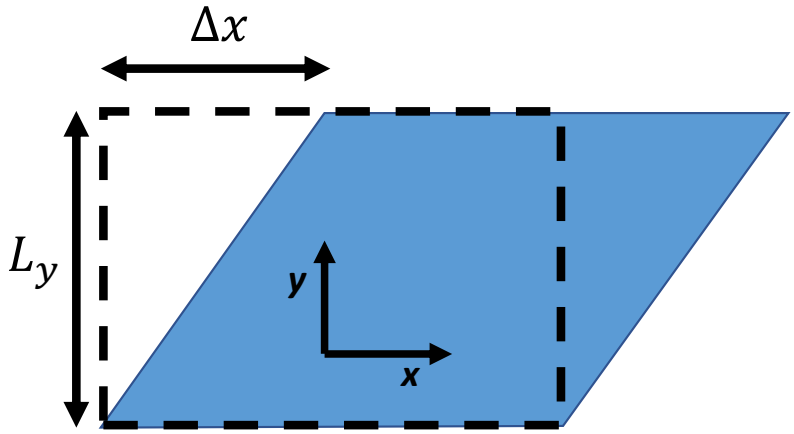

Figure 2.2: A sketch of a simple shear strain, γ_{xy}. The black dotted line shows the original sample, and the solid blue shows the shape after the strain.

in the material is described by

$$v_x(y) = y\dot{\gamma}, \tag{2.18}$$

with all other components zero. The displacement at any point in the sample is then given by

$$s_x(y,t) = \int_0^t y\dot{\gamma}dt' = y\gamma, \tag{2.19}$$

so the strain

$$\gamma = \frac{s_x}{y}. \tag{2.20}$$

If we assume the sample to have finite length L_y in the y-direction, the applied strain is then

$$\gamma = \frac{\Delta x}{L_y}, \tag{2.21}$$

with Δx the displacement in the x-direction. The shear strain then is the displacement in one direction divided by the sample size in a perpendicular direction, as shown in Fig. 2.2. This represents the fact that simple shear is a fundamentally different form of deformation to extensional strain. In both protocols, we can divide the system into a collection of 2D planes of infinitesimal width in which the velocity field is constant. In extensional strain, these planes are transported along the normal to each plane. In shear strain, however, the planes are transported in a direction which is parallel to the planes. While extensional strain consists of a material being

stretched (or squeezed), simple shear consists of layers of material sliding over each other [94].

We have now rigorously defined the concept of strain, and examined two common strain protocols: pure shear and simple shear. All of the work that is presented in this thesis uses simple shear protocols, which as we have seen applies no compression, but does have a rotational contribution.

2.1.2 Stress Tensor

To evaluate stress, we again consider a 3D sample of material. Externally applied forces all operate on the faces of the material, and we assume that the forces applied sum to zero. The material can then be divided into a collection of infinitesimal regions, and the forces within the material must be transmitted from one region to the next at the surfaces dividing them [95]. At every point in the surface, we can therefore define a 2D surface with any orientation, and consider the force which is exerted along that surface, and that force can in general be in any direction. To quantify this, we consider an infinitesimal surface of area ds with surface normal vector $\mathbf{n}$, and label the force transferred by the surface $d\mathbf{F}$. The stress on that surface can then be written as [96]

$$\mathbf{T}^{(\mathbf{n})} = \frac{d\mathbf{F}}{ds}. \tag{2.22}$$

This can be applied to a surface in any orientation, but linearity ensures that considering three orthogonal surfaces is sufficient to fully describe the forces at any point. We can therefore construct a stress tensor by considering the forces on surfaces which are perpendicular to the basis vectors [97], $\mathbf{x}$, $\mathbf{y}$, $\mathbf{z}$:

$$\boldsymbol{\Sigma} = \begin{bmatrix} \mathbf{T}^{(\mathbf{x})} & \mathbf{T}^{(\mathbf{y})} & \mathbf{T}^{(\mathbf{z})} \end{bmatrix} = \begin{bmatrix} \Sigma_{xx} & \Sigma_{xy} & \Sigma_{xz} \\ \Sigma_{yx} & \Sigma_{yy} & \Sigma_{yz} \\ \Sigma_{zx} & \Sigma_{zy} & \Sigma_{zz} \end{bmatrix}, \tag{2.23}$$

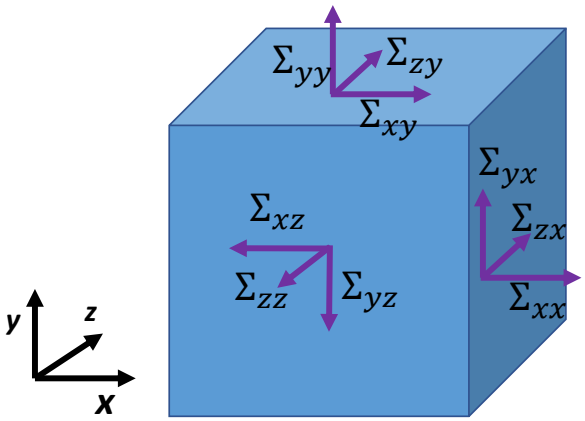

Figure 2.3: A sketch of a sample of material, showing the possible stresses. Each element of the stress tensor also acts in the opposite direction on the opposite face.

so that the stress on any surface is given by

$$\mathbf{T}^{(\mathbf{n})} = \boldsymbol{\Sigma} \cdot \mathbf{n}, \tag{2.24}$$

with $\mathbf{n}$ the unit vector perpendicular to that surface.

As with the strain tensor, there are two different forms of stress defined by the stress tensor. The diagonal components describe stress related to forces that act perpendicular to the surface through which they are transferred, and are referred to as the normal stress components. The normal components describe compressional and extensional forces on a material. The off diagonal components describe stress related to forces that act in the plane of the surface through which they are transferred, and are referred to as shear stress components. These components are associated with forces that push slabs of material past each other. Fig. 2.3 shows a sample of material with these stresses labelled.

We can define a hydrostatic pressure on a sample as

$$P = -\frac{1}{D}\sum_i \Sigma_{ii}, \tag{2.25}$$

with D the number of dimensions, and this acts to compress the material and change its volume. All of the materials we consider are incompressible, and the hydrostatic pressure adjusts to ensure that the incompressibility condition is always met. We

shall not consider the hydrostatic pressure for these materials. The normal stress components are then typically expressed as two normal stress differences. In simple shear with $v_x = \dot{\gamma} y$, the normal stress differences are [91]

$$N_1 = \Sigma_{xx} - \Sigma_{yy}, N_2 = \Sigma_{yy} - \Sigma_{zz}. \tag{2.26}$$

These normal stress differences then describe forces that act to extend a material along one axis while contracting on another, in a way that preserves volume. In this work, all of the protocols considered are simple shear with $\partial_y v_x = \dot{\gamma}$, and we will only consider the shear stress component, Σ_{xy}. This does not mean that the normal stress is zero, but for the systems we consider, we assume that the shear stress provides enough information to understand the key rheological phenomena of concern here.

2.2 Rheology

Rheology is the study of the deformation and flow properties of matter, and generally consists of studying the relationship between stress, strain and strain rate. We will start by considering how this is done experimentally, before discussing some common rheological phenomena.

2.2.1 Rheometer Geometry

Studying rheology requires applying strain and/or stress to a sample of material. Generally, this can either be strain controlled, in which a predetermined strain is applied to the material and the resulting stress measured, or stress controlled, in which a predetermined stress is applied and the resulting strain measured [98]. This is done using a rheometer, which is a machine designed for this purpose. There are a number of rheometer designs available, and we will only consider those that apply to shear protocols.

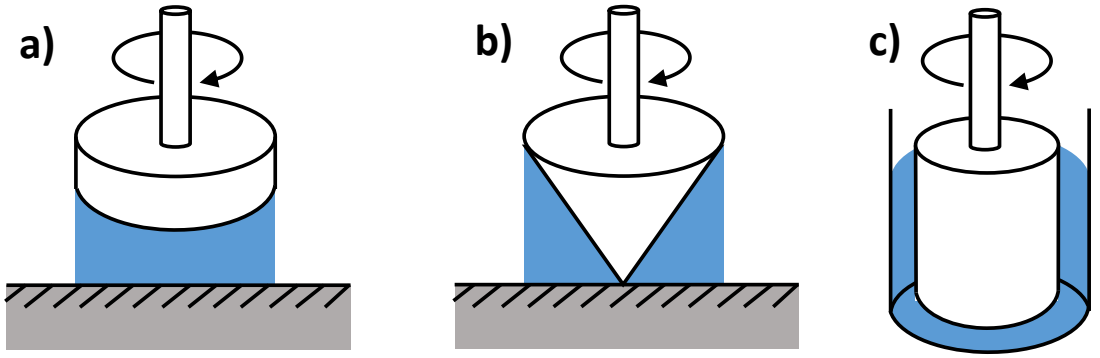

Figure 2.4: A sketch of some common rheometer geometries: **a)** Plate-plate, **b)** Cone-plate and **c)** Taylor-Couette. The angle of the cone is significantly more exaggerated than in most experimental setups.

Shear rheometers typically deform a material by placing a sample between two plates or cylinders, one of which is fixed, and the other of which rotates. The plates can have various designs, the simplest of which is plate-plate, in which there are two flat horizontal plates with the material in between, as shown in Fig. 2.4a. While this appears to be a simple design, it generates non-trivial dynamics, because the applied shear rate is a function of distance from the axle, and therefore non-uniform, and the non-uniformity is significant when compared to the applied shear rate. It is therefore more common to instead use a plate and cone geometry, in which there is one flat plate and another conical plate, the tip of which almost touches the bottom plate, as shown in Fig. 2.4b. The result of this is that both the speed of the rotation and the width of the sample vary linearly with distance from the axle, and so the applied shear rate is uniform across the sample [98]. However, a disadvantage of this geometry is that any material effects that have an associated length-scale may now occur non-uniformly across the sample due to its non-constant width. Also, the rotational motion can cause an effect called edge fracture [99], in which air gaps open in the edges of the material, which impacts the measured response.

An alternative is a Taylor-Couette geometry, in which the material is sandwiched in between two concentric cylinders, one of which rotates, as shown in Fig. 2.4c. There is then a curved slab of material which makes a full circle, and it is now simple to apply a nearly uniform shear. If the cylinders are very long, the flow is effectively

unidirectional in the azimuthal direction. A disadvantage of this geometry is that the flow is not completely flat due to the device curvature, and the result of this is that for inertialess flow (which we assume throughout this thesis), the stress field varies as [100]

$$\Sigma = \frac{B}{r^2}, \tag{2.27}$$

with r the distance from the axle, in contrast to the expression for flat inertialess flow, in which $\nabla\Sigma = \mathbf{0}$. This means that for a viscous fluid, the strain rate also varies across the sample [101] as

$$\dot{\gamma} = \frac{C}{r^2}. \tag{2.28}$$

The effect this has can be minimised by using cylinders with large radii and a small gap, but it still leaves some non-uniformity.

One additional experimental nuance is an effect called apparent wall-slip [102]. Where the material is in contact with the plates, it does not necessarily move at the same speed as the adjacent plate, and this can cause the rheometer to incorrectly measure the strain. There are a number of experimental techniques to minimise this, such as using cross hatched plates [103]. Throughout this work, we will neglect wall slip.

2.2.2 Flow Curves

A common way to characterise a material's rheology is via a flow curve. To obtain this, the material is sheared at a strain rate which is held constant after its first application at some time $t = 0$ until the material reaches a steady state in which the shear stress is independent of time. The steady state shear stress can then be plotted as a function of strain rate. This graph is referred to as the flow curve.

For a material to reach a steady state while under shear, it must have some level of viscous, plastic or fluid-like behaviour. Consider for example an elastic solid with stress proportional to strain, $\Sigma = K\gamma$. Under a constant applied shear rate, the stress will continue increasing indefinitely without reaching a steady state (in

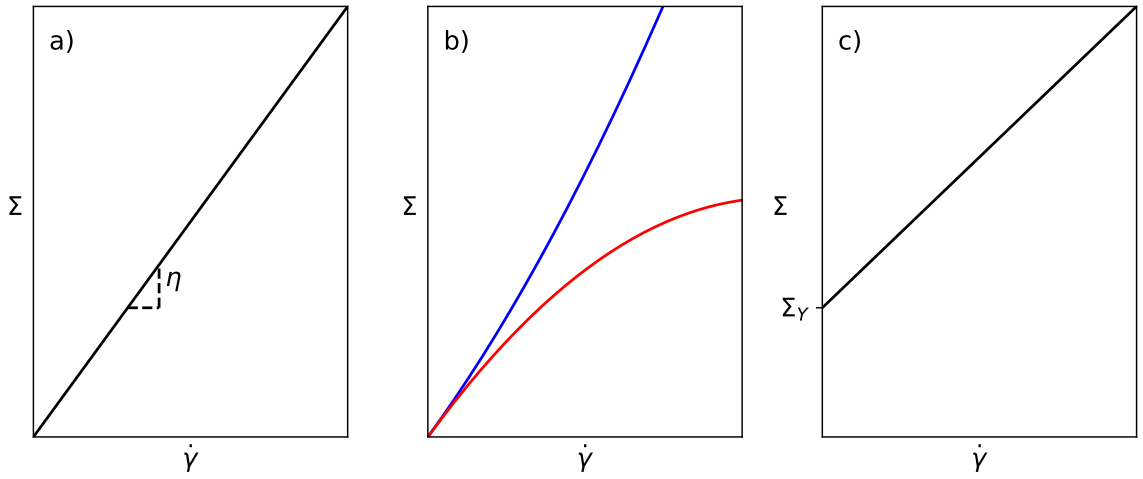

Figure 2.5: Flow curves of steady state stress against strain rate for **a)** a Newtonian fluid, **b)** a shear-thickening fluid (blue) and a shear-thinning fluid (red) and **c)** a yield stress fluid.

practice, a real material will break once the breaking strain is passed, and then display plastic behaviour). Alternatively, a Newtonian fluid with stress proportional to strain rate, $\Sigma = \eta\dot{\gamma}$, will have a flow curve that takes the form of a straight line passing through the origin, the gradient of which gives the viscosity of the fluid, as shown in Fig. 2.5a.

Two common non-linear responses that manifest in a flow curve are shear-thinning and shear-thickening. These are shown in Fig. 2.5b. At low strain rate, they both have $\Sigma \propto \dot{\gamma}$, as for a Newtonian fluid, but at higher strain rates the gradient increases for a shear-thickening fluid and decreases for a shear-thinning fluid. To characterise this, we can define a dynamic viscosity,

$$\eta = \frac{d\Sigma}{d\dot{\gamma}}, \tag{2.29}$$

and we see that this dynamic viscosity is a function of strain rate.

A third common class of materials are yield stress fluids. These have a flow curve in which stress is an increasing function of strain rate for $\dot{\gamma} > 0$, but the curve intercepts the stress axis at a non-zero value, which is referred to as the yield stress, Σ_Y, as shown in Fig. 2.5c. This means that a minimum stress must be applied to the material to generate a steady flow, and above this minimum stress, the material

behaves as a fluid. For a stress below the yield stress, these materials typically behave as elastic solids with $\Sigma \propto \gamma$. A Bingham fluid is a very common sub-class of yield stress fluid, in which for applied stresses above the yield stress, stress is linear in strain rate [42, 104]. Another common sub-class of yield stress fluid is a Herschel-Bulkley fluid [105], for which

$$\Sigma = \Sigma_Y + \kappa\dot{\gamma}^n. \tag{2.30}$$

This describes a yield stress fluid which, when a stress greater than the yield stress is applied, becomes shear-thinning for $n < 1$ and shear thickening for $n > 1$.

A flow curve is clearly a good way to distinguish between various classes of materials and characterise basic rheological behaviour. However, the flow curve only describes steady state behaviour, and many materials also exhibit a range of interesting time-dependent rheological phenomena before reaching steady state. To observe this behaviour, other rheological protocols are needed, which we now describe.

2.2.3 Shear Startup

A common protocol for characterising a material's rheology before it reaches steady state is shear startup, in which shear is applied at a constant rate $\dot{\gamma}$ for all time $t > 0$. For an elastic solid under shear startup, the stress would be linear with the strain $\gamma = \dot{\gamma}t$, until the breaking strain is reached, at which point the material no longer behaves elastically. On the other hand, a Newtonian fluid would have a stress response $\Sigma = \eta\dot{\gamma}$, which is determined by the shear rate, but remains constant at all times $t > 0$.

For a yield stress fluid, we typically see an initial elastic regime, in which stress is proportional to strain, $\Sigma \propto \gamma = \dot{\gamma}t$. Then, at larger strains, the stress approaches a steady state value, as prescribed by the steady state flow curve defined above. This steady state stress will be larger than the yield stress and depends on the strain rate.

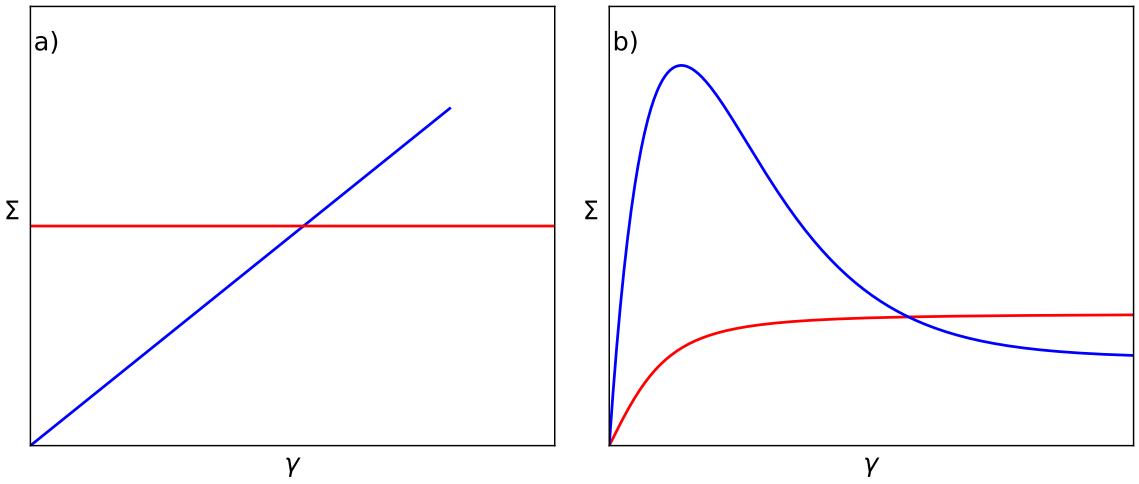

Figure 2.6: Startup curves of stress against strain at constant strain rate for some common classes of materials. **a)** An elastic solid (blue) and a viscous fluid (red). **b)** A yield stress fluid with no static yield stress (red) and with a static yield stress (blue), which leads to a stress overshoot.

Some yield stress fluids display a stress overshoot under shear startup, in which the stress increases to a maximum value and then decreases as it approaches its steady state. In this situation, the stress maximum is known as the static yield stress, and is the stress which is required to generate steady flow at a particular strain rate. The value of the steady state shear stress in the limit $\dot{\gamma} \to 0$ is instead known as the dynamic yield stress, and is the minimum stress required to maintain a state of steady flow at any strain rate. Fig. 2.6 shows startup curves for some common classes of materials.

2.2.4 Lissajous Figures

Another way to characterise the response of a material while in a state of flow is to apply an oscillatory shear protocol, such that

$$\begin{aligned} \gamma =& \gamma_0 \sin(\omega t) , \\ \dot{\gamma} =& \gamma_0 \omega \cos(\omega t) . \end{aligned} \tag{2.31}$$

The stress response can then be measured around each cycle, which reveals the dependence of stress on strain and strain rate separately. Typically, the response is plotted in two different graphical formats, one showing stress as a function of

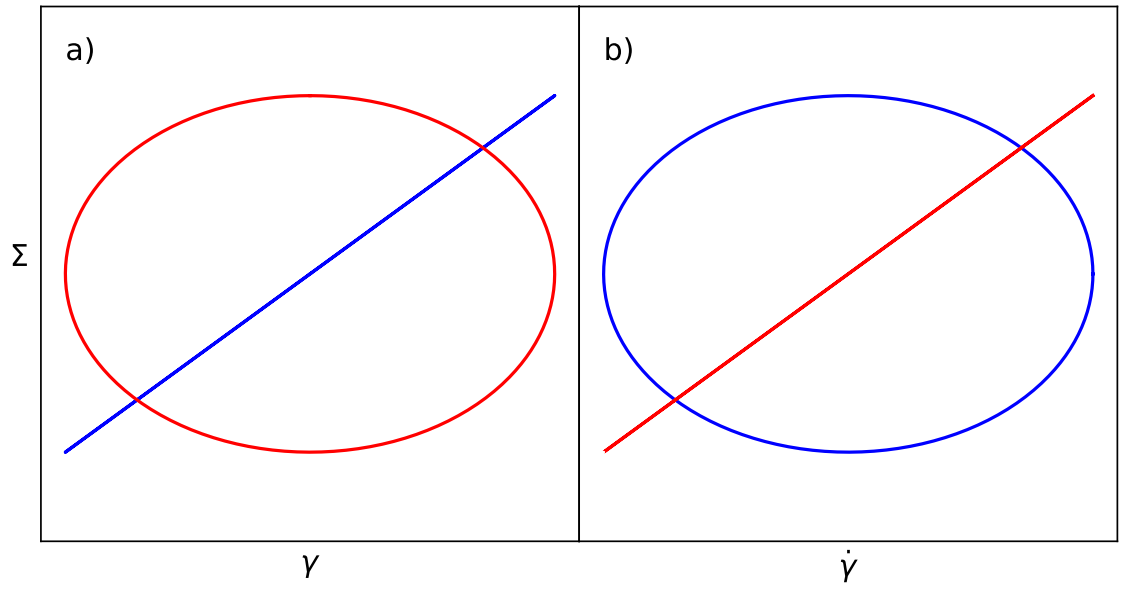

Figure 2.7: Lissajous figure showing stress as function of **a)** strain and **b)** strain rate under an oscillatory shear protocol $\gamma = \gamma_0 \sin(\omega t)$ for an elastic solid (blue) and a Newtonian fluid (red).

strain and the other showing a function of strain rate. These are known as Lissajous figures.

For an elastic solid with $\Sigma = k\gamma$, the plot showing stress as a function of strain will simply be a diagonal straight line. The dependence of stress on strain rate will look like

$$\Sigma^2 = k^2\gamma_0^2\left(1 - \frac{\dot{\gamma}^2}{\gamma_0^2\omega^2}\right), \tag{2.32}$$

which will appear as an ellipse.

For a Newtonian fluid with $\Sigma = \eta\dot{\gamma}$, the plot of stress as a function of strain rate will trivially be a straight diagonal line. The plot of stress as a function of strain will show an ellipse with

$$\Sigma^2 = \eta^2\gamma_0^2\omega^2\left(1 - \frac{\gamma^2}{\gamma_0^2}\right). \tag{2.33}$$

We therefore see that the two extreme cases of an elastic solid and a viscous fluid have very distinctive signals on this type of plot, which are shown in Fig. 2.7. In practice, most soft matter systems exhibit a mix of solid-like and fluid-like behaviours, and so they will produce a Lissajous figure that is neither a perfect

ellipse nor a straight line [63].

Time Dependence

Lissajous figures are typically plotted after many shear cycles, so that the material has had time to reach its oscillatory steady state, and there is little change from cycle to cycle. However, many soft matter systems change state during the application of an oscillatory shear protocol, and as a result the steady state Lissajous figure is insufficient to describe the full dynamics. Instead, a Lissajous figure for each shear cycle can be plotted to fully characterise the material response [65]. We will discuss this in detail in Ch. 4 and Ch. 5, where we examine slow fatigue and delayed yielding in two theoretical models under an applied oscillatory shear.

2.3 Shear Banding

So far, we have limited ourselves to assuming strain to be uniform throughout a sample. However, there are many effects that can cause both strain and strain rate to be heterogeneous. Important among these is the phenomenon known as shear banding, which has been extensively observed experimentally [106–117].

The most common reason for shear banding to arise is when a material has a non-monotonic constitutive curve [118–120], as sketched in Fig. 2.8a. The result of this is that there are some stresses at which the material has multiple states of steady flow at different strain rates. The material can therefore develop a state in which it is divided into multiple regions at different strain rates, as shown in Fig. 2.8b, but the stress is nonetheless uniform, as required by force balance. These shear bands are generally stable and can in principle persist indefinitely because each region is in one of the possible steady states.

To allow this effect in theoretical models, it is common to divide the total stress of the system into a elastoplastic contribution, σ, and a viscous contribution, $\eta\dot{\gamma}$,

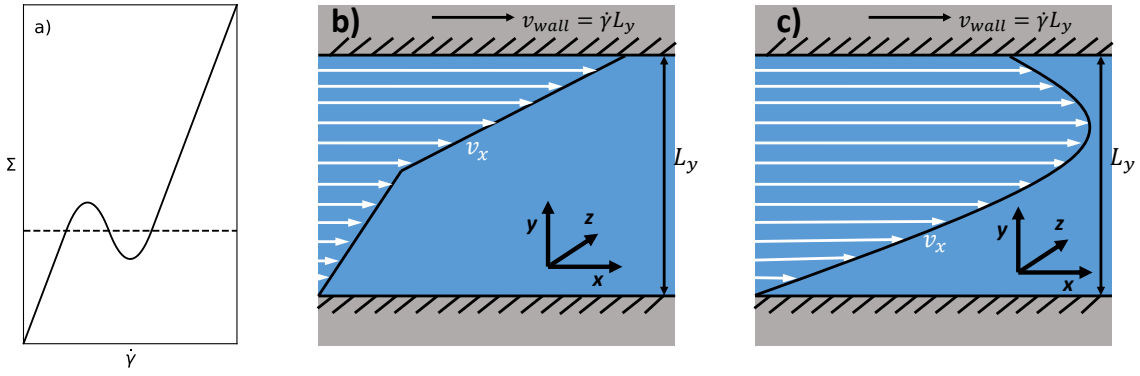

Figure 2.8: **a)** Non-monotonic constitutive flow curve, in which multiple strain rates are possible at the same stress. **b)** Velocity field for a material exhibiting shear banding, with different shear rates $\dot{\gamma} = \partial_y v_x$ in each of the two bands. **c)** Velocity field for a material exhibiting transient shear banding without distinct bands of different strain rates, in which the strain rate varies smoothly in space, and is locally negative in the upper section.

by assuming that the system comprises some elastoplastic material in a background solvent. The behaviour of σ is then related to the specific system being modelled. The total stress of the system is taken to be $\Sigma = \sigma + \eta\dot{\gamma}$, and the viscosity of the background solvent, η, is taken to be small. The total stress of the system then also obeys specific requirements. One common such requirements is to assume inertialess flow, which corresponds to setting the Reynoldss number to zero, and gives $\nabla_i \Sigma_{jk} = 0$ for unidirectional flow between two flat plates.

Once the stress has been decomposed in this way, it is common for the elastoplastic stress σ to vary in space. We assume that between neighbouring regions of different σ, there must be some interface with a non-zero width [121]. There will be some non-zero interfacial energy associated with these interfaces, which we expect to depend on the gradient of σ. We follow [121] and assume that the interfacial energy takes the form

$$E_I \propto \int dV \, (\nabla\sigma)^2 \,, \tag{2.34}$$

although other functional forms would render similar qualitative results. The interfaces will now generate a force which acts to minimise that energy, and so the

equation for σ needs to be modified by a term of the form

$$-\frac{\partial E_I}{\partial \sigma} = -\kappa \nabla^2 \sigma, \tag{2.35}$$

which has the effect of diffusing the elastoplastic stress across the sample. While we have noted here one possible form for a diffusive term, we will not use this precise form throughout. However, the key conclusion to be drawn from this analysis is that for a spatially varying σ, some kind of stress diffusive term should be included [121].

In principle, a material with a non-monotonic flow curve could form a state in which strain rate varies very rapidly in space and forms a large number of coexisting bands of alternating strain rate, but in practice this is not what is seen because of stress diffusion. In both experimental and theoretical systems, the effect of stress diffusion is to smooth out strain rate, so that typically only a small number of bands of distinct strain rate form [121].

More recently, transient shear banding has also been the subject of much study. Here, shear bands form during the early stages of a deformation but do not constitute a stable steady state, and so under continuous applied shear, the shear bands will eventually decay and the material return to a state of homogeneous flow [35, 44, 114, 122–124]. Transient shear banding is generally the result of an instability in the system, which causes the growth of heterogeneity when certain requirements are satisfied. For example, in some systems, when the stress is relaxing as a function of strain, $\partial_\gamma \sigma < 0$, the system is unstable to perturbation growth [44]. In other systems, instability can be related to the curvature of the stress-strain curve [125]. By the time the system reaches its steady state, these requirements are no longer satisfied, and so the system evolves towards a homogeneous state once more. Because they arise out of instability, transient shear bands only form when there is some form of perturbation in the system. In experimental systems, this perturbation is present naturally due to thermal or mechanical noise or device curvature, but in computational systems it sometimes needs to be added by hand.

Transient shear bands do not always have sharply defined bands of different

shear rates, as is the case for steady state shear bands. Instead, the strain rate can vary smoothly across the whole sample, and as a result the velocity profile can be non-linear, and even have locally negative strain rates [126]. An example velocity profile for a transient shear band without clearly delineated regions is shown in Fig. 2.8c. Although transient shear bands will by definition decay after a long enough time, many of them can be very long lived [35], which means that on experimentally or computationally accessible timescales, the apparent steady state remains banded.

2.4 Methodology

In this work, we study theoretical constitutive models of soft matter systems and solve them computationally. Some of the models used involve simulating a finite number of discrete material elements, which evolve according to some specified dynamics. For these models (Ch. 4 and Ch. 5), the dynamics presented in the relevant sections provide a full description of the way in which the model is simulated.

The remaining models (Ch 3 and Ch. 6) take the form of continuum first order implicit differential equations of some number of variables. For these models, we numerically solve these dynamical equations using the fourth order Runge-Kutta method (RK4) [127]. For a system of n variables, $x_1, x_2, ..., x_n$, we combine these variables into a single time dependent vector, $\mathbf{x}(t)$. We can write the time derivative of $\mathbf{x}$ at any time,

$$\frac{\partial \mathbf{x}}{\partial t} = \mathbf{f}(\mathbf{x}), \tag{2.36}$$

where $\mathbf{f}$ is constructed from the dynamical equations. If we know the state of the system at time t, we can then advance the state by a small time increment, Δt,

through the following calculations:

$$\begin{aligned}
\mathbf{k_1} =& \mathbf{f}\left(\mathbf{x}\left(t\right)\right), \\
\mathbf{k_2} =& \mathbf{f}\left(\mathbf{x}\left(t\right) + \Delta t\frac{\mathbf{k_1}}{2}\right), \\
\mathbf{k_3} =& \mathbf{f}\left(\mathbf{x}\left(t\right) + \Delta t\frac{\mathbf{k_2}}{2}\right), \\
\mathbf{k_4} =& \mathbf{f}\left(\mathbf{x}\left(t\right) + \Delta t\mathbf{k_3}\right), \\
\mathbf{x}\left(t+\Delta t\right) =& \mathbf{x} + \frac{1}{6}\left(\mathbf{k_1} + 2\mathbf{k_2} + 2\mathbf{k_3} + \mathbf{k_4}\right).
\end{aligned} \tag{2.37}$$

Provided the time step is sufficiently small, we can repeat this process a large number of times, and the result will be a very good approximation to the exact solution to the dynamical equations.

In Ch 3, we simulate a large number of lattice points, each of which is in a slightly different state $\mathbf{x}$, so that we can model heterogeneity. While RK4 is sufficient to advance a single lattice point, we have an additional term in the dynamical equations which couples lattice points together, which takes the form of a diffusive term, as introduced in Sec. 2.3. To evolve the system, we therefore have to follow two processes at each step: first, we advance each lattice point using RK4, then we apply the spatial coupling term to the whole system using a Crank-Nicolson algorithm (CN) [128, 129].

To apply the CN algorithm, we note that our system is already discretised in space and time, and we write the state vector as

$$\mathbf{x}_i^n, \tag{2.38}$$

where the superscript denotes the time step and the subscript denotes the position. The diffusive term which we need to advance takes the form

$$\frac{\partial \mathbf{x}}{\partial t} = \cdots + \alpha\frac{\partial^2 \mathbf{x}}{\partial y^2}, \tag{2.39}$$

and we advance this using a second-order implicit Runge-Kutta method, which when

discretised takes the form

$$\frac{\mathbf{x}_i^{n+1} - \mathbf{x}_i^n}{\Delta t} = \frac{\alpha}{2\Delta y^2}\left[\left(\mathbf{x}_{i+1}^{n+1} - 2\mathbf{x}_i^{n+1} + \mathbf{x}_{i-1}^{n+1}\right) + \left(\mathbf{x}_{i+1}^{n} - 2\mathbf{x}_i^{n} + \mathbf{x}_{i-1}^{n}\right)\right]. \tag{2.40}$$

This can be rearranged to have all the terms in $\mathbf{x}^{n+1}$ on the left hand side, and then expressed as a matrix equation with

$$\mathbf{A}\begin{bmatrix} \mathbf{x}_0^{n+1} \\ \mathbf{x}_1^{n+1} \\ \vdots \\ \mathbf{x}_m^{n+1} \end{bmatrix} = \mathbf{B}\begin{bmatrix} \mathbf{x}_0^{n} \\ \mathbf{x}_1^{n} \\ \vdots \\ \mathbf{x}_m^{n} \end{bmatrix}, \tag{2.41}$$

with $\mathbf{A}$ and $\mathbf{B}$ two matrices, and we can calculate all of their elements, provided we are careful with the boundary conditions. We use symmetric boundary conditions, and assume all fields are smooth, with zero gradient at each edge of the sample. This is accounted for when calculating the matrices by considering an additional element past each edge of the sample, $\mathbf{x}_{-1}^n = \mathbf{x}_1^n$ and $\mathbf{x}_{m+1}^n = \mathbf{x}_{m-1}^n$. Eq. 2.40 can then be applied to calculate the matrix elements of $\mathbf{A}$ and $\mathbf{B}$ for all $0 \leq i \leq m$, with slight modification to the first and last row of the matrices to account for these boundary conditions. Inspection of Eq. 2.40 reveals that $\mathbf{A}$ and $\mathbf{B}$ are both tridiagonal, and because we can evaluate everything on the right hand side of the matrix equation, we can calculate the next state of the system if we can invert $\mathbf{A}$. We carry out this inversion using the Thomas algorithm [130], which takes only $\mathcal{O}(m)$ time, with m the number of grid points. Once the matrix has been inverted, it is trivial to construct the state of the system at the next time step.

2.5 Conclusion

In this chapter, we have introduced the concepts of stress and strain, and defined the normal and shear components of these in terms of the deformations applied to a sample of material. We considered some common strain protocols, including simple shear, which is what we use throughout this thesis. We also considered the effect on

a sample of material of various components of the stress tensor.

We then considered how to experimentally measure the response of a material to a deformation by discussing rheometry and rheometer geometry. Next, we introduced some common measurement protocols, in the form of the flow curve, shear startup curves and Lissajous figures. We considered the response of various common materials to these protocols, including elastic solids, Newtonian fluids, shear-thinning and shear-thickening fluids and yield stress fluids.

Next, we introduced the concept of shear banding, in which the strain rate becomes heterogenous across a sample. We considered both transient and steady state shear banding, and some of the key differences between them. We also saw that allowing strain heterogeneity requires the imposition of a stress diffusive term, and considered the effect that this has on shear banded systems.

Finally, we have introduced some of the computational methods which will be used in this work, in the form of the RK4 method and the Crank-Nicolson algorithm.

Chapter 3

Ductile and Brittle Yielding in Soft Glassy Materials

3.1 Introduction

A wide range of amorphous materials display elasto-plastic behaviour, in that they have a solid-like regime and a plastic-like regime when deformed. The solid-like regime is characterised by a near-elastic stress-strain response, where stress is typically very close to proportional to strain. The plastic regime is characterised by plastic deformation, where very large deformations can occur at a near-constant stress. Notably, the transition between these behaviours can be driven entirely by the load or deformation applied to the system. This transition is called yielding and is generally caused by internal state changes.

Many viscoelastic materials also undergo a yielding process, where there is a macroscopic change to the global mechanical response from an elastic regime at small deformation to a plastic regime at large deformation [38, 43]. Previous experimental work has explored shear-startup in carbopol microgels [114, 131] and silica based colloidal gels [12] and identified that they exhibit an elastic branch at small strain, followed by a stress overshoot, and then relaxation to plastic flow, along with long

lived transient shear banding during the regime of stress relaxation. Further experimental work with colloidal gels [13] found that fluidity transitions start occurring in small, spatially localised pockets, which then grow and spread out over the sample with a characteristic time that exponentially decreases with the applied stress, until the whole sample has fluidised.

Molecular dynamical simulations of amorphous systems [132] under shear startup found transitions towards heterogeneous flow, which only at low strain rates develop into shear bands, which are transient but long lived. A combination of theoretical and experimental work [133] found that in stress controlled protocols, as the applied stress of the systems explored increased past the yield stress, regions with faster particle movement grow heterogeneously, allowing particles to diffuse as steady flow sets in. Study of a fluidity model and the soft glassy rheology model [35] under shear startup found that both these models show transient shear banding for a wide range of parameters, and that this shear banding is often associated with fast stress relaxation. Fluid-universal criteria for linear instability to shear banding growth have also been developed [125] for a number of rheological protocols, including shear startup, in which it was found that banding begins to grow just before a stress overshoot as a function of strain.

In general, yielding can occur smoothly or can be abrupt and catastrophic. It has been argued in Ref. [43] that amorphous solids yield in two distinct ways: discontinuous "brittle" yielding, which is catastrophic and precipitous; or continuous, "ductile" yielding, which is smooth. The authors of Ref. [43] argue that these two regimes are separated by a random critical point, and characterised by qualitatively different underlying stress-strain curves. In Ref. [43], brittle yielding occurs in systems in which the stress-strain curve has a stress overhang, the result of which is that for a protocol in which strain increases monotonically, the stress will drop discontinuously. In contrast, ductile yielding in Ref. [43] occurs in systems with a stress overshoot and is accompanied by continuous stress.

In this work, we will use a fluidity model to further explore yielding transitions

under shear startup. We will argue that ductile and brittle yielding are different manifestations of the same phenomenon, and that the materials we study in this work only undergo continuous yielding. We will argue that 'brittle' and 'ductile' are the two limiting cases of a continuum of yielding speeds, without requiring an overhang in the stress-strain curve or a random critical point.

In Sec. 3.2 we consider a fluidity model for age-dependent soft glassy fluids, as in [35, 134], and we aim to explore mathematically and computationally how the model system yields in various situations. In Sec. 3.4.1 we consider the system when homogeneous shear is artificially enforced. In Sec. 3.4.2 we consider the situations in which the system is linearly unstable to perturbation growth, and therefore likely to exhibit shear banding. In Sec. 3.4.3 we carry out detailed non-linear simulations of the system, and we find a continuum of continuous yielding rates, ranging from slow and smooth to fast and precipitous, which are two facets of the same phenomenon. We also find that fast yielding with an infinite negative gradient in the stress-strain curve, which would be measured experimentally as discontinuous yielding, is the limiting situation at zero strain rate, infinite sample age and zero diffusion.

3.2 Model

We consider a model of a soft glassy fluid comprised of an elastoplastic fluid with a scalar, shear-dependent fluidity, following [35]. The total shear stress Σ is decomposed into a viscoelastic part σ and a purely viscous part, so that

$$\Sigma = \sigma + \eta\dot{\gamma}, \tag{3.1}$$

where the viscosity of the purely viscous part, η, is assumed to be small. We will assume a Reynolds number of 0 (neglecting inertia), which requires Σ to be spatially invariant, allowing us to use it to describe global behaviour. We use a Maxwell-type

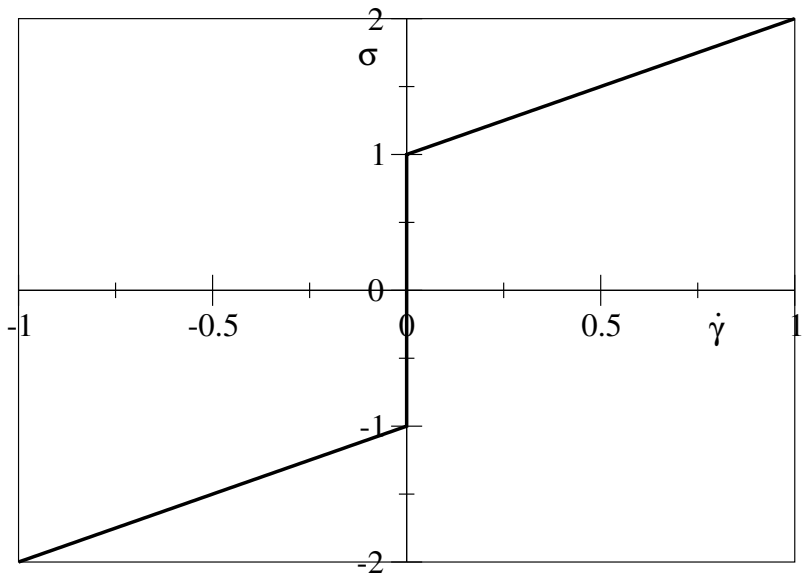

Figure 3.1: Steady state flow curve of stress against strain for the model with $G = \tau_0 = 1$. The yield stress must be overcome ($|\sigma| > 1$) for the system to flow in steady state.

constitutive equation, dependent on fluidity, for the viscoelastic stress

$$\partial_t \sigma = G\dot{\gamma} - \frac{\sigma}{\tau}, \tag{3.2}$$

where G is an elastic modulus and τ is the structural relaxation time, or inverse fluidity. τ then has its own dynamics:

$$\partial_t \tau = 1 - \frac{\tau}{\tilde{\tau}(\dot{\gamma})} + \frac{l_0^2}{\tau_0}\partial_y^2 \tau. \tag{3.3}$$

We define $\tilde{\tau}(\dot{\gamma})$ so that $\tilde{\tau}(0) \to \infty$, and without flow this then represents simple ageing, with the total change in τ over a given time interval, $\Delta\tau$, equal to the total time, Δt. When the system is in a state of steady flow, $\tilde{\tau}(\dot{\gamma})$ is the new steady state value of τ, and τ evolves towards it. l_0 is a mesoscopic length which describes the tendency for one region to equalise with its neighbours, and the right hand term is a diffusive one which damps heterogeneity [121].

We choose our steady state relaxation time to be

$$\tilde{\tau} = \tau_0 + \frac{1}{|\dot{\gamma}|}, \tag{3.4}$$

so that we have a steady state stress under flow of $\sigma = G\dot{\gamma}\tilde{\tau} = G(\tau_0\dot{\gamma} \pm 1)$, with the

$\pm$ following the sign of the strain rate. For a stress $-G < \sigma < G$, the steady state strain rate is $\dot{\gamma} = 0$, and so this is a Bingham fluid [42], with a yield stress $\sigma_Y = G$, as shown in Fig. 3.1. For a stress below this yield stress, the material behaves like an elastic solid, while above it the stress increases monotonically with strain rate in a fluid-like manner. We will work in units of stress and time for which $G = \tau_0 = 1$. For the rest of this discussion, we will use $\eta = 0.05$ unless stated otherwise.

τ_0 represents the timescale on which microscopic movements take place, and as such is generally small compared to laboratory timescales. As a result, it would be difficult to shear an experimental system at a strain rate which is fast compared to τ_0. We therefore impose $\bar{\dot{\gamma}}\tau_0 \ll 1$ throughout.

3.3 Shear Protocol

We consider a sample of infinite extent in the x (flow) and z (vorticity) directions, we assume translational invariance in these directions and neglect edge effects, and consider shear flow between two flat parallel plates at $y = 0, L_y$. We will work in length units in which $L_y = 1$. Within these assumptions, σ, τ and $\dot{\gamma}$ can only depend on y.

We study a shear start-up protocol defined as follows. First, the sample is prepared by a deep quench at $t = -t_w$, resulting in a fully rejuvenated state with $\tau\left(y, t = -t_w\right) = 1, \sigma\left(y, t = -t_w\right) = 0$. We then allow the sample to age at rest, with $\dot{\tau} = 1$, until time $t = 0$, at which point we set the upper plate moving along x with constant speed $\bar{\dot{\gamma}} L_y = \bar{\dot{\gamma}}$, which defines the imposed average shear rate. Assuming no-slip conditions, the local shear rate, $\dot{\gamma}\left(y, t\right)$, must satisfy $\bar{\dot{\gamma}} = \int_0^1 \dot{\gamma}(y,t)dy$.

3.4 Results

3.4.1 Homogeneous Dynamics

We will start by considering this system when it is artificially constrained to flow homogeneously. We do so by setting the shear rate throughout the sample to be equal to the imposed shear rate, and therefore do not need to model multiple points in space. The behaviour of the system is now fully described by the vector $(\sigma, \tau)^T$ evolving in time according to Eq. 3.2, 3.3 without the diffusive term.

The dashed lines in Fig. 3.2 show how the shear stress, Σ, evolves for several different values of ageing time, t_w, and fixed $\bar{\dot{\gamma}}$, and shows two interesting features. For low ageing time ($t_w = 10^2$), the global stress response increases monotonically towards the steady state value, then plateaus when it reaches it. For higher values of t_w, however, the global stress shows a linear elastic branch, which overshoots the steady state value, reaches a maximum and then decays to the steady state viscous behaviour from above. To understand this, let us consider σ, remembering that initially $\tau = t_w$, and that it then decays towards its steady state value of $\tau = \tilde{\tau}$. When τ is large, $\frac{\sigma}{\tau}$ is small, and so $\partial_t \sigma \approx G\dot{\gamma}$, giving linear elastic behaviour as observed until τ becomes small enough for the stress to drop off. From this, it is easy to see qualitatively why a small initial value of τ will result in no overshoot.

To examine this more carefully, first we solve for $\tau(t)$, and find that

$$\tau(t) = t_w e^{-\frac{t}{\tilde{\tau}}} + \tilde{\tau}\left(1 - e^{-\frac{t}{\tilde{\tau}}}\right). \tag{3.5}$$

To solve for σ, we will need to multiply an integrating factor, which is found by integrating τ,

$$P = e^{\int \frac{1}{\tau} dt} = \left(e^{t/\tilde{\tau}} - 1\right)\tilde{\tau} + t_w, \tag{3.6}$$

and gives us that

$$\partial_t (P\sigma) = P\dot{\gamma}, \tag{3.7}$$

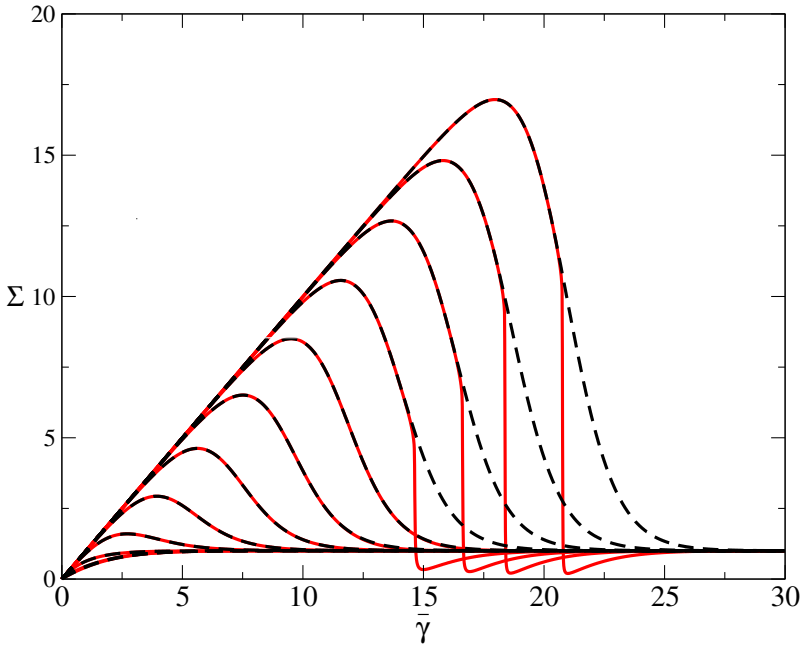

Figure 3.2: Numerical homogeneous (dashed), and heterogeneous (solid) start-up curves for the system at $\bar{\dot{\gamma}} = 10^{-3}$ for $t_w = 10^1, 10^2, ..., 10^{12}$ left to right.

which is solved by

$$\sigma(t) = \frac{\dot{\gamma}\left[\tilde{\tau}^2\left(e^{t/\tilde{\tau}} - 1\right) + (t_w - \tilde{\tau})\, t\right]}{\tilde{\tau}\left(e^{t/\tilde{\tau}} - 1\right) + t_w}. \tag{3.8}$$

To find out more about the stress peak, we will need to consider the derivative of σ,

$$\partial_t \sigma = \dot{\gamma}\frac{e^{t/\tilde{\tau}}\left[\tilde{\tau}\left(2t_w - \tilde{\tau}\right) + t\left(\tilde{\tau} - t_w\right)\right] + \left(\tilde{\tau} - t_w\right)^2}{\left[t_w + \tilde{\tau}\left(e^{t/\tilde{\tau}} - 1\right)\right]^2}. \tag{3.9}$$

We are now interested in whether this expression is ever negative, as that is necessary and sufficient for an overshoot, and if so when it crosses the time axis, which will give us the location of the overshoot. The denominator (and $\dot{\gamma}$) is always positive, so we need to consider the strain at which the stress is instantaneously constant:

$$\dot{\gamma}^2\left\{e^{t/\tilde{\tau}}\left[\left(2t_w - \tilde{\tau}\right)\tilde{\tau} + t\left(\tilde{\tau} - t_w\right)\right] + \left(\tilde{\tau} - t_w\right)^2\right\} = 0. \tag{3.10}$$

Substituting in the expression for $\tilde{\tau}$ and noting that $\tau_0\dot{\gamma} \ll 1$ for all the situations in which we use this model, we set $\tau_0\dot{\gamma} = 0$ and find that

$$\exp(\gamma)\left[2t_w\dot{\gamma} - 1 - \gamma\left(\dot{\gamma}t_w - 1\right)\right] + \left[t_w\dot{\gamma} - 1\right]^2 = 0. \tag{3.11}$$

First, consider the case when $t_w\dot{\gamma} - 1 = 0$, when the expression reduces to

$$\exp(\gamma) t_w \dot{\gamma}, \tag{3.12}$$

which is necessarily positive, and so there is no overshoot in this situation.

Next, consider the case when $t_w\dot{\gamma} - 1 > 0$. There is a growing exponential which is multiplied by the sum of two quantities, one positive and one negative. The negative term, $-\gamma(\dot{\gamma}t_w - 1)$, grows with γ, while the positive term, $2t_w\dot{\gamma} - 1$, is constant, and so the expression must be negative for γ greater than some threshold, γ_0. The remaining term in the expression, $[t_w\dot{\gamma} - 1]^2$, is necessarily positive, although also constant and therefore quickly becomes small when compared to the exponential. We can therefore conclude that in this case, the rate of change of stress will become negative.

Next we consider the case where $t_w\dot{\gamma} - 1 < 0$, and note that $t_w\dot{\gamma} - 1 > -1$. The squared term on the right is still positive, and the exponential term now multiplies a growing positive term and a term which is either positive or small and negative. The expression (for rate of change of stress) will therefore only grow after $t = 0$. From the assumption that the total stress is always in the same direction as the shear, we know that $\partial_t\sigma(t = 0) \geq 0$, and therefore $\partial_t\sigma$ is always positive. In this case, then, we conclude that the stress increases monotonically.

From this, we deduce that the condition for an overshoot is

$$t_w\dot{\gamma} > 1. \tag{3.13}$$

We will now try to determine when the stress maximum occurs, which will be when $\partial_t\sigma = 0$, and to do this we first use the above results to assume that $t_w\dot{\gamma} \gg 1$. Eq. 3.11 now reduces to

$$e^{\gamma_0} t_w\dot{\gamma}(2 - \gamma_0) + (t_w\dot{\gamma})^2 = 0, \tag{3.14}$$

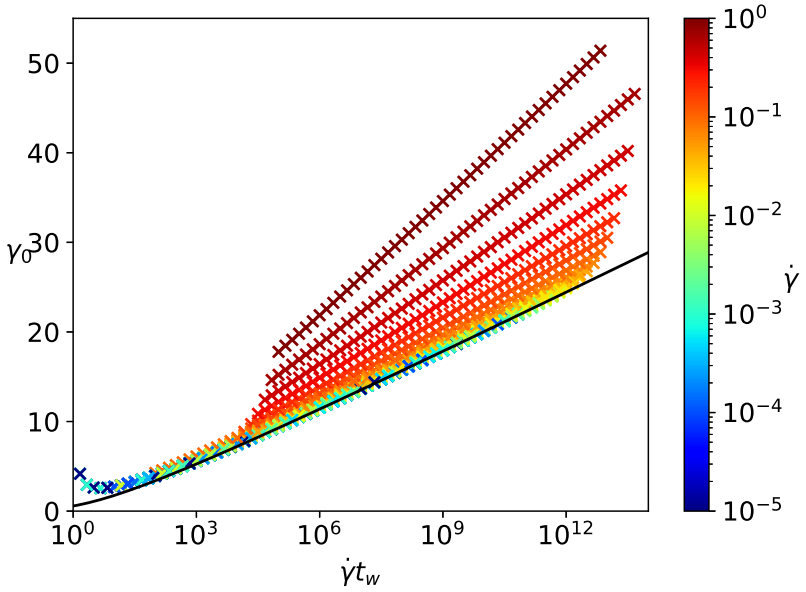

Figure 3.3: Strain when stress is maximum, γ_0, plotted against $\dot{\gamma}t_w$ for homogeneous curves (crosses), coloured according to $\dot{\gamma}$. The solid black line shows the strain at which $\gamma_0 e^{\gamma_0} = t_w\dot{\gamma}$. At low $\dot{\gamma}$ and high $\dot{\gamma}t_w$, we expect the crosses to fall on the black line.

we will assume that the overshoot occurs at a strain $\gamma_0 \gg 1$, and find that

$$\gamma_0 e^{\gamma_0} = t_w\dot{\gamma}, \tag{3.15}$$

and so the strain at which the stress maximum occurs is dependent on $\dot{\gamma}t_w$. We do not calculate here the height of the stress overshoot, however, note that for a significant majority of the time before the overshoot, stress is directly proportional to strain. The maximum stress will therefore be very close to the strain at which it occurs multiplied by G.

Fig. 3.3 shows strain at which the stress overshoot occurs from homogeneous simulations, and also the line of Eq. 3.15, and it can be seen that they are similar. The crosses are colour coded according to strain rate, which reveals that the discrepancies from Eq. 3.15 occur at large $\dot{\gamma}$ and small $\dot{\gamma}t_w$. This is as expected, as we assumed $\dot{\gamma}$ to be small and $\dot{\gamma}t_w$ to be large, and within this regime, the overshoot height matches the predicted curve very well.

3.4.2 Linear Stability Analysis

We are also interested in how the system behaves when heterogeneity in σ, τ and $\dot{\gamma}$ in the flow gradient direction is allowed. From now on, we will stop including τ_0 in equations, as we chose a unit system in which its value is 1. To see when heterogeneous startup curves will differ from the homogeneous one, we need to carry out a linear stability analysis. This will tell us under what conditions any small spatial perturbations will grow into measurable heterogeneity and noticeable shear bands will develop. Shear bands will, in general, modify the behaviour of the system, so this analysis also tells under what situations we expect heterogeneous startup curves to be different to homogeneous curves. To do this, we define the background state, $\bar{\sigma}$, $\bar{\tau}$, $\bar{\dot{\gamma}}$, which follows the homogeneous dynamics, and the first order perturbations, $\delta\sigma$, $\delta\tau$, $\delta\dot{\gamma}$, which characterise the degree to which flow becomes heterogeneous. Both the base state and the perturbation depend on time, and are expressed as follows:

$$\sigma = \bar{\sigma} + \sigma_1 \cos(\pi y/L) = \bar{\sigma} + \delta\sigma, \tag{3.16}$$

$$\tau = \bar{\tau} + \tau_1 \cos(\pi y/L) = \bar{\tau} + \delta\tau, \tag{3.17}$$

$$\dot{\gamma} = \bar{\dot{\gamma}} + \dot{\gamma}_1 \cos(\pi y/L) = \bar{\dot{\gamma}} + \delta\dot{\gamma}, \tag{3.18}$$

$$\Sigma = \Sigma_0. \tag{3.19}$$

For the last equation we have used that force balance requires that there is no heterogeneity in Σ. We only consider the lowest Fourier mode because it is the most unstable and is commonly generated experimentally by device curvature, which is discussed further below. Substituting Eq.3.1 into Eq. 3.19, we find that

$$0 = \delta\sigma + \eta\delta\dot{\gamma}, \tag{3.20}$$

$$\delta\dot{\gamma} = -\frac{\delta\sigma}{\eta}. \tag{3.21}$$

The perturbation can now be considered separately to the base state, $\bar{\sigma}$, $\bar{\tau}$ and $\bar{\dot{\gamma}}$, which is defined to evolve according to the homogeneous dynamics. To do this, we define

$$\partial_t\sigma = f\left(\sigma, \tau, \dot{\gamma}\right), \partial_t\tau = g\left(\sigma, \tau, \dot{\gamma}\right), \tag{3.22}$$

then Taylor expand around the base state to first order and find that

$$\partial_t\delta\sigma = \delta\sigma\frac{\partial f}{\partial\sigma} + \delta\tau\frac{\partial f}{\partial\tau} + \delta\dot{\gamma}\frac{\partial f}{\partial\dot{\gamma}}, \tag{3.23}$$

and similarly for $\delta\tau$. Using Eq. 3.21 to replace $\delta\dot{\gamma}$ with $\delta\sigma$ gives us

$$\partial_t\delta\sigma = \delta\sigma\frac{\partial f}{\partial\sigma} + \delta\tau\frac{\partial f}{\partial\tau} - \frac{\delta\sigma}{\eta}\frac{\partial f}{\partial\dot{\gamma}}. \tag{3.24}$$

Using only the linear part of the Taylor expansion, with higher order terms neglected, as expressed here, requires that the higher order terms are much smaller. Examination of the derivatives reveals that approximation is valid for all of the terms except one, which is the expansion for $\partial_t\delta\tau$, which contains terms of the following form:

$$\partial_t\delta\tau = ... + \frac{1}{n!}\left(-\frac{\delta\sigma}{\eta}\right)^n\frac{\partial^n\left(g\right)}{\partial\dot{\gamma}^n}. \tag{3.25}$$

Differentiating g gives us that

$$\frac{\partial^n\, g}{\partial\dot{\gamma}^n} = \frac{\left(-1\right)^n\bar{\tau}n!}{\left(1+\bar{\dot{\gamma}}\right)^{n+1}}, \tag{3.26}$$

which in combination with Eq. 3.25 gives us

$$\partial_t\delta\tau = ... + \frac{\bar{\tau}}{1+\bar{\dot{\gamma}}}\left(-\frac{\delta\sigma}{\eta\left(1+\bar{\dot{\gamma}}\right)}\right)^n. \tag{3.27}$$

The higher orders of this term will only vanish if the term in brackets is less than 1, and so we will need to avoid the regime in which it is not. $\bar{\dot{\gamma}}$ is typically small compared to 1, and so we find an additional condition for our linear stability analysis

to hold:

$$\frac{\delta\sigma}{\eta} \ll 1, \tag{3.28}$$

and if we are outside that regime we will have non-linear behaviour which does not follow the rest of this analysis. For most of the results presented, condition 3.28 holds.

Assuming linearity, we can write the perturbation dynamics as a matrix equation:

$$\partial_t \begin{bmatrix} \delta\sigma \\ \delta\tau \end{bmatrix} = M \begin{bmatrix} \delta\sigma \\ \delta\tau \end{bmatrix} = \begin{bmatrix} -\frac{1}{\bar{\tau}} - \frac{1}{\eta} & \frac{\bar{\sigma}}{\bar{\tau}^2} \\ \frac{\bar{\tau}}{\eta\left(1+\bar{\dot{\gamma}}\right)^2} & -\frac{1}{1+\frac{1}{\bar{\dot{\gamma}}}} - l_0^2\pi^2 \end{bmatrix} \begin{bmatrix} \delta\sigma \\ \delta\tau \end{bmatrix}. \tag{3.29}$$

For now, we will neglect the diffusive term, $l_0^2\pi^2$, as l_0 describes a microscopic length scale, which will be much shorter than the wavelength of the perturbations, and therefore is generally small compared to the other terms. Eq. 3.29 is then in general diagonalisable, and will have two separate modes. We are interested in whether either of these is a growing mode, as a single growing mode is sufficient for the magnitude of the heterogeneity to grow. The growth rate of each mode is determined by the eigenvalues, and so we need to find a condition for a positive eigenvalue. We note that the trace of the growth matrix, $-\frac{1}{\bar{\tau}} - \frac{1}{\eta} - \frac{1}{1+\frac{1}{\bar{\dot{\gamma}}}}$, is necessarily negative as $\bar{\tau}$, η and $\bar{\dot{\gamma}}$ are all positive, and so standard matrix results tell us that $|M| > 0$ gives both eigenvalues negative, while $|M| < 0$ gives one positive and one negative. We therefore find that the condition for linear instability is

$$0 > |M| = \left(\frac{1}{\bar{\tau}} + \frac{1}{\eta}\right)\frac{1}{1+\frac{1}{\bar{\dot{\gamma}}}} - \frac{\bar{\sigma}}{\bar{\tau}\eta\left(1+\bar{\dot{\gamma}}\right)^2}. \tag{3.30}$$

Assuming that $\eta \ll \bar{\tau}$ and $\bar{\dot{\gamma}} \ll 1$, this reduces to

$$\frac{\bar{\sigma}}{\bar{\tau}\eta} > \frac{\bar{\dot{\gamma}}}{\eta}, \tag{3.31}$$

$$\bar{\sigma} > \bar{\tau}\bar{\dot{\gamma}}. \tag{3.32}$$

From this, it can be seen that perturbation growth will occur when the stress is large and the fluidity is low. Recall that in steady state, $\sigma = \tau\dot{\gamma}$, and the steady state is therefore stable against perturbation growth (or, given the approximations, may be unstable with a very low growth factor, which is too small to overcome diffusion), and so there will be only transient banding. From Eq. 3.2, it can be seen that the criterion for stress relaxation ($\partial_t\sigma < 0$) is identical to condition 3.32, and so we can conclude that the system is linearly unstable to perturbation growth while the stress in the homogeneous base state is a decreasing function of strain. This tells us that only systems with a stress overshoot will be unstable against perturbation growth at any point, and that systems with an overshoot will in general develop shear bands after the overshoot, while the stress is relaxing.

Eigenvalues

We can also examine the eigenvalues directly. For cleanness of notation, we will stop using overbars to describe the steady state (so we will use τ instead of $\bar{\tau}$ etc.). Recall that each eigenvalue describes the growth rate of its mode, and the growing mode corresponds to the positive eigenvalue. From Eq. 3.29, we can calculate that the eigenvalues will be

$$\lambda_{\mp} = \frac{1}{2}\left[-\dot{\gamma} - \frac{1}{\tau} - \frac{1}{\eta} \mp \sqrt{\left(-\dot{\gamma} - \frac{1}{\tau} - \frac{1}{\eta}\right)^2 - 4\dot{\gamma}\left(\frac{1}{\tau} + \frac{1}{\eta}\right) + 4\frac{\sigma}{\tau}\frac{1}{\eta\left(\dot{\gamma}+1\right)^2}}\right], \tag{3.33}$$

which we simplify by assuming that η and $\dot{\gamma}$ are small and τ is large to give

$$\lambda_{\pm} \approx \frac{1}{2}\left[-\frac{1}{\eta}\left(1 \pm \sqrt{1 - 4\dot{\gamma}\eta + 4\frac{\eta\sigma}{\tau}}\right)\right]. \tag{3.34}$$

We can now see that the eigenvalue which becomes positive will be λ_-, and we carry out a binomial expansion of the square root to give

$$\begin{aligned}\lambda_- &\approx \frac{1}{2}\left[-\frac{1}{\eta}\left(1-\left(1-2\dot{\gamma}\eta+2\frac{\eta\sigma}{\tau}\right)\right)\right] \\ &= \frac{1}{2}\left[-\frac{1}{\eta}\left(2\dot{\gamma}\eta-2\frac{\eta\sigma}{\tau}\right)\right] \\ &= \left(\frac{\sigma}{\tau}-\dot{\gamma}\right),\end{aligned} \tag{3.35}$$

which as expected is positive iff the condition 3.32 derived earlier is met.

By examining the ratio $\frac{\sigma}{\tau}$ for the homogeneous state, we can proceed further. We find that this ratio as a function of γ always has a typical shape for all $\dot{\gamma}, t_w$, with a magnitude depending on $\dot{\gamma}$ and t_w. We also find that for a given product $\dot{\gamma}t_w$ the magnitude is directly proportional to $\dot{\gamma}$. This allows us to write it as

$$\frac{\sigma}{\tau} = \dot{\gamma}F\left(\dot{\gamma}t_w\right)A\left(\gamma\right), \tag{3.36}$$

with $A\left(\gamma\right)$ and $F\left(\dot{\gamma}t_w\right)$ two unspecified (although calculable) functions. Close examination of the equations reveals that $F\left(x\right)$ varies slowly.

For total perturbation growth, we need to consider the differential equation which comes from Eq. 3.29:

$$\partial_t \boldsymbol{\alpha} = \lambda_-\left(t\right)\boldsymbol{\alpha}, \tag{3.37}$$

with $\boldsymbol{\alpha}$ the relevant eigenvector, with components which are linear combinations of $\delta\tau$ and $\delta\sigma$. This is solved by

$$\boldsymbol{\alpha} = \boldsymbol{\alpha}_{(t=t_0)}\exp\left(\int_{t_0}^{t_1}\lambda_-\left(t\right)dt\right), \tag{3.38}$$

and so we see that the time integral of the eigenvalue is what determines perturbation growth. Note, however, that our growth matrix is time dependent, and the matrix results used in Eq. 3.38 are only strictly true for time-independent matrices. We proceed with the calculation under the assumption that it will be approximately true, noting the need to verify our results with non-linear simulations. If we assume that there will be a small perturbation at all times, then we are specifically interested

in the integral over the time interval during which the eigenvalue is positive:

$$\int_{t_0}^{t_1} \lambda_- dt = \int_{t_0}^{t_1} -\dot{\sigma} dt = -\Delta\sigma, \tag{3.39}$$

and so because λ_- is exactly the gradient of the stress strain curve, its integral will equal the change in stress over the same period. Because we are considering only the period when the eigenvalue is positive, this integral is then equal to the stress drop of the homogeneous curve, which depends principally on the product $\dot{\gamma}t_w$. This is an important result, and tells that during the linear regime, we are able to completely calculate the magnitude of the perturbation growth from the size of the stress drop after the overshoot. We therefore also expect any phenomena associated with shear banding to also show a dependence on $\dot{\gamma}t_w$.

It will also be useful to consider the effect that diffusion can have on perturbation growth. We find that the perturbation diffuses at a rate

$$\partial_t \delta\tau = -l_0^2 \pi^2 \delta\tau. \tag{3.40}$$

If we assume that the direction of $\boldsymbol{\alpha}$ remains fairly constant in (σ, τ)-space, this damping is transferred directly to $\boldsymbol{\alpha}$ and so our combined perturbation growth equation becomes

$$\frac{\partial_t \boldsymbol{\alpha}}{\boldsymbol{\alpha}} = \dot{\gamma} F\left(\dot{\gamma}t_w\right) A\left(\gamma\right) - \dot{\gamma} - l_0^2 \pi^2, \tag{3.41}$$

which gives a stronger requirement for perturbation growth:

$$\dot{\gamma}\left(F\left(\dot{\gamma}t_w\right) A\left(\gamma\right) - 1\right) - l_0^2 \pi^2 > 0. \tag{3.42}$$

This will in general have the effect of delaying the onset of banding, but also gives a new condition which must be met for any banding:

$$\dot{\gamma} > \frac{l_0^2 \pi^2}{A_{max} F\left(\dot{\gamma}t_w\right)}, \tag{3.43}$$

which gives an l_0-dependent strain rate for a given $\dot{\gamma}t_w$ below which perturbation growth is impossible because any perturbation will diffuse faster than it grows. We will call this strain rate the diffusion limit, and note that because F varies slowly

it will be close to being a line of constant $\dot{\gamma}$, and so the diffusion limit $\dot{\gamma}_{diff} \sim l_0^2$. This seems logical, as diffusion is principally a time-dependent phenomenon, while our analysis has shown that during the linear regime, perturbation growth is mainly strain-dependent. For sufficiently small strain rate, the diffusion will overtake the perturbation growth and prevent the formation of shear bands. This important result tells us that for a fixed l_0, there will be some strain rate below which we see no significant shear banding, and the heterogeneous startup curves will follow the homogenous ones.

We have now seen the system is unstable to perturbation growth when the stress of the homogeneous base state is decreasing in time, and that the perturbation growth during the linear regime is directly related to the size of the stress drop. We therefore expect systems with a larger stress overshoot to show more significant banding. We also find that for any l_0, there is a strain rate-dependent diffusion limit which scales as l_0^2, below which we expect to see no banding. However, we also note that our analysis is only true in the linear regime, makes several approximations, and applies results which only strictly hold for time-independent matrices to a time-dependent matrix. We therefore explore this further in full non-linear simulations, to confirm whether the behaviour we have predicted will occur.

3.4.3 Non-Linear Simulations

Random Noise

We are interested in seeing how heterogeneity and shear banding will affect the system's dynamics. However, if we simply remove the artificial homogeneity constraint and model spatial variation, but start the system in a mathematically exactly uniform spatial state, then every point will evolve in the same way and the system will remain homogeneous. To observe heterogeneity, we therefore have to seed the system with some form of heterogeneous perturbation. These perturbations represent physical phenomena such as thermal effects and rheometer imperfections, and

as such will need to be initially small. These small perturbations can still have a large impact on the global dynamics, however, due to the instability that amplifies heterogeneity into a fully formed shear band.

In this work, we will only seed the first Fourier mode, as it is the one which diffuses most slowly, grows most quickly and is most likely to appear in real physical situations due to device curvature. The typical rheometer geometry which would be used to approximate our geometry would be a Taylor-Couette flow, in which a thin layer of fluid is in between two large cylinders, one of which rotates. This is a good approximation to our protocol, with the exception that the fluid layer is slightly curved. This curvature means that even under homogeneous flow, there is a slight variation in stress across the sample, which is proportional to $1/r^2$, with r the distance from the centre of rotation. For a set-up in which the radius of the cylinders is much larger than the distance between them, this effect is effectively linear, and therefore appears most strongly in the first Fourier mode, with other modes having progressively smaller amplitudes. We will discuss several different methods of seeding, which all have competing advantages and disadvantages.

We will start with the simplest method of seeding, where we prepare the sample with a slight heterogeneity in the local stress field. We will therefore have an initial state of $(\sigma(y), \tau(y)) = (\sigma_0(y), t_w)$, with $\sigma_0(y) = \delta \cos(\pi y/L)$, with δ some small number. This perturbation represents some artefact of the sample preparation, or could represent a non-uniformity associated with the finite time a rheometer takes to reach $\bar{\dot{\gamma}}$.

This approach is appealing in its simplicity, and in the right circumstances does yield interesting results. However, at low strain rates it can be ineffective. To see why, consider two start-up curves with the same value of $\bar{\dot{\gamma}} t_w$, and therefore the same size of overshoot, but with differing strain rates. We know that the system only becomes unstable to perturbation growth near the peak of the overshoot, which happens at fixed *strain* for these scenarios. However, because $\gamma = \dot{\gamma} t$, this occurs at a much later time for the case with lower strain rate (and can be orders of magnitude

later). While the system is evolving towards the stress maximum, however, the perturbation is decaying due to the diffusive term in Eq. 3.3, and this decay happens at a rate independent of strain rate. We therefore find that for sufficiently low strain rates, the perturbation will have been decaying for longer, and often almost to zero, by the time the system is unstable, and this can obscure many phenomena.

Next we should consider what would happen if we seed τ instead of σ, so that the initial state looks like $(\sigma(y), \tau(y)) = (0, \tau_{ini}(y))$, with $\tau_{ini} = t_w(1 + \delta \cos \pi y/L)$, which might represent a non-uniformity in sample ageing. While the mechanism is different, the physics is the same: the coupling between τ and σ means that within a few time-steps the percentage perturbation in each is effectively the same. We can also see how seeding σ would result in a heterogeneous τ: the perturbations in σ are quickly transferred to $\dot{\gamma}$ due to force balance, and this heterogeneity then perturbs τ. We can therefore conclude that the choice of field to seed has little effect on the outcome, and perturbing τ will give the same results as perturbing σ. We therefore only need to perturb one of these fields, and for the rest of this work will choose to seed σ for simplicity.

To get around this problem of noise diffusion, we could instead add a small random perturbation at each time step, which is similar to thermal fluctuations or time dependent mechanical rheometer noise. However, we wish to ensure that this perturbation does not become too large, and that the added noise is not dependent on non-physical simulation parameters, and so we choose at each time step to increase $\sigma(y)$ by $\sigma_n(y) = X_t \delta \sqrt{\Delta t} \cos \pi y/L$, where δ is still a small number, X_t is a random number, chosen for each time-step, in the range $[-0.5, 0.5]$, and Δt is the time step. Because the perturbation can now be positive or negative, the noise will never grow too large.

To understand why the noise is scaled by the square-root of the time-step, we need to examine the statistical properties of the total noise added, $\phi = \sum_t \sigma_n = \delta \sqrt{\Delta t} \cos(\pi y/L) \sum_t X_t$, where the sum is over N time-steps. For cleanliness of notation, we will analyse $\chi = \sum_t X_t$, and this can be done using the central limit

theorem, which tells us that this value will follow a Gaussian distribution [135]. We will first look at the mean of this distribution,

$$\bar{\chi} = N\bar{X}_t = 0, \tag{3.44}$$

which gives us the hoped for result that the mean total noise added is zero. Next we consider the variance of χ, $(\Delta\chi)^2$, which is given by

$$(\Delta\chi)^2 = N\,(\Delta X_t)^2\,, \tag{3.45}$$

and the standard deviation

$$\Delta\chi = \sqrt{(\Delta\chi)^2} = \sqrt{N}\Delta X_t = \sqrt{\frac{t}{\Delta t}}.\frac{1}{\sqrt{12}}, \tag{3.46}$$

with t the total time being summed over. We can now look at the standard deviation of ϕ,

$$\Delta\phi = \delta\sqrt{\Delta t}\cos(\pi y/L)\Delta\chi = \delta\sqrt{\frac{t\Delta t}{12\Delta t}}\cos(\pi y/L) = \delta\sqrt{\frac{t}{12}}\cos(\pi y/L), \tag{3.47}$$

which reveals that the standard deviation of the total noise added is independent of the time step and depends only on total time, which is desired because the time step is a non-physical model feature. However, the standard deviation increases with time, which is as expected as the random motion compounds with time. We therefore see that the total noise added by this method will have a mean of zero, ensuring it never grows too large, and a standard deviation which is independent of the time step, meaning that it depends only on physical parameters.

We can now see why this noise protocol is useful: there is heterogeneity ensured at every time-step, it is always small, and its properties are independent of the time step. However, the trade-off is that with the high degree of randomness introduced, the system is now less predictable. When the system reaches a point where perturbation growth begins, we can't even predict whether the perturbation will be positive or negative, and its magnitude is likely to change on every run. This can be countered by simulating the system multiple times and averaging, although this is computationally

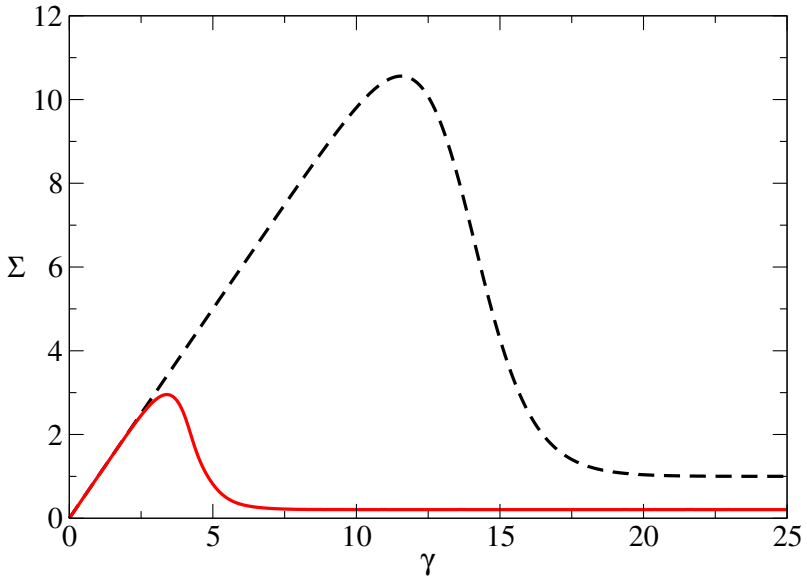

Figure 3.4: Homogeneous (black dashed) and heterogeneous (red solid) start-up curves for a system with $\bar{\dot{\gamma}} = 10^{-4}$, $t_w = 10^{10}$, $\delta = 10^{-3}$. The seeded perturbation gives a shear band with a range which is larger than the imposed shear rate, and so the heterogeneous system fluidises far earlier than might be expected.

expensive.

The magnitude of the noise, which is determined by δ, is also significant. From now on, δ will refer to the quantity define above, and is a simulation parameter. A value of $\delta = 0.01$ is commonly used, and is similar to the variations of 1-10% which are caused by device curvature in experiments. However, to avoid non-linear effects in this model requires that $\frac{\delta}{\eta} \ll 1$. We therefore generally will choose δ to be no larger than 0.01 (and often much smaller) in order to avoid these effects.

It will also be instructive to consider the magnitude of the variation in $\dot{\gamma}$. As we have seen, $\delta\dot{\gamma} = \frac{\delta\sigma}{\eta}$, and due to the seeding $\delta\sigma \approx \delta$, so we see that $\delta\dot{\gamma}$ is independent of strain rate. This is problematic, because it means that taking $\bar{\dot{\gamma}}$ sufficiently low will give us $\delta\dot{\gamma} > \bar{\dot{\gamma}}$ in the unperturbed state, and so the system is seeded with a permanent large shear band in comparison to the shear rate of the background state. There are two possible ways to resolve this: we could take δ to be very low, say 10^{-5}, to avoid this behaviour in a larger range of strain rates. This approach is unsatisfactory, however, because we still have a finite lower limit on strain rate. The alternative is to scale δ with $\bar{\dot{\gamma}}$ so that $\delta \propto \bar{\dot{\gamma}}$, which means that the seeded shear

band is always small compared to the global shear rate. This is appealing because it allows strain rate to be taken infinitely small. To consider the physicality of this, it will be instructive to consider the case where δ is kept constant at low strain rates, as in Fig. 3.4. We then will have situations in which the shearing is very slow, but the system still exhibits a strong shear band immediately which causes the system to fluidise very rapidly, and with only a very small elastic branch. Further, the steady state which the system reaches is *different* to the homogeneous steady state, because the system has some locally negative strain rates. This seems particularly strange when a faster shear rate (with the same $\dot{\bar{\gamma}}t_w$) would prevent this early fluidisation, restore the elastic branch, and ensure the steady state stress is equal to that of the homogeneous system. We therefore consider the scaling of δ to be physically justifiable, and for the rest of the work will use $\delta = 0.01\dot{\bar{\gamma}}$ unless otherwise specified.

The physical origin of the random noise is also important to consider. Adding noise at every timestep, with a δ independent of strain rate, would seem to be a good example of thermal noise; there is some stochasticity in the system caused by local thermal motion. In this scenario, the fact that the seeded shear band is large compared to the global strain rate also seems reasonable, and could be justified by arguing that local thermal motion is faster than shear induced motion (although the neat sinusoidal shape of the noise would be less justifiable). However, while plausible for some materials, this actually indicates why this approach is problematic here. In soft glassy materials, the microstructure which determines the behaviour is typically far larger than the atomic scale, and as such the thermal motion of particles is very slow compared to their size. We should therefore assume that, outside of the strict athermal limit but even at very low strain rates, the shear induced particle motion should dominate over the thermal motion. The case of constant δ is therefore acceptable in this scenario for *thermal, quasistatic* systems (although the model would need to be modified to allow quasistatic simulation), while the situation we have chosen, with δ scaling with $\dot{\bar{\gamma}}$ is for *thermal, finite strain rate* systems, even if that strain rate is slow. This situation, however, is clearly not pure thermal noise.

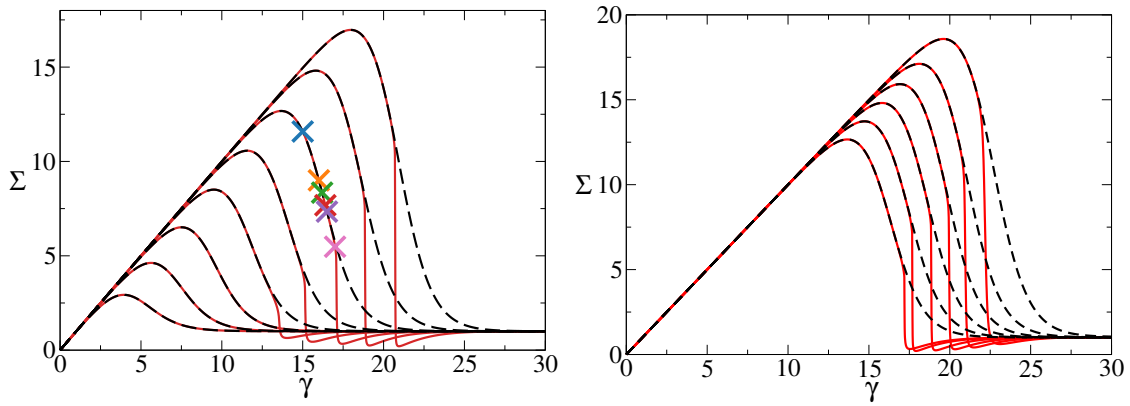

Figure 3.5: Homogeneous (dashed) and heterogeneous (solid) startup curves for $\bar{\dot{\gamma}} = 10^{-3}$ (left) with $t_w = 10^5, 10^6, ..., 10^{12}$, and for $t_w = 10^{11}$ (right) with $\bar{\dot{\gamma}} = 10^{-4}, 3.16 \times 10^{-4}, .., 3.16 \times 10^{-2}$. On the left plot, coloured crosses identify locations of velocity profiles of the same colour in Fig. 3.6a, except for the pink cross which identifies the location of a velocity profile from Fig. 3.6b. In all cases $l = 10^{-3}$ and $\delta = 0.01\bar{\dot{\gamma}}$.

Instead, it should be interpreted as some non-uniformity in molecular velocities, and the assumption that they follow a certain distribution regardless of shear rate.

Heterogeneous Dynamics

We now consider the heterogeneous dynamics in full detail, for which we have used numerical simulations. We will observe that the scenarios in which significant shear banding is observed line up with those predicted on the basis of the linear stability analysis in the previous section, and a few of these start-up curves are shown in Fig. 3.5. This allows us to see the impact of banding on the global stress response: there is a sudden sharp drop-off in the stress, with a (negative) gradient which is steeper than the stress decay for the homogeneous case. This drop-off can be understood as follows: the development of a shear band causes some local strain rates to increase and others to decrease. The critical point is when the strain rate is able to become locally negative: the average of the absolute local strain rate then begins to exceed the average imposed shear rate. This causes the sample to fluidise more rapidly on average than in the homogeneous case, causing a faster stress drop-off. An example of an extremely banded velocity profile, including locally negative shear rates, is shown in Fig. 3.6b. For a single sample, we can define S_{max}, which will be the

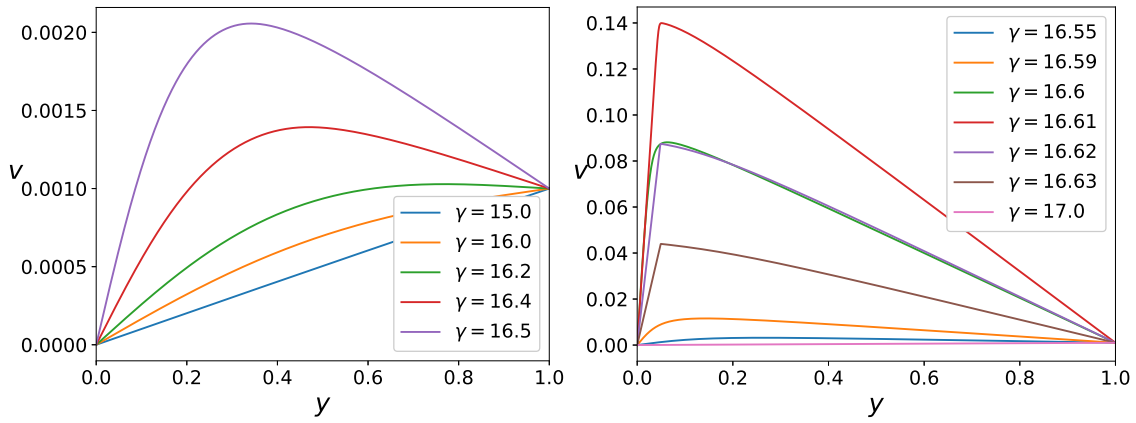

(a) (b)

Figure 3.6: Banded velocity profiles for $\bar{\dot{\gamma}} = 10^{-3}$, $t_w = 10^{10}$ and $l = 10^{-3}$. (a) shows a range 1.5 strain units, and (b) shows half a strain unit during the time in which the profile is extremely banded. The local strain rate, $\dot{\gamma}$, is given by the gradient of these curves.

amplitude of the largest negative gradient of the stress-strain curve during the time simulated. This gives a measure of yielding rate for each sample, which can be averaged across samples with the same parameters but different random seeds. We also define the degree of banding, $B = (\Delta\dot{\gamma})/\bar{\dot{\gamma}}$, with $\Delta\dot{\gamma}$ the difference between the largest and smallest local strain rate. From this, we can define B_{max}, for each sample, which is the largest value of B during the time observed, and this can also be averaged across samples.

As shear banding leads to a fast drop-off in the stress, we might expect large values of S_{max} to be correlated with the regions of instability identified by the analysis in Sec. 3.4.2. Fig. 3.7a, 3.7b show phase space plots of S_{max}, and we can see the predicted trends broadly emerging. The plot with $l = 10^{-2}$ has a cut-off strain rate below which S_{max} returns to a small value, while in the plot with a lower value of l the diffusion limit is not visible. We also see that increasing the product $\bar{\dot{\gamma}}t_w$ leads to a higher value of S_{max}, except below the diffusion limit.

The white lines in Fig. 3.7 show contours of constant overshoot height. Following one of these lines at a large overshoot height (right of the plot), we see that S_{max} increases as the strain rate decreases, and appears to do so without bound. This implies that the sharpness of the yielding increases along these contours, and approaches

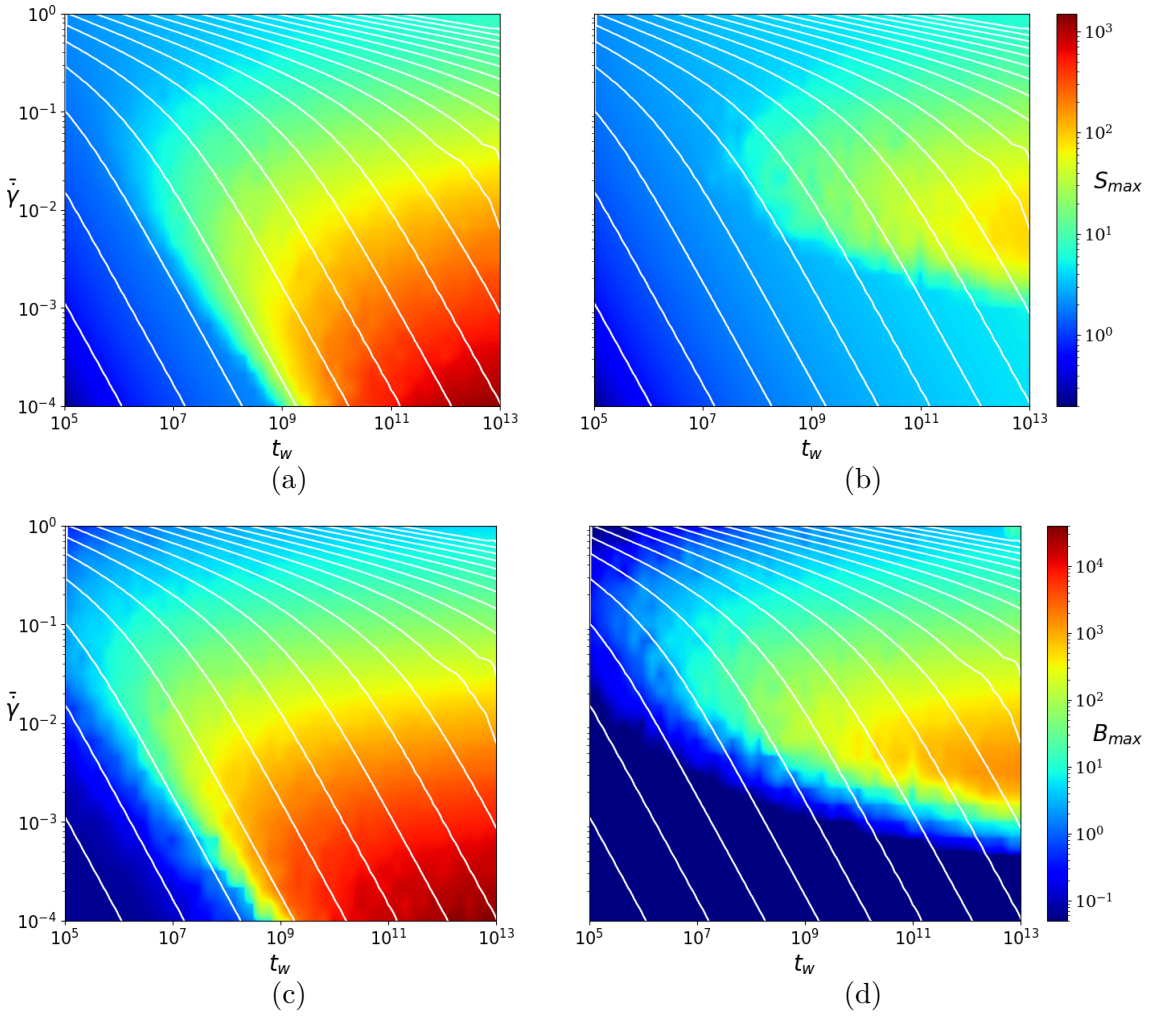

Figure 3.7: Top: Phase space plots of S_{max} for $l = 10^{-3}$ (left) and $l = 10^{-2}$ (right). Bottom: Phase space plots of degree of banding, B_{max}, for $l = 10^{-3}$ (left) and $l = 10^{-2}$ (right). White lines on phase space plots are contours of constant overshoot height.

a limit of infinite steepness (at zero strain rate), which would be experimentally indistinguishable from discontinuous yielding. Note that this was not predicted by the linear stability analysis, and so is likely related to non-linear behaviour. If we instead follow a line of constant low overshoot height (bottom left), we see that S_{max} is small and remains constant. This implies that in that regime, we have only slow, smooth yielding, regardless of strain rate. We consider the case in which S_{max} is large to be "brittle" yielding, and the case of low S_{max} to be "ductile" yielding, although we do not define a precise threshold in S_{max} to differentiate between them, as this would necessarily be somewhat arbitrary. Instead, we describe samples as

showing brittle yielding when $B_{max} > 1$, as this indicates that significant shear bands form, and the failure is therefore initially strongly localised. Examination of Fig. 3.7 reveals that following this criterion, we do indeed see that samples which exhibit brittle yielding have a high S_{max}, and for those showing ductile yielding it is low.

While phase space plots allows us to see general trends, it will also be instructive to examine some slices across them, as in Fig. 3.8. It can be seen from Fig. 3.8(b) that at low t_w, S_{max} increases only slowly with increasing t_w, following the homogeneous trend, and then at a $\bar{\dot{\gamma}}$-dependent t_w it starts to increase very rapidly. Comparison with Fig. 3.8(d), which shows the degree of banding for the same parameters, reveals that the much sharper gradients occur when the degree of banding, B_{max}, is larger than some cut-off, which is slightly above 1. This is as expected because the degree of banding exceeding 1 indicates that there is some material with a negative local shear rate.

It will also be instructive to examine the case where $\dot{\gamma}$ is increased at constant t_w, as in Fig. 3.8(a,c). Now it can be seen that S_{max} appears to increase as $\bar{\dot{\gamma}}$ decreases, until it reaches a limiting point where the perturbation growth is too small to generate locally negative shear rates. However, this limiting point is dependent on t_w, so if we were to examine the limit of infinite sample age, S_{max} could increase without limit as $\bar{\dot{\gamma}}$ decreases, until the diffusion limit. From this we can conclude that an infinitely sharp stress drop-off would be the limiting behaviour in the case of infinite t_w, zero strain rate and no diffusion.

We have now seen that the behaviour predicted by the linear stability analysis has broadly emerged, including more severe banding for samples with a larger stress overshoot and an l_0-dependent strain rate below which perturbation growth is suppressed. We have also seen several interesting new phenomena relating to the non-linear behaviour, including the observation that $S_{max} \to \infty$ as $\bar{\dot{\gamma}} \to 0$ at fixed overshoot height.

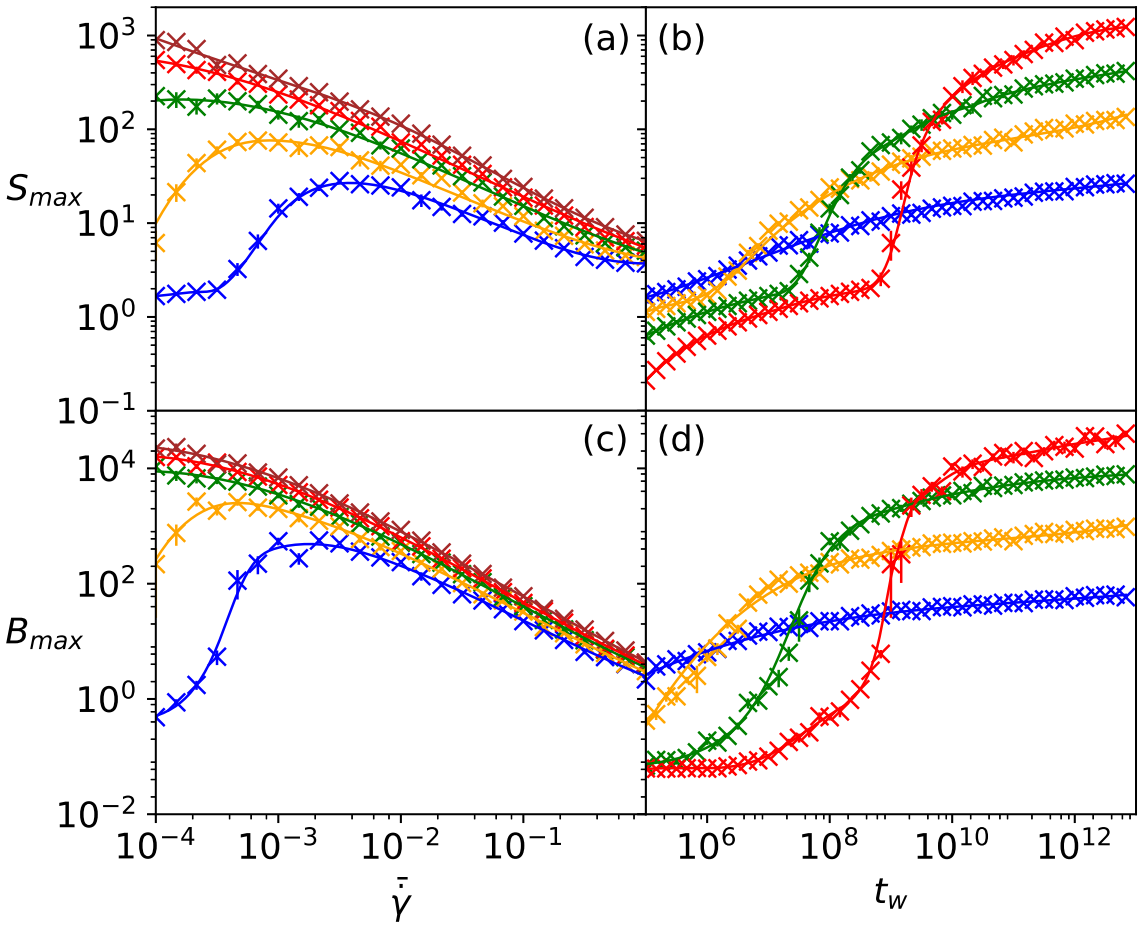

Figure 3.8: Slices of the phase space shown in Fig. 3.7a, with fixed $t_w = 10^8, 10^9, .., 10^{12}$, blue to red increasing t_w, (left) and fixed $\dot{\bar{\gamma}} = 10^{-4}, 10^{-3}, 10^{-2}, 10^{-1}$, blue to red increasing shear rate, (right), showing S_{max} (top) and B_{max} (bottom).

3.5 Discussion

We have seen that shear banding leads to a fast drop-off in stress, and that its occurrence is broadly correlated with regions of phase space in which we expect significant banding. However, it is also interesting to note that there appears to be a continuum of yielding rates. Some startup curves, generally those with minimal banding, have a slow stress drop off, which we will refer to as "ductile yielding", while in others the stress drops off exceptionally fast, which we call "brittle yielding". Crucially, while these two extreme behaviours are qualitatively distinguishable, there is also a continuum of intermediate yielding speeds. Fig. 3.9 shows a specially chosen selection of startup curves for which the yielding is easily comparable, as the parameters are chosen to give identical stress overshoot sizes. In the left plot,

the stress drop is large and the smooth variation of yielding is clearly visible. It can be seen that the brittle and ductile yielding are the two extremes of a common phenomenon. In fact, it is difficult to robustly define ductile and brittle yielding separately based only on the stress-strain curve, as this would require the imposition of an artificially chosen threshold value of S_{max}. In comparison, the right plot shows a small stress drop, and in this situation, only ductile yielding is observed. We therefore see that although a range of yielding speeds is in general possible, the brittle yielding is only possible for a large stress overshoot. However, note that the parameters used in Fig. 3.9 are very carefully chosen, and while they are helpful here for instruction, it would be unusual to generate such a plot from regular experimental data.

Brittle yielding in general takes place at low strain rates and at high t_w (and low l). This is actually the result of two separate processes: a sample with higher $t_w\bar{\dot{\gamma}}$ fluidises more slowly, and therefore has a longer elastic branch. It follows that when the sample starts to yield, more stress has built up, and this drives a more rapid fluidisation. This correlation is related to the homogeneous dynamics, and occurs even when the system is artificially constrained to homogeneous flow. When the system is allowed to flow heterogeneously, we find an additional phenomenon: the rate of perturbation growth in the non-linear regime is, broadly speaking, time-dependent rather than strain-dependent, so at low strain rates significant shear bands can develop in a much smaller strain window following the start of the yielding. As discussed above, this banding can lead to locally negative shear rates, which causes the system to fluidise much more rapidly on average.

While the authors of [43] find that brittle yielding is accompanied by a discontinuous stress drop, and therefore separated from ductile yielding by a critical point, we find that brittle yielding occurs with a finite, although very fast, stress drop, of which a limiting case is a discontinuous stress drop. We therefore find that there is no need for a stress overhang or a random critical point, and ductile and brittle yielding both occur in systems with a stress overshoot.

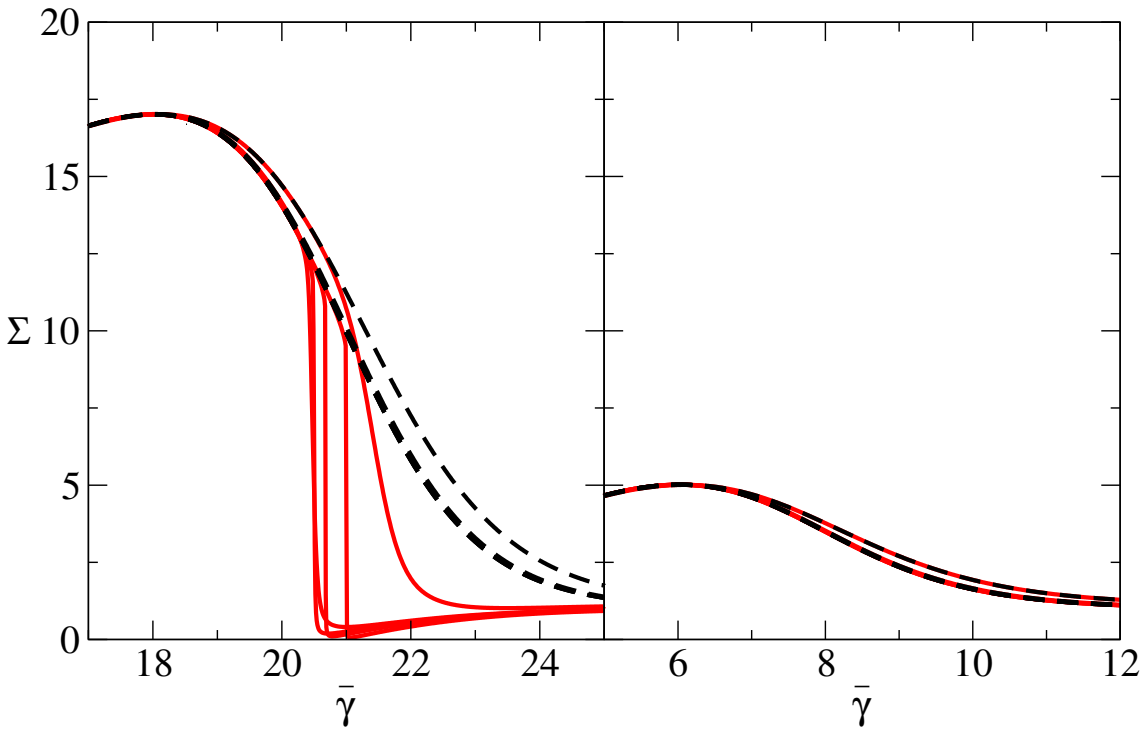

Figure 3.9: Stress-strain curves for constant overshoot height $\Sigma_{max} = 17.0$ (left) and $\Sigma_{max} = 5.0$ (right), with strain rates $\dot{\bar{\gamma}} = 10^{-5}, 10^{-4}, ..., 10^{-1}$. The ageing times are chosen so that the peak of each curve is at the same height, in order to make it easier to compare them. These curves do not correspond to a straight line slice of the phase space considered above.

3.6 Conclusion

We have introduced a fluidity model of soft glassy fluids, and considered its dynamics under a shear startup protocol. In Section 3.4.1 we considered the dynamics of the system when constrained to flow homogeneously, and found that for sufficiently high $\dot{\bar{\gamma}} t_w$, the system exhibits an elastic branch, before yielding into a fluid-like state. We also found that the strain at which the stress is at a maximum is dependent only on the product $\dot{\gamma} t_w$.

In Section 3.4.2, we considered the system's linear instability to perturbation growth, and identified typical parameter values in which this is likely to lead to shear banding. We found that in the linear regime, perturbation growth is directly related

to stress relaxation, and that systems with a larger stress overshoot are therefore more likely to show significant banding.

In Section 3.4.3 we then carried out heterogeneous, non-linear simulations of the system, and found the regions of parameter space which lead to shear banding broadly line up with the predictions of our linear stability analysis, although samples which showed significant banding entered a non-linear regime in which the linear stability analysis was no longer able to accurately predict behaviour. We also saw that there is a range of rates at which the system can yield, and found that the extreme cases of ductile and brittle yielding are simply two extremes of a continuum of yielding rates for a single phenomenon. We find also that for our model, brittle yielding is only possible with a large stress overshoot, while ductile yielding can occur for any size of overshoot.

We have seen that for a large stress overshoot, decreasing the strain rate appears to increase the sharpness of the yielding transition indefinitely. However, we note also that this only strictly true in the case $l_0 = 0$, as for finite l_0 we have a strain rate below which perturbation growth is damped. Therefore, although we make predictions for the model's behaviour as strain rate goes to zero, these predictions are not strictly true in the quasistatic limit.

This work has successfully built on that done in [35] exploring the transient shear banding in this model. It is, however, in disagreement with the conclusions drawn in [43] that "brittle" and "ductile" yielding are two distinct phenomena, and the work in [45], which finds a discontinuity in the stress response during elastoplastic yielding. We can compare our brittle and ductile yielding to those in [43], and we find that, in our model at least, they are two facets of the same process, differing only quantitatively. We find that precipitous yielding can occur with an arbitrarily steep gradient in the stress response, while these former works find that there is some threshold beyond which there are discontinuities in the stress response. However, we note that, in contrast to these works, our simulations were thermal at finite strain rate.

These results can also be compared to additional results presented in [44] for athermal systems. This work found that at low strain rates, heterogeneous athermal systems with a stress overshoot always show brittle yielding, regardless of the size of the overshoot, and ductile yielding is therefore only possible at high strain rate. This implies that the ductile yielding we see for samples with a small overshoot height is related to thermal effects, which in some way slow down the yielding. The precise nature of the transition between the athermal and thermal cases remains unstudied.

Chapter 4

Delayed Yielding in the Soft Glassy Rheology Model in Large Amplitude Oscillatory Shear

4.1 Introduction

Common experience tells us that many materials can be deformed many times in a similar way, before eventually breaking; for example a plastic chair might be sat on hundreds of times with no apparent problems, before suddenly breaking the next time. The process of fatigue in solids following repeated cyclic loading has been extensively studied in an engineering context [46–48], and it is widely accepted that repeated loading and unloading of a wide range of materials causes the development of weaker areas and cracks, which then propagate across the material, leading to macroscopic failure [46–50]. The process by which small regions of a material slowly weaken is known as material fatigue, and has been shown to occur over a large number of loading cycles [49]. The process of crack propagation in solids has been connected to the relaxation of elastic stress through local yielding events [49, 136] and to noise-induced heterogeneity, which causes the stress on small regions of a material to exceed the yield stress while the material-averaged stress is still below

this threshold [137]. However, the focus within the engineering literature has been on materials that are elastic solids until some maximum stress or strain, at which point they fracture. We wish to consider here a wider class of materials, which are able to show solid-like, fluid-like and plastic behaviour, and as a result can yield without fracturing.

Many of the materials that show this behaviour can be characterised as soft and/or glassy [138], and in this work we explore this phenomenon theoretically. It is widely accepted that soft glassy materials show a solid-fluid transition under shear [12, 13, 38, 42, 91, 114, 115, 131, 139–143]. Experimental work has applied large amplitude oscillatory shear (LAOS) protocols to a range of soft glassy materials [53] including foams [51], gels [52, 54, 58], emulsions [52, 55, 61], wormlike micelle solutions [54], polymer solutions [55, 56] and colloidal glasses [57, 59, 60]. These experiments have revealed a range of non-linear behaviour, including solid-fluid transitions, yielding processes and growth of heterogeneity in the strain and strain-rate fields. Solid-fluid transitions transform a material from a solid-like state, in which stress is proportional to strain, to a fluid-like state, in which stress is a function of strain rate. In yielding events, for a strain-controlled protocol, the stress suddenly decreases substantially, while in a stress-controlled process, the strain suddenly increases substantially. In the experiments of Ref. [51], a solid fluid transition emerges as the oscillation amplitude increases, while experiments with colloidal gels [63] showed that this yielding can happen after thousands of shear cycles. In Ref. [64] the authors connected delayed yielding with either a power law or exponential fit of the time until yielding as a function of the stress amplitude. LAOS protocols therefore clearly provide a rigorous way of exploring this every day process with which we are familiar, and so we will explore the process of delayed yielding under LAOS, in which a solid-fluid transition happens after a large number of strain cycles.

Previous studies of the Soft Glassy Rheology (SGR) model under LAOS [65, 66] found transitions from solid-like to fluid-like behaviour, with a fluidised steady state

featuring strong shear bands. Ref. [65] explored the criteria for yielding transitions under LAOS, and showed that they only occur for amplitude greater than some threshold, but for arbitrarily low frequency.

However, to the author's knowledge, no previous work has explored theoretically the number of shear cycles before yielding under LAOS, or the process by which that yielding occurs, in either the SGR model or any other model of soft materials. In this work, we use the SGR model to explore both of these questions. In particular, we will explore the way in which yielding can occur suddenly over a small number of cycles after a very large number of cycles. We will also attempt to identify precursors to yielding, which has wide reaching real world applications: a good understanding of the precursors to yielding could allow engineers to identify when a material is likely to fail, even if there is no obvious indication from its macroscopic stress-strain relationship.

4.2 Model

We use the SGR model [36,37,144,145], which considers an ensemble of elastoplastic elements, each of which represents a mesoscopic spatial region of material. These regions are small enough that a macroscopic material contains a large number of them, meaning that we can describe material properties using an ensemble average. They are also large enough that we can meaningfully define a local elastic strain. Typically, therefore each mesoscopic region must contain at least a few of the material's constituent building blocks (foam droplets, colloidal particles etc.).

Each element has a local elastic strain, l, and a local yield energy, E. The elastic strain increases as the system is sheared at a rate $\dot{l} = \dot{\gamma}$, where $\dot{\gamma}$ is the applied strain rate, allowing local deformation to build up. As elements are strained, they gain stress Gl and energy per unit volume $\frac{1}{2}Gl^2$, where G is the microscopic shear modulus. We work in stress units where $G = 1$.

Each element then stochastically hops out of its energy well at a rate Γ, which is determined by the difference between the accumulated elastic strain energy and the local yield energy. This hopping rate is given by

$$\Gamma\left(E,l\right)=\Gamma_0\min\left\{\exp\left[-\frac{E-\frac{G}{2}l^2}{x}\right],1\right\}, \tag{4.1}$$

where x is an effective noise temperature and Γ_0 is the microscopic hopping rate. We work in time units where $\Gamma_0=1$. The hopping rate is given a maximum value of Γ_0 following the recommendations in [146] in order to ensure the model remains thermodynamically consistent.

In materials in which the thermal energy is of the same order of magnitude as the energy well depths, such as metallic glasses, the temperature parameter, x, is generally interpreted as the true thermodynamic temperature, with $x=k_BT$ [146]. For systems such as foams and emulsions, the energy barriers generally relate to the stretching and rearrangement of films and interfaces, and as a result are typically much larger than the thermal energy [16, 17, 19, 20, 147]. In these systems, x is an effective noise temperature, which is not connected to thermodynamic temperature, but is related to the mechanisms which allow stress fluctuations to propagate across the material.

After yielding, the local elastic strain of an element is reset to $l=0$, and a new energy well depth is chosen from an exponential distribution,

$$\rho\left(E\right)=\frac{1}{x_g}e^{-\frac{E}{x_g}}, \tag{4.2}$$

where x_g is the glass transition temperature [148]. We set $x_g=1$, which corresponds to setting the local yield strain amplitude. To calculate the stress in the system, we take an ensemble average of the local elastic stress, so that

$$\sigma=\frac{G}{n}\sum_{i=1}^{n}l_i, \tag{4.3}$$

where n is the number of elements and the sum is over elements.

In the limit of an infinite number of elements, the probability distribution of the

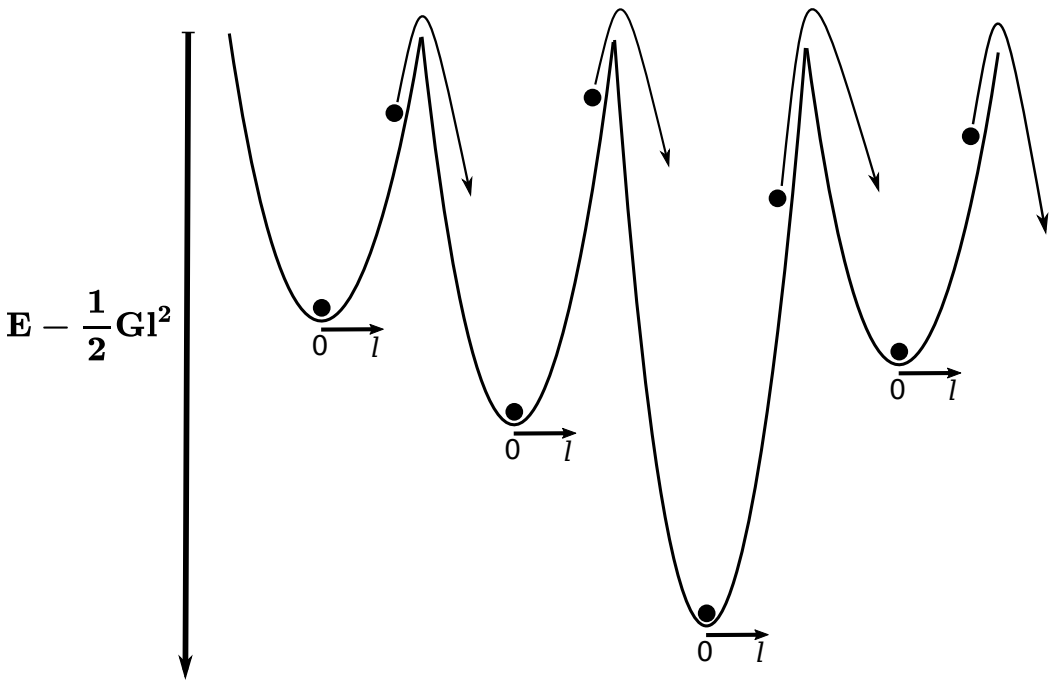

Figure 4.1: Sketch of the behaviour of the SGR model [36, 37, 144, 145]. Elements are in traps of depth E, and gain local strain energy $\frac{1}{2}Gl^2$ as they are deformed at a rate $\dot{l} = \dot{\gamma}$. Elements have a probability of hopping out of their well at any time, and this probability is a decreasing function of the energy gap to the top of the well and depends on the noise temperature, x. After hopping, each element returns to $l = 0$ and a new energy well depth E is chosen from the distribution $\rho(E) = \frac{1}{x_g} e^{-E/x_g}$. Figure is adapted from [36, 145]

system, $P(E, l; t)$ is governed by the equation

$$\dot{P} + \dot{\gamma}\partial_l P = -\Gamma(E, l) P + \rho(E) \delta(l) Y(t), \tag{4.4}$$

with $\delta(x)$ the Dirac delta function and $Y(t)$ the ensemble average hopping rate, given by

$$Y(t) = \int \Gamma(E, l) P(E, l; t) \, dE dl. \tag{4.5}$$

The second term on the left hand side of Eq. 4.4 describes elements' local strain growing as the system is sheared. The first term on the right hand side describes elements yielding, and the second term on the right hand side describes the selection of new energy well depths.

We therefore have a model that for small strains, $\frac{1}{2}Gl^2 \ll E$, and zero temperat-

ure, $x = 0$, behaves effectively elastically, whereas at large enough strains, elements approach the edge of their traps and start to yield locally, allowing the stress in the system to relax plastically. It is therefore possible for the system to reach a state of steady stress while under continuous shear. At finite temperature, the same behaviour is broadly observed, but it is now possible for elements to yield for any value of l. The behaviour of elements is sketched in Fig. 4.1 to illustrate this.

The resulting behaviour of the model depends on the value of the noise temperature, x, and we find that the flow curve (see Ch. 2.2.2) has three regimes [149]:

$$\begin{aligned} &\text{Newtonian flow regime: } \sigma \propto \dot{\gamma} \text{ for } x > 2 \\ &\text{Power law fluid regime: } \sigma \propto \dot{\gamma}^{x-1} \text{ for } 1 < x < 2 \\ &\text{Glass phase: } \sigma - \sigma_y \propto \dot{\gamma}^{1-x} \text{ for } x < 1 \end{aligned} \tag{4.6}$$

As can be seen, below the glass transition temperature, the model predicts yield stress fluid behaviour.

We follow Ref. [149] and initialise the system with the probability distribution $P_0(E) = \rho(E)$, which corresponds to the steady state of the system in the limit $x \to \infty$ and is also the distribution which maximises the system's entropy. We then apply a deep quench to the system, and instantaneously set the temperature to some finite working temperature within the glass phase, $x < x_g$. If the system then remains at rest in the glass phase, it shows rheological ageing [149], and the ensemble hopping rate, $Y(t)$, decreases with time, causing the system to become more solid-like. In principle this ageing can continue forever, although in practice simulating a finite number of elements limits the level to which a system can age. Previous studies [35, 44, 145, 149–152] have shown that within the glass phase, the system's age prior to shear is a key parameter in determining the system's subsequent behaviour under shear.

So far we have considered the behaviour of an ensemble of elements assuming uniform shear is applied to all elements, but have not considered any spatial variation

in the shear rate. We now extend this model into a 1D form, allowing spatial variation of the shear rate field in the flow gradient direction, y. The system is now divided into n streamlines, each of which has m elements, where m still needs to be large so that ensemble averages can be taken for each streamline. Throughout this work, we have $n = 25$ streamlines of $m = 10,000$ elements each. We find that increasing m has no noticeable impact on the dynamics of the system, although for lower $m \approx 1,000$, there are some changes to the results, particularly near transition points. We find that varying n has no noticeable impact on the number of cycles before yielding, but can have a small impact on the rate at which a sample yields. Each streamline has a local strain rate, $\dot{\gamma}_j$, which obeys

$$\frac{1}{n}\sum_{j=1}^{n}\dot{\gamma}_j = \dot{\bar{\gamma}}, \tag{4.7}$$

where $\dot{\bar{\gamma}}$ is the imposed strain rate which is applied to the system. We can also calculate the elastoplastic stress on any streamline as

$$\sigma_j = \frac{G}{m}\sum_{i=1}^{m} l_{ij}, \tag{4.8}$$

where l_{ij} is now the elastic strain of the i-the element in the j-the streamline.

We then consider the elastoplastic elements to be immersed in a background Newtonian solvent, of viscosity $\eta \ll 1$ (in our units in which $G = \Gamma_0 = 1$, and we use $\eta = 0.05$ throughout. For the j^{th} streamline, the total stress, Σ_j, is then composed of an elastoplastic contribution from the SGR elements and a viscous contribution from the solvent, so that

$$\Sigma_j = \sigma_j + \eta\dot{\gamma}_j. \tag{4.9}$$

We assume small Reynolds number, which means that the total stress must be spatially uniform, $\partial_y \Sigma\,(y) = 0$, and so the total stress in the system, Σ, obeys

$$\Sigma = \frac{1}{n}\sum_{j=1}^{n}\Sigma_j = \frac{1}{n}\sum_{j=1}^{n}\sigma_j + \eta\dot{\bar{\gamma}}. \tag{4.10}$$

This allows us to calculate the global stress. We then calculate the local strain rate of each streamline, given the local elastoplastic stresses and the imposed strain rate,

by recalling that for a spatially uniform system,

$$\Sigma_j = \Sigma, \tag{4.11}$$

and therefore that

$$\sigma_j + \eta\dot{\gamma}_j = \frac{1}{n}\sum_j \sigma_j + \eta\dot{\bar{\gamma}}. \tag{4.12}$$

This has the net effect that a streamline with a higher elastoplastic stress than its neighbours will flow at a lower strain rate than those neighbours. This allows the stress to propagate across the sample on a timescale determined by η, in a manner that reproduces the 1D projection of the Eshelby propagator [153].

Finally, we need to couple adjacent streamlines together to allow some diffusion of stress, as discussed in Ref. [121]. If we do not include some form of diffusion, there will be no significance to the location of streamlines within the sample, and spatially-heterogeneous effects will occur on the scale of the spatial grid, with the strain rate of each streamline independent of the strain rates of adjacent streamlines (within the limit of Eq. 4.12). Including a diffusive term couples adjacent streamlines together, and ensures that heterogeneous effects occur in spatially localised regions on a length-scale determined by the diffusion coefficient. To do this, each time an element yields, we choose three elements at random from each of the neighbouring streamlines and adjust their local strains by $w\Delta l\,[-1, +2, -1]$, where Δl is the change in local strain of the element that yielded during the yielding event and w is a small diffusivity parameter, which we set to $w = 0.05$. This acts as a diffusive term [44], and causes stress heterogeneity in the sample to be diffused, with the most strong damping on higher Fourier modes. It therefore plays an analogous role to the $l_0^2\partial_y^2\tau$ term in the model presented in Ch. 3.

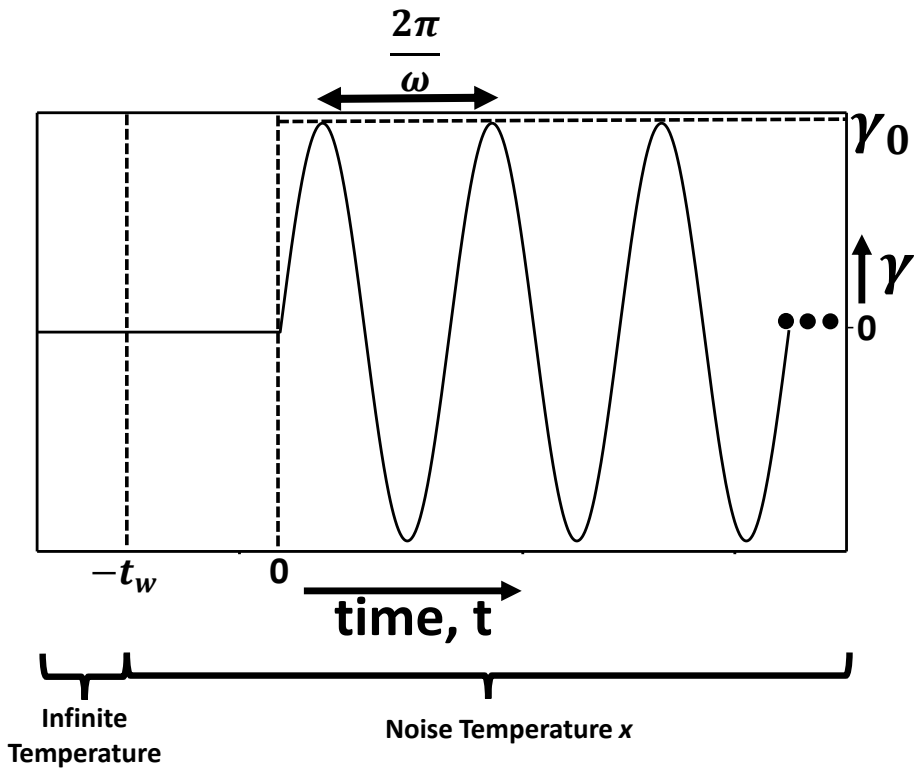

Figure 4.2: Sketch of the shear protocol. The sample is first equilibrated at infinite temperature, then instantaneously quenched to a finite working temperature, x. Next, it is aged without shear for a time t_w, before an oscillatory strain of amplitude γ_0 and frequency ω is applied. The oscillatory strain is applied for many more cycles than are shown here.

4.3 Shear Protocol

As described above, we have a model in which we apply a global strain rate and are able to measure the resulting stress. We first equilibrate at $x = \infty$, then instantaneously quench at time $t = -t_w$ to a working temperature $x < x_g$, within the glass phase, where the model shows rheological ageing. The system is then allowed to age for a time t_w without any applied shear. The parameter t_w therefore describes the degree of annealing, and a larger t_w will correspond to a more solid, better annealed sample.

At time $t = 0$, we begin to shear the system, applying a LAOS, strain controlled protocol. We apply an imposed strain rate $\dot{\bar{\gamma}} = \gamma_0 \omega \cos(\omega t)$, with ω the angular frequency and γ_0 the oscillation amplitude. This protocol is sketched in Fig. 4.2. A cosine strain rate signal is chosen so that the applied strain is continuous and centred:

it follows $\gamma = \gamma_0 \sin(\omega t)$, so that $\gamma(t = 0) = 0$, and the strain cycles between positive and negative. Throughout this work, we set $\omega = 10^{-1}$ for computational efficiency, which corresponds to low frequency but is far from the quasistatic limit. We have also explored $\omega = 10^{-2}$, which shows qualitatively similar results.

The oscillation amplitude, γ_0 is an important parameter which will be varied throughout this work. To be within the LAOS regime, we require a sufficiently large amplitude that non-linear behaviour is commonly observed [154, 155]. For the SGR model, this means that elements are frequently close to the edges of the energy wells, $\frac{1}{2}Gl^2 \approx E$. The expected value of E after a relaxation event is given by

$$\bar{E} = \int \rho\left(E'\right) E' dE' = x_g, \tag{4.13}$$

and so we require that in each cycle, elements are able to build up enough strain to come close to that mean value. The maximum local strain increase in a cycle is exactly the oscillation amplitude, so this corresponds to

$$\gamma_0 \gtrsim \sqrt{\frac{2x_g}{G}} = \sqrt{2}. \tag{4.14}$$

We will in general use $\gamma_0 > 1$, noting that the LAOS regime cannot be rigorously defined by a precise threshold amplitude. We will also see a change in behaviour around $\gamma_0 \approx \sqrt{2}$, and we want to see both sides of this transition.

We model shear of a sample between two flat parallel plates, of infinite extension in the flow direction, x, and the vorticity direction, z. The plates are separated in the y-direction by a distance L. We choose units of length in which $L = 1$. We assume the sample to be infinite and homogeneous in the x- and z-directions, and only allow heterogeneity in the y-direction. The assumption of infinite extensions requires that for each streamline, we model enough elements that the distribution of E and l is a very close approximation to the probability distribution described by Eq. 4.4. Applying the oscillatory shear protocol corresponds to fixing the bottom plate while moving the top plate in the positive and negative x-directions. This is similar to a Taylor-Couette rheometer geometry in the limit of small gap size, as in

previous chapters.

We need to ensure that there is some variation in the system so that if it is unstable against the growth of heterogeneity, there will be a perturbation that is able to grow. Without any variation in the system, any unstable modes will have zero amplitude, and so will still be unable to develop. To generate variation, we seed the system with a small sinusoidal perturbation, by adjusting the energy well depths after ageing. Each energy well is adjusted to $E = E_0 (1 + \delta \cos 2\pi y)$, with E_0 the energy well depth before the adjustment and δ the size of the perturbation. We use $\delta = 10^{-2}$ throughout. The fact that there are a finite number of elements on each streamline ensures that there is some stochastic variation between streamlines at all times, and we find that maintains enough heterogeneity in the system that we do not need to continually add additional noise.

While applying this protocol, we can measure the response of the system both within each oscillation cycle and as a function of the number of oscillation cycles. As we are particularly interested in yielding that occurs after many cycles, we will principally follow the latter, and define N as the number of complete oscillation cycles that have been carried out. We define $\Sigma_{\mathrm{RMS}}(N)$ for a given cycle, which is the root-mean-square of the stress during that cycle. To measure heterogeneity, we define the degree of banding at any point in time, $\Delta\dot{\gamma}(t)$, as the standard deviation of the strain rate across the sample,

$$\Delta\dot{\gamma}(t) = \sqrt{\frac{\sum_{i=1}^{n} \left(\dot{\gamma}_i - \dot{\bar{\gamma}}\right)^2}{n}}, \tag{4.15}$$

and $\langle\dot{\gamma}\rangle(N)$ as the mean of $\Delta\dot{\gamma}$ during a cycle.

4.4 Results

The basic phenomenon that we report is illustrated in Fig. 4.3. We see an initial, pre-failure regime, in which stress is almost constant. Then, after some number of

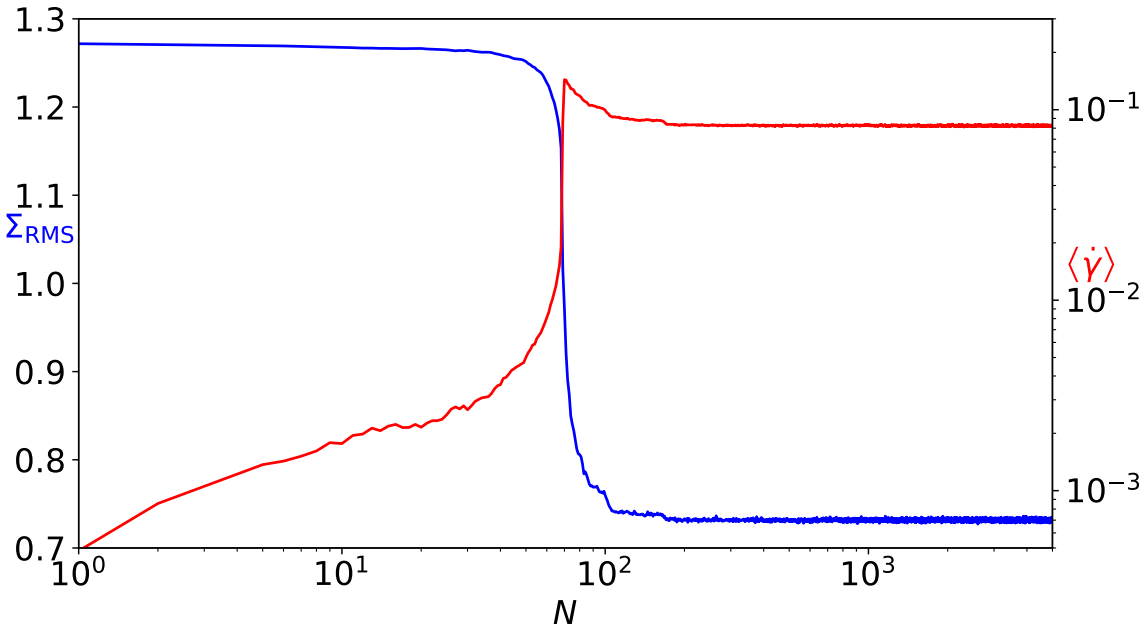

Figure 4.3: RMS stress (blue) and mean degree of banding (red) around each cycle as a function of number of cycles for $t_w = 10^7$, $\gamma_0 = 1.8$. For this sample, the cycle number at yielding $N^* = 70$.

cycles $N^* = 70$, the system suddenly yields dramatically over just a few cycles, and the stress drops to a much lower value. Then in the post-failure regime, the stress is almost constant again, but now at a lower value than initially.

Examining the degree of banding for the system reveals some insight into the process. During the pre-failure regime, although stress is effectively constant, we see that heterogeneity is gradually building up. Then, as the sample fails, the degree of banding increases very rapidly at the same time as the stress relaxes, suggesting that these processes are very closely linked. The degree of banding then also stabilises to an approximately constant value, which is higher than its value before yielding.

To quantify this delayed yielding, we define N^* as a measure of the cycle number in which yielding occurs. To calculate this, we first find the cycles in which Σ_{RMS} is at its global maximum and global minimum as a function of cycle number, N. If the minimum occurs before the maximum, we argue that the sample does not show yielding for the parameter values in question, and do not define an N^*. If the minimum is after the maximum, we define a threshold stress as the midpoint between the two, and N^* is then the first cycle in which Σ_{RMS} is below that threshold,

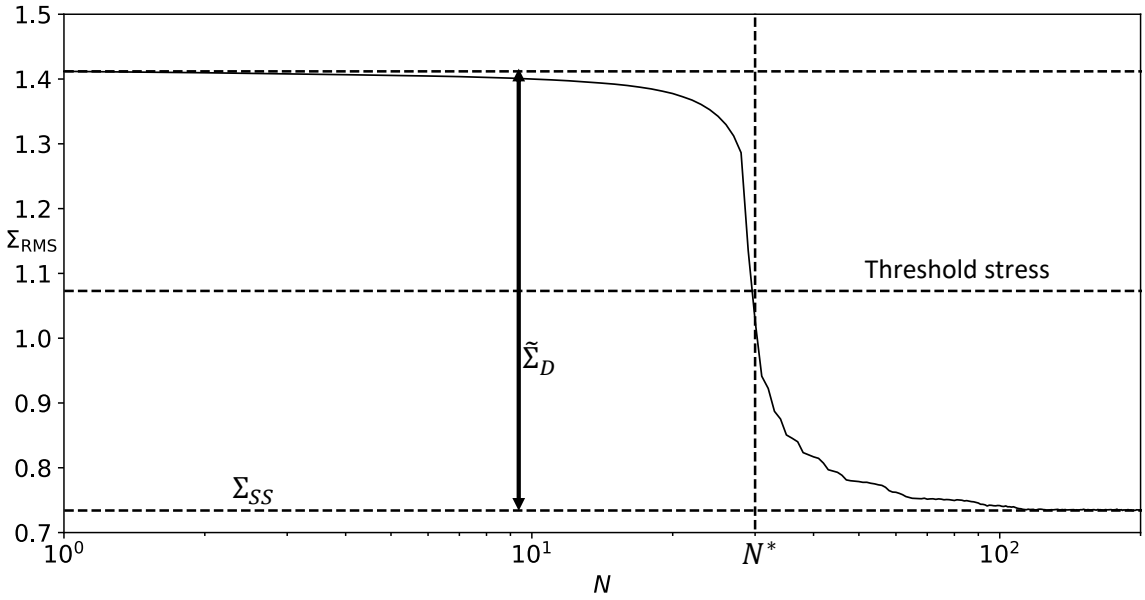

Figure 4.4: Root-mean-square stress, Σ_{RMS} as a function of cycle number N for one sample, with important quantities labelled. $\tilde{\Sigma}_D$ is the size of the stress drop and Σ_{ss} is the steady state stress, which allows calculation of the normalised stress drop, $\Sigma_D = \tilde{\Sigma}_D/\Sigma_{\mathrm{ss}}$. The threshold stress is the midpoint between the maximum and minimum of Σ_{RMS}, and the yielding cycle, N^*, is the first cycle in which Σ_{RMS} is less than the threshold stress and remains below it.

and remains below the threshold until the stress minimum. Note that the minimum possible value of N^* is $N^* = 2$. To characterise the magnitude of the observed yielding phenomenon, we define $\tilde{\Sigma}_D$, which is simply the difference between the maximum and minimum values of Σ_{RMS}, and $\Sigma_D = \tilde{\Sigma}_D/\Sigma_{\mathrm{ss}}$, where Σ_{ss} is the final value of Σ_{RMS}. Fig. 4.4 shows a sketch of all of these quantities for a single sample.

To examine this behaviour in more detail, we now turn to Fig. 4.5, which on the left shows both Σ_{RMS} and $\langle\dot{\gamma}\rangle$ as a function of cycle number, N, for $t_w = 10^7$ and various strain amplitudes, γ_0. Within the range of strain amplitude $1.5 \leq \gamma_0 \leq 2.5$, we see clear and significant delayed yielding, and the cycle in which the sample fails, N^* is larger for smaller amplitudes. For the larger amplitude $\gamma_0 = 2.75$, we see that the sample does yield, but this begins in the first cycle, and so the effect cannot be considered as delayed yielding. For smaller amplitude, $\gamma_0 \leq 1.25$, we do see a late stress drop, but the magnitude is very small. For this reason, we also introduce a threshold, $\Sigma_D > 0.1$, which we justify below by referring to Fig. 4.8, and will not consider samples below this threshold to show yielding. Also of note is that

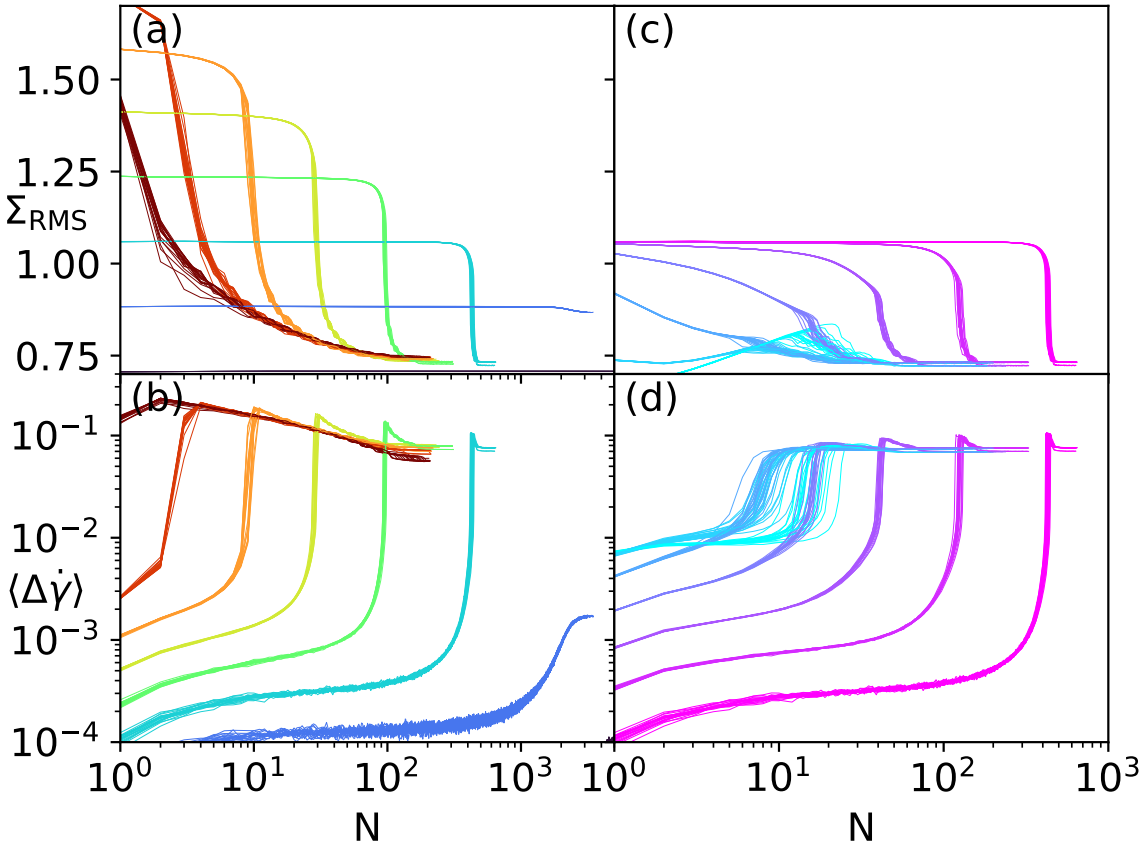

Figure 4.5: Root-mean-square stress, Σ_{RMS} (top) and mean of banding during a cycle, $\langle\dot{\gamma}\rangle$ (bottom) as a function of cycle number N. Left: waiting time $t_w = 10^7$ and strain amplitudes $\gamma_0 = 1, 1.25, ..., 2.75$ in curve sets right to left, blue to red. Right: strain amplitude $\gamma_0 = 1.5$ with waiting time $t_w = 10^1, 10^2, ..., 10^7$ in curve sets left to right, blue to pink. Within each set, each curve corresponds to a different random initial seed.

the samples which show significant yielding all relax to a very similar steady state stress, while those at lower amplitudes have a clearly different steady state stress. Examination of Fig. 4.5b, shows that in each case, the drop in Σ_{RMS} is associated with a simultaneous sudden increase in the degree of banding, indicating that the yielding is closely related to a growth in heterogeneity. Note that the final degree of banding for $1.5 \leq \gamma_0 \leq 2.75$ is approximately the same, while for $\gamma_0 = 1.25$ it is two orders of magnitude lower, and doesn't appear on the scale for $\gamma_0 = 1$. This implies that the small stress drop we see for $\gamma_0 = 1.25$ is caused by a qualitatively different process to the yielding we see at higher amplitudes, and is not driven or accompanied by a shear banding instability of any experimentally observable amplitude. We revisit this phenomenon below when we consider the system under homogeneous shear.

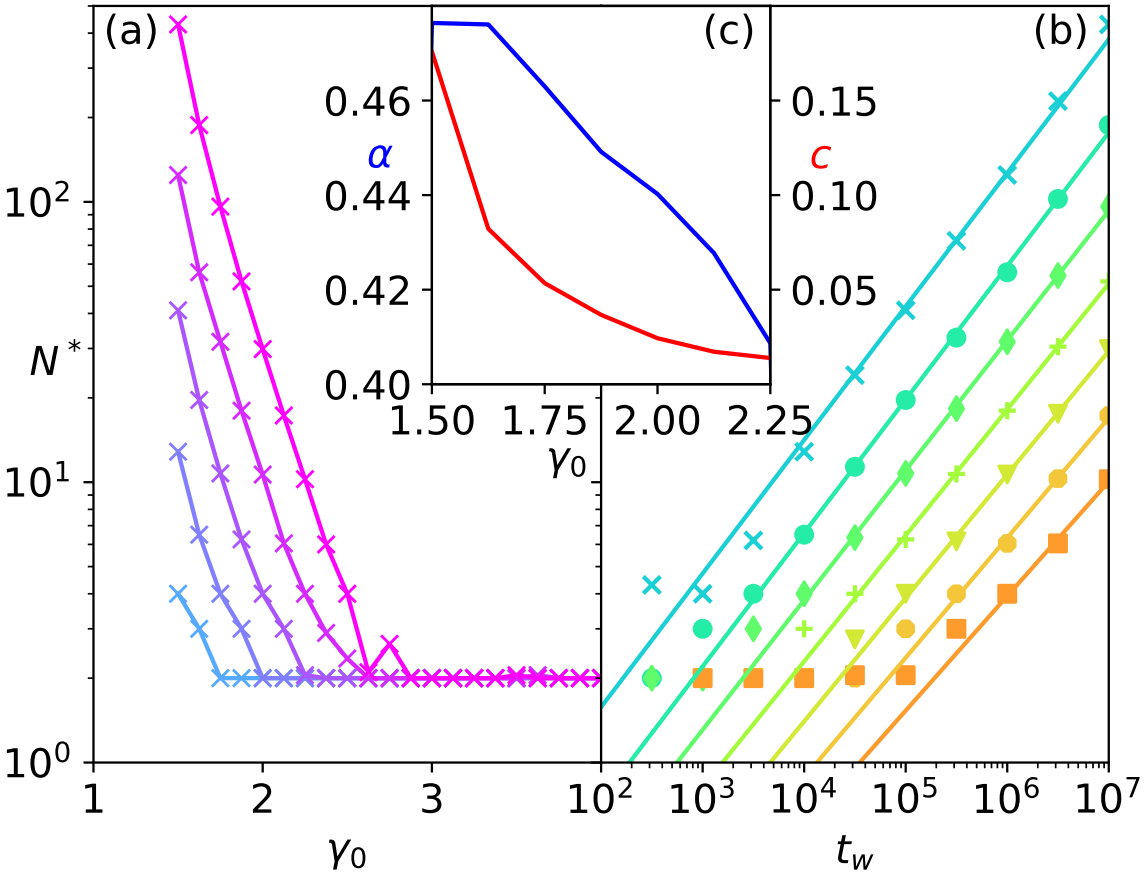

Figure 4.6: **a)** Cycle number at yielding, N^*, as a function of amplitude, γ_0, for $t_w = 10^3, 10^4, ..., 10^7$ in curves bottom to top, blue to pink. **b)** Cycle number at yielding, N^*, as a function of waiting time, t_w, for amplitudes $\gamma_0 = 1.5, 1.675, 1.75, ..., 2.25$ in data sets top to bottom, blue to red. Marked symbols show data points, and straight lines show power law best fits, $N^* = ct_w^\alpha$. **c)** Power law exponent, α, and prefactor, c, as a function of amplitude, γ_0. Only cases with $\Sigma_D > 0.1$ are shown.

The right of Fig. 4.5 shows both Σ_{RMS} and $\langle\dot{\gamma}\rangle$ as a function of cycle number, N, for various t_w and $\gamma_0 = 1.5$. Here, it can be seen that all the samples show some level of delayed yielding, although for the smallest t_w, these yielding events follow a rise in the stress. In the general, the cycle in which the sample fails, N^*, increases as t_w increases. We now see that the steady state stress of all the samples is equal, which is to be expected at constant amplitude, as t_w is an initial condition of which the system should retain no memory in steady state.

To explore these trends further, Fig. 4.6 shows N^* as a function of both γ_0 and t_w, now excluding samples with $\Sigma_D < 0.1$. Fig. 4.6a shows that at high amplitude, $N^* \to 2$ for all t_w, indicating a yielding process which starts within the first cycle.

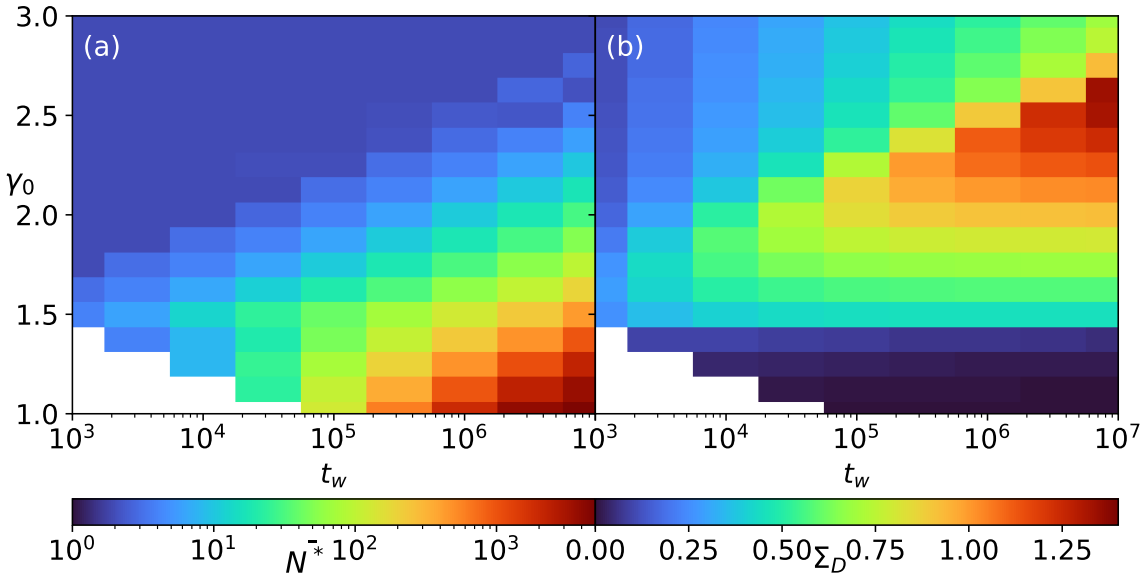

Figure 4.7: **a)** Colourmap showing cycle number at yielding, N^*, as a function of both t_w and γ_0. **b)** Colourmap showing size of the stress drop, Σ_D, as a function of both t_w and γ_0. In both plots, the region in white is where the maximum of Σ_{RMS} occurs after its minimum, and so no yielding is considered to have taken place.

Above a critical amplitude, $\gamma_0 > \gamma_c$, with $\gamma_c \approx 1.4$, we see N^* increase as amplitude decreases. For $\gamma_0 < \gamma_c$, we then see very small stress drops, and the corresponding N^* are not marked here. Fig. 4.6b shows the corresponding plot with N^* as a function of t_w, and we now see that for any amplitude there is a region in which $N^* \approx 2$, but outside that region, N^* appears to show a power law dependence on t_w. This power law implies that if we were to keep increasing t_w outside of the limits shown, we would also see N^* increase without bound. Fig. 4.5c shows the exponent and prefactor of the power law as a function of amplitude, and we see the prefactor clearly growing as the amplitude decreases, in support of the trend seen in Fig. 4.5a. The exponent of the power law varies smoothly, although shows a very weak dependence on amplitude. The smooth dependence of both of these parameters suggests that for a given t_w and γ_0, we could use the power law to predict N^*.

Having examined N^* as a function of γ_0 and t_w separately, we turn now to Fig. 4.7a, which shows N^* in the full 2D parameter space of γ_0 and t_w. We see that for all t_w there is an amplitude below which no yielding occurs, either because the stress maximum occurs after the minimum or because the size of the stress drop is small.

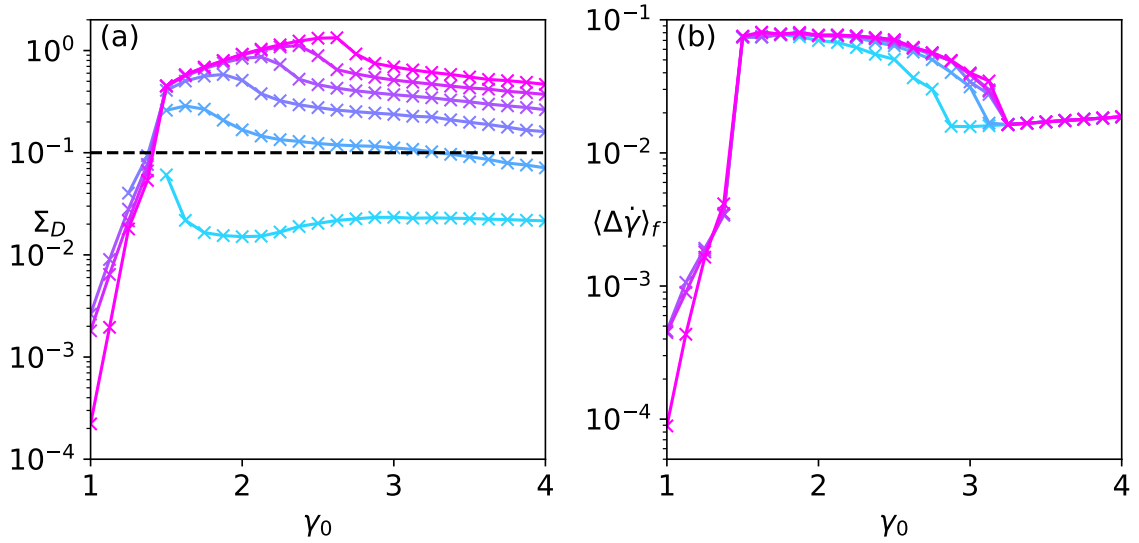

Figure 4.8: Normalised stress drop, Σ_D, (left) and final degree of banding, $\langle\dot{\gamma}\rangle_f$, (right) as a function of amplitude for $t_w = 10^3, 10^4, ..., 10^7$ in curves from blue to pink. Both show a clear change in behaviour around a critical amplitude, $\gamma_c \approx 1.4$. The black dashed line in panel (a) shows $\Sigma_D = 0.1$, and samples below this line are excluded from Fig. 4.6.

Everywhere else, N^* increases with decreasing amplitude and increasing t_w, as seen before. The trends shown imply that it would be possible to see delayed yielding for an arbitrarily large amplitude, provided t_w is taken large enough. The bottom right corner of the plot shows that N^* does continue to increase for $\gamma_0 < \gamma_c$, and it grows very quickly as amplitude decreases. However, what we see in this regime is not really yielding, as the magnitude of the stress drop is small compared to the steady state stress.

Fig. 4.7b shows the stress drop, Σ_D, as a function of both γ_0 and t_w, and we now see two different types of behaviour. For $\gamma_0 \geq 1.5$, there is a clear trend in Σ_D, and it is typically greater than 0.2. For $\gamma_0 < 1.5$, a very different trend emerges, which barely depends on t_w within the region in which yielding occurs. Σ_D is also much smaller, and typically around 0.1. This is also the only region in which there are samples which show no yielding.

To further explore the region of Fig. 4.7b which looks visibly different ($\gamma_0 < 1.5$), we turn to Fig. 4.8, which shows the normalised stress drop, Σ_D, and the final degree of banding, $\langle\dot{\gamma}\rangle_f$, as a function of amplitude for various t_w. We see that as

the imposed strain amplitude is decreased towards γ_c, the final degree of banding reaches a clear plateau, and then for amplitudes only very slightly smaller than γ_c, the final degree of banding is significantly smaller. Fig. 4.8a shows more clearly the transitional behaviour that we noted from observation of the size of the stress drop in Fig. 4.7b, and shows that this transition occurs at exactly the same amplitude as the transition in the final degree of banding.

For this reason, we separate the samples which yield into two categories: for $\Sigma_D > 0.1$, which typically corresponds to $\gamma_0 > \gamma_c$, we consider the sample to have shown significant, measurable yielding. For $\Sigma_D < 0.1$, we consider the sample to not show significant yielding, despite the small stress drop (which can still be exceptionally delayed). This threshold is marked on Fig. 4.8a, which reveals that it does exclude all samples which do not show significant banding. However, it also excludes some samples with $\gamma_0 > \gamma_c$, and applying a threshold based on $\langle\dot{\gamma}\rangle_f$ may appear to be more appropriate. We chose a criterion based on stress despite the fact that it doesn't provide a perfect distinction between the two qualitatively different regimes because in a real application, a significant change in stress would be necessary to consider a sample to have yielded, and not simply a growth in internal heterogeneity. Additionally, it is significantly easier to measure a change in the stress than in the degree of banding in a laboratory setting. Based on this distinction, samples with $\Sigma_D < 0.1$ are excluded from Fig. 4.6.

Homogeneous Shear

So far, we have presented results only for heterogeneous shear. We now also present results for samples with enforced homogeneity, in which the strain rate of each streamline is always set to the applied strain rate, thereby excluding the possibility of shear banding. Note that this is not experimentally possible, and we explore this only to provide further theoretical insight. Fig. 4.9 shows the stress curves from Fig. 4.5 alongside their counterparts, in which strain rate homogeneity is enforced. Examination of the top two panels, at constant t_w, reveals that several samples

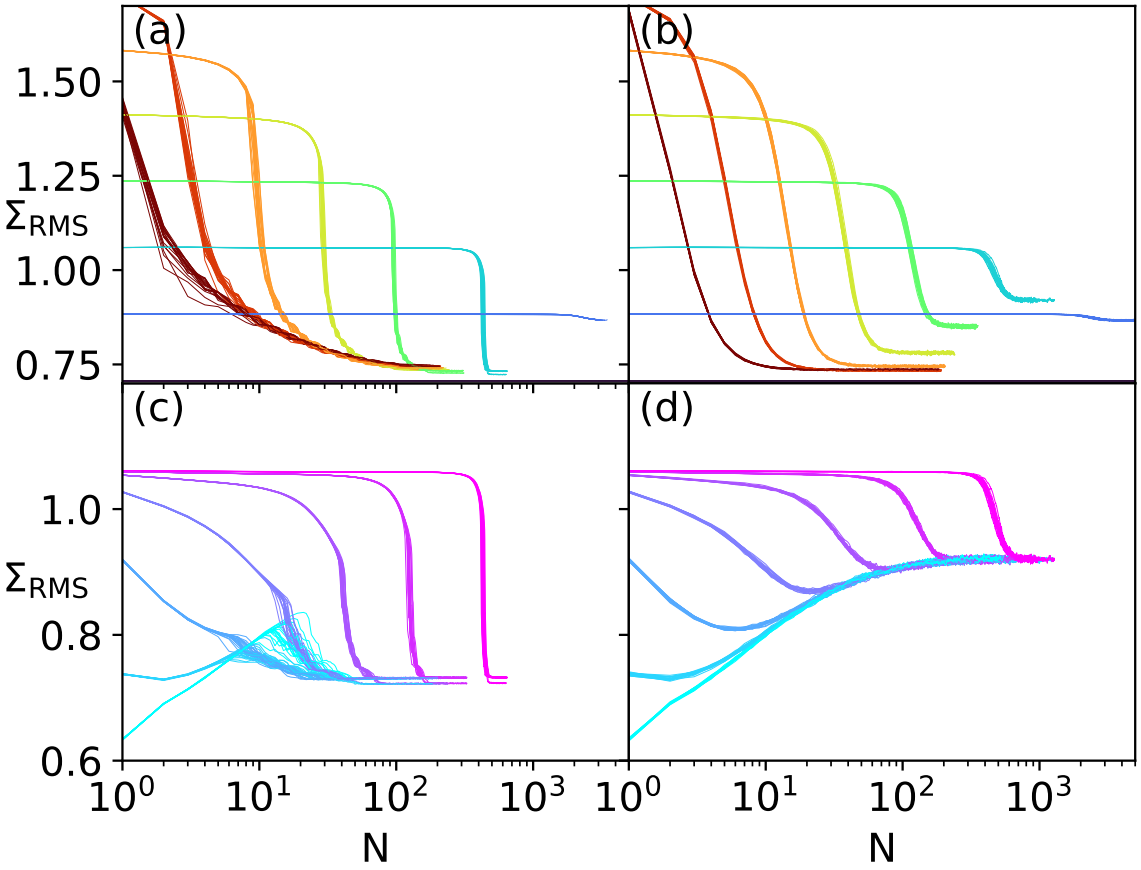

Figure 4.9: Root-mean-square stress, Σ_{RMS} as a function of cycle number N for heterogeneous shear (left) and homogeneous shear (right). Top: waiting time $t_w = 10^7$ and strain amplitudes $\gamma_0 = 1, 1.25, ..., 2.75$ in curve sets right to left, blue to red. Bottom: strain amplitude $\gamma_0 = 1.5$ with waiting time $t_w = 10^1, 10^2, ..., 10^7$ in curve sets left to right, blue to pink. Within each set, each curve corresponds to a different random initial seed.

now have different steady state stress values, while those at low and high amplitude have essentially the same steady state values under homogeneous shear as under heterogeneous shear. This can be understood as follows: at high amplitude, the samples fluidise rapidly, and this effect is strong enough to occur without shear bands developing. At low amplitude, the heterogeneous steady state still has a very low degree of banding, and this is unaffected by enforcing homogeneous shear. These samples do not appear to fluidise substantially, and so it seems the amplitude is too low to properly fluidise the homogeneous state or to generate significant shear banding. For intermediate amplitudes, the system fluidises significantly in both cases, but under heterogeneous shear, the formation of shear bands allows the system to fluidise further and reach a new steady state. This implies that the homogeneous

steady states for $1.5 \leq \gamma_0 \leq 2$ are unstable to growth of heterogeneity. We also see from these panels that almost every sample yields more slowly under homogeneous shear. We suggest, therefore, that the sudden growth of a shear band is able to fluidise the sample much more rapidly. The samples that do not show this difference are for strain amplitude $\gamma_0 < 1.5$, for which the stress curves are effectively identical between the two plots.

Fig. 4.9c-d show stress curves at a given imposed strain amplitude, $\gamma_0 = 1.5$, for different values of the waiting time, t_w, and we find that in both cases the steady state is independent of t_w. However, once again, we find two different steady states, implying that the homogeneous steady state is unstable to growth of heterogeneity. Many of these curves show stress drops of significantly smaller amplitude under homogeneous shear than under heterogeneous shear, and in some cases the stress increases as it approaches steady state rather than decreasing. Once again, we also see significantly slower yielding as a function of cycle number in homogeneous shear compared to when shear banding is allowed.

These graphs provide further evidence for a critical amplitude at $\gamma_c \approx 1.4$: it is now clear that for all parameters, there is a homogeneous yielding mechanism possible. For some parameters, there is also a heterogeneous yielding mechanism available, which happens faster and takes the samples to a steady state of lower stress than in the homogeneous case. For $\gamma_0 < 1.5$, the samples for which heterogeneous shear is allowed still yield in exactly the same way as those for which homogeneity is enforced, while those at higher amplitudes display clear differences between homogeneous and heterogeneous shear. There is therefore a qualitative difference between the yielding process which occurs for $\gamma_0 < \gamma_c$ and the process for $\gamma_0 > \gamma_c$

4.5 Discussion

We have uncovered two distinct forms of yielding within the SGR model subject to LAOS. One of these is related to a shear banding instability and is inherently

heterogeneous in nature. In contrast, the sample remains homogeneous in the other case. The heterogeneous yielding generally happens more quickly, and most of the stress change typically occurs over just a few cycles. In contrast, homogeneous yielding can take tens of cycles to occur.

When heterogeneous shear is allowed, we find that there is a critical strain amplitude, γ_c, below which samples nonetheless remain homogeneous during yielding, while for larger amplitudes shear bands form during yielding. This same critical amplitude also delineates two separate regimes, which are qualitatively distinctive even when analysing only the stress as a function of number of cycles: for $\gamma_0 < \gamma_c$, the stress drop as the sample yields is small compared to the steady state stress, and tends to zero as the oscillation amplitude is decreased, while for $\gamma_0 > \gamma_c$, the stress drop is significant, except at very low t_w.

We therefore were able to define a critical amplitude, $\gamma_c \approx 1.4$, below which the samples do not show significant yielding under oscillatory shear. This is very close to the LAOS threshold which we motivated in Eq. 4.14, which suggests that perhaps $\gamma_c \simeq \sqrt{2}$. The fact that new behaviour emerges as the oscillation amplitude is increased above this limit suggests that the heterogeneous yielding we observe at larger amplitudes is a non-linear effect, and is closely related to the fact that during each cycle, the elastic energy of each element is normally increased above the typical yield energy. However, note that this estimate was based on the *typical yield energy after local yielding*, while in practice, for high t_w the typical local yield energies are generally higher than this.

This helps us explain the yielding behaviour as a function of t_w: for an individual element that has not yet yielded, $l = \gamma_0 \sin(\omega t)$, and so the yielding rate is given by

$$\Gamma(t; E) = \Gamma_0 \min\left\{\exp\left[-\frac{E - \frac{G}{2}\gamma_0^2 \sin^2(\omega t)}{x}\right], 1\right\}. \tag{4.16}$$

We now assume that the element has $\frac{1}{2}Gl^2 < E$, so that the maximisation term is not needed, and the probability that the element has not yielded at a point in time,

$P_N(t;E)$, then obeys

$$\frac{dP_N(t;E)}{dt} = -\Gamma(t;E)\,P_N(t;E)\,, \tag{4.17}$$

so that the probability of that element yielding in each cycle is given by

$$\begin{aligned} P_Y(\gamma_0,E) =& 1-\exp\left(-\Gamma_0\int_0^{2\pi/\omega}\exp\left[\frac{\frac{1}{2}G\gamma_0^2\sin^2(\omega t)-E}{x}\right]dt\right) \\ \approx& \Gamma_0\int_0^{2\pi/\omega}\exp\left[\frac{\frac{1}{2}G\gamma_0^2\sin^2(\omega t)-E}{x}\right]dt, \end{aligned} \tag{4.18}$$

where the approximation requires that the probability of yielding in each cycle is small, which corresponds to the situation in which N^* is large. The expected number of cycles before the element yields, $\mathcal{E}(N^*)$, is inversely proportional to this probability [156], so

$$\mathcal{E}(N^*) \propto \frac{1}{\Gamma_0}\exp\left(\frac{E}{x}\right)\frac{1}{\int_0^{2\pi/\omega}\exp\left[\frac{\frac{1}{2}G\gamma_0^2\sin^2(\omega t)}{x}\right]dt}. \tag{4.19}$$

The functional dependence of this value on γ_0 is non-trivial, but if we assume that after ageing $\bar{E} \propto \log(t_w)$, as in [145], the power law behaviour as a function of t_w emerges naturally. If $\gamma_0 > \gamma_c$, once the element has yielded, it then has a high probability to yield each cycle, and this probability stays high, so the element exhibits consistent plastic-like behaviour. Note that while we can predict a power law dependence on t_w, predicting the exponent would require considering the full variation of E across elements, which is non-uniform. There will always be a small number of elements with much lower E than the sample average, which are likely to yield earlier, but a much larger number close to the mean value, and the greater number increases the probability that one of the these will yield first. Calculating the power law exponent analytically would require an additional integral over this distribution, which we do not attempt here.

To understand the behaviour as a function of amplitude, we consider the dynamics only qualitatively. As amplitude decreases, so do the typical values of l^2 over each cycle, and so the probability of an element yielding during that cycle decreases,

meaning that more cycles are required for yielding, so N^* is a decreasing function of amplitude. However, for $\gamma_0 < \gamma_c$, even after it yields for the first time, the element has a low probability of yielding in each cycle, and that probability decreases with amplitude. For $\gamma_0 < \gamma_c$, the element therefore still displays mostly solid-like behaviour after yielding, and so the change in its average stress with respect to cycles before it yielded is small. This potentially explains both the general trends we see as a function of γ_0 and t_w, and the qualitative change in behaviour at $\gamma_0 = \gamma_c$.

The above discussion considered the behaviour of individual elastoplastic elements, and while the behaviour of the sample will broadly follow the average behaviour of an individual element, it is important to consider heterogeneous effects. Based on the considerations above, the number of cycles before the first yielding is likely to show significant variation across elements, which will lead the sample to yield slowly over many cycles. This is indeed what we see under homogeneous shear. In heterogeneous shear, in contrast, we see very rapid yielding over only a few cycles. To understand this, we consider the heterogeneous dynamics of the system.

Consider a single streamline under heterogeneous shear, with $\gamma_0 > \gamma_c$. When a single element on this streamline yields, it will decrease the root mean square elastoplastic stress on that streamline over future cycles, as discussed above. To maintain force balance, this causes an increase to the local strain rate of that streamline, so that the streamline which has had the most elements yield at least once is now being sheared at a faster strain rate than the global applied strain rate. The elements on that streamline will therefore be pushed to larger l^2 in each cycle, making them more likely to yield, and as each element yields the local strain rate will be increased further. This therefore becomes a positive feedback cycle, causing a single streamline to very rapidly yield completely. The diffusivity in the model means that as a single streamline yields rapidly, the adjacent streamlines will also be impacted, and this is likely to trigger a similar avalanche in each of them, so that the plastic behaviour then diffuses across the sample from the first streamline to fully yield. This feedback and avalanche behaviour is what causes the much more

rapid yielding which is seen under heterogeneous shear.

One result of this phenomenon is that as the sample yields, the streamlines which are displaying solid-like behaviour are pushed to lower strain rates, making them less likely to yield. Under heterogeneous shear, it is therefore possible for some streamlines to stay in their solid-like state for a very large number of cycles without showing significant yielding, while others yield and remain in plastic-like states. We see this when examining the degree of banding across the sample, which remains high indefinitely in samples which have yielded heterogeneously. Simulations of the SGR model with shear startup [35, 145] have shown very long lived shear bands that persist after yielding, but are nevertheless transient and therefore decay after a sufficiently long time period due to diffusion. We might therefore expect that given sufficient time, we would also see the whole sample fluidise under LAOS, and the shear bands heal to leave homogeneous shear finally. On the other hand, the effect of shear banding with a LAOS protocol is to decrease the strain amplitude of the unyielded streamlines, and if this amplitude is decreased below γ_c, there may be no mechanism for those streamlines to yield. The simulations presented here only explore the dynamics for a reasonably short time period after the yielding event, which is typically of the same order of magnitude as the time before yielding, and it therefore remains an open question as to whether or not this banded state will persist indefinitely.

This positive feedback process, in which changes to local strain rate drives faster yielding, leads us to expect that there may be changes to the phase of individual streamlines as they yield, and this is what we see in Fig. 4.10. As a streamline starts to yield, the total strain applied to that streamline falls out of phase with that of the sample average and with the streamlines that are not yielding, and stays out of phase for a significant period of time. The strain rate also falls out of phase with the sample average as this happens, driven by the fact that the unyielded streamlines are in solid-like states, with stress proportional to strain and elements generally unlikely to yield, while the streamline that has yielded is in a plastic-like state, with

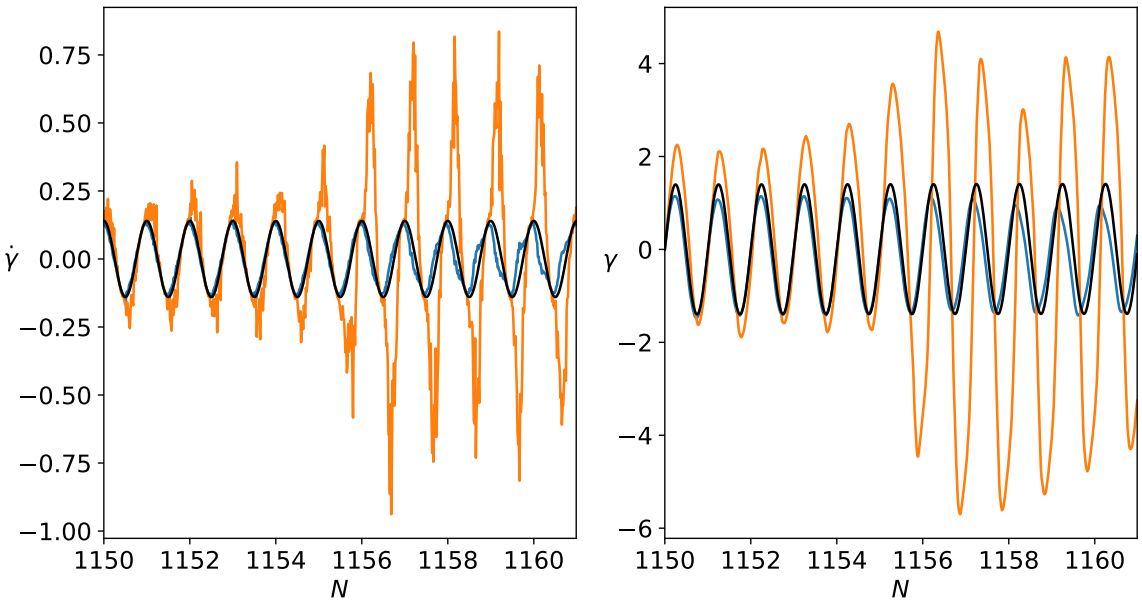

Figure 4.10: Strain rate (left) and strain (right) as a function of cycle number for the sample average (black), a streamline which yields within the window shown (orange) and a streamline which does not yield in the window shown (blue). For the sample shown, $N^* = 1157$. We see that as the orange streamline yields, it falls out of phase with the other streamlines.

stress related to strain rate and with elements frequently yielding. We therefore expect that while this situation continues, force balance will drive a phase difference between the streamlines in different states.

By considering the system dynamics, we have now been able to understand the majority of the observed behaviour. We have motivated the functional dependence of N^* on t_w and γ_0, and the difference in behaviour when $\gamma_0 < \gamma_c$, whilst proposing that $\gamma_c \simeq \sqrt{2}$. We have also been able to understand the differences between heterogeneous and homogeneous yielding, and in particular the reason for the much more rapid yielding generally seen in heterogeneous shear.

4.6 Conclusion

We have seen that for a significant range of values of the strain amplitude, γ_0, and ageing time prior to shear, t_w, the SGR model shows yielding under LAOS, and this yielding can be extremely delayed for large t_w and for small $\gamma_0 \gtrsim \gamma_c$. We have also

seen that the number of cycles until yielding, N^*, follows a power law in t_w. This power law suggests that as t_w increases, the number of cycles until failure increases without bound, such that exceptionally delayed yielding is possible at high t_w.

We have also characterised the dependence of N^* on the oscillation amplitude, γ_0, and found that for $\gamma_0 > \gamma_c$, with critical amplitude $\gamma_c \approx 1.4$, N^* increases as γ_0 decreases. This means that for larger amplitude oscillation, we see less delayed yielding, and at the highest amplitudes yielding is almost instant, while for amplitudes close to the critical amplitude, it means that we see very delayed yielding.

We have also seen that for $\gamma_0 < \gamma_c$, we do see a very delayed stress drop, but the type of yielding is qualitatively distinct, and as a result the associated stress drop becomes small enough that it would be difficult to measure experimentally, so that in general, we would not consider these samples to have yielded. This is in agreement with [51, 65] both of which showed a solid-fluid transition emerge as the amplitude is increased above some critical value.

We have also examined the differences between yielding when homogeneous shear is enforced and when heterogeneous shear is allowed, and find that the yielding generally happens much more rapidly under heterogeneous shear, and typically takes only a few cycles, while under homogeneous shear it can occur over tens of cycles. The much faster yielding under heterogeneous shear is driven by the development of shear bands within the sample, which are associated with local phase changes to the strain and strain rate in regions of the sample which are yielding rapidly. We have also been able to understand these phenomena by considering the dynamics of the SGR model, and the explanations for some of these behaviours led to the conclusion that $\gamma_c \simeq \sqrt{2}$.

We have therefore succeeded in our initial aim of understanding both the cycle number at yielding and the mechanism by which the samples yield. However, all of our results are at fixed temperature and frequency, and some interesting further work would be to explore the dependence of N^* on these parameters as well. Additional interesting further work would be to investigate the persistence of shear bands for a

large number of cycles after yielding, and the extent to which the entire sample is able to fluidise. Such an investigation would be able to draw parallels with previous work on long-lived transient shear bands in the SGR model [35] and would help discern whether or not the shear bands we observe after yielding will persist indefinitely.

It would also be interesting to compare these results to further experimental work, ideally carried out with materials that show rheological ageing. In comparing this work to experimental data, it is important to note that the most significant previous experimental work has been stress controlled [63, 64], while the theoretical work presented here was strain controlled, and therefore further theoretical work with a stress controlled protocol would be helpful. This work makes a very clear prediction for the functional dependence of N^* on sample age, which could easily be compared to experimental data, as could our qualitative prediction for its dependence on strain amplitude.

The results presented in this chapter may also have a significant impact in engineering contexts, especially if they are well supported by future experiments. The predictions that we presented above could motivate changes in the manufacturing process for situations in which understanding and predicting fatigue and delayed yielding is important, and also improve system safety by allowing accurate predictions of the timescale over which materials will remain solid-like before they yield.

Chapter 5

Delayed Yielding in an Elastoplastic Model Under Large Amplitude Oscillatory Shear

5.1 Introduction

In Ch. 4, we summarised some recent experimental and theoretical results concerning delayed yielding in a Large Amplitude Oscillatory Shear (LAOS) protocol, when applied to amorphous materials. We then went on to explore this phenomenon in detail theoretically using the Soft Glassy Rheology (SGR) model. In this chapter, we will consider the same phenomenon using a different theoretical model.

The SGR model is commonly used to model amorphous and glassy materials [37, 149–152, 157–161], and has shown significant success in capturing experimentally observed behaviour. However, there are other models which use similar approaches, one of which is the elastoplastic model (EPM) [38, 39, 162–169].

Exploring the same behaviour in two different theoretical models will be an excellent way to corroborate results and increase confidence that they are related to real physical behaviour and not the details of the model assumptions. It will

also allow us to compare the mechanisms for this process in the two models, which should help us to understand the physical mechanism for the processes we explore. For this reason, we will proceed with a very similar investigation in the EPM to the one we carried out using the SGR model, and compare the results.

The two models in question have several similarities: both involve modelling an ensemble of elastoplastic elements, and in each case these elements have a local elastic strain that can be relaxed by yielding events. As a result, there is a range of behaviour that is shared by the two models, including solid-fluid transitions under shear and shear banding instabilities [36, 37, 65, 66, 144, 162–171].

There are also a few differences between the two models, the most notable of which is that in its glass phase, the SGR model exhibits ageing in the absence of shear [149–152], while the EPM does not [170, 171]. Recall that in Ch. 4, the sample age was our primary measure of degree of annealing prior to shear, and so in this chapter we will need to find an alternative measure of annealing.

In Sec. 5.2, we will outline the construction of the EPM and how we will use it to explore delayed yielding in LAOS. In Sec. 5.3, we will then present the results, which show several similarities to the results in the SGR model.

5.2 Model

Like the SGR Model, the EPM is composed of an ensemble of elastoplastic elements, which are small enough that a macroscopic material contains a large number of them, yet large enough that we can meaningfully define a local elastic strain, l. As the system is sheared, l increases at a rate determined by the local strain rate, $\dot{l} = \dot{\gamma}$. Corresponding to the local strain is a stress Gl and elastic energy $\frac{1}{2}Gl^2$. However, unlike in the SGR model, the local yield energy is always set to a constant, E, and we will work in units in which $G = 1$ and set $E = 1$, which corresponds to choosing the yield strain amplitude.

Each element stochastically hops out of its energy well at a rate Γ, which is determined by the difference between the accumulated elastic strain energy and the local yield energy. This hopping rate is given by

$$\Gamma(l) = \Gamma_0 \min\left\{\exp\left[-\frac{E - \frac{G}{2}l^2}{T}\right], 1\right\}, \tag{5.1}$$

with T the system temperature and Γ_0 the microscopic yielding rate. We work in units in which $\Gamma_0 = 1$. After yielding, the local yield energy remains the same, and the local elastic strain is set to a new value selected from a Gaussian distribution of variance l_W and mean 0,

$$P(l; l_W) = \frac{1}{\sqrt{2l_W\pi}} \exp\left[-\frac{l^2}{2l_W}\right]. \tag{5.2}$$

We set $l_W = 0.05$ throughout. The stress of an ensemble of elements is calculated in the same way as in the SGR model:

$$\sigma = \frac{G}{m} \sum_{i=1,..m} l. \tag{5.3}$$

In the absence of shear, the system evolves towards a steady state in which

$$P(l) = \frac{1}{\sqrt{2T_0\pi}} \exp\left[-\frac{Gl^2}{2T_0}\right], \tag{5.4}$$

with T_0 the system temperature. A lower temperature therefore results in a steady state in which the distribution of l is narrower. This distribution is centred on $l = 0$, and the sample has no macroscopic stress.

To anneal the samples, we will first equilibrate the system at a finite temperature T_0, then instantaneously quench it to a lower working temperature, T, and then immediately begin shearing the system. A lower T_0 therefore corresponds to a better annealed sample, and the system is expected to behave in a more solid-like way for larger strains with lower T_0.

To allow heterogeneous effects and shear banding, we take the same approach as we did in the SGR model: the system is divided into $n = 25$ streamlines arranged in the y-direction, each of which has $m = 10,000$ elastoplastic elements, and the

elastoplastic stress of an individual streamline, σ_i, is calculated using Eq. 5.3. The streamlines are then immersed in a background solvent with a small viscosity, $\eta = 0.05$, and the total stress on each streamline $\Sigma_i = \sigma_i + \eta\dot{\gamma}$. We enforce force balance, $\partial_y \Sigma = 0$, which means that $\Sigma_i = \Sigma_j \ \forall i, j \leq n$, so that the strain rate on any streamline can be calculated using

$$\sigma_j + \eta\dot{\gamma}_j = \frac{1}{n}\sum_j \sigma_j + \eta\dot{\bar{\gamma}}, \tag{5.5}$$

with $\dot{\bar{\gamma}}$ the global applied strain rate. To include stress diffusivity in the system, each time an element yields, we chose three elements at random from each of the neighbouring streamlines and adjust their local strains by $w\Delta l\,[-1, +2, -1]$, where Δl is the magnitude of the change in local strain of the element that yielded during the yielding event and w is a small diffusivity parameter, which we set to $w = 0.05$.

The sample modelled is placed between two flat parallel plates, which are separated in the y-direction by a distance L. We work in units in which $L = 1$. We assume the sample to be translationally invariant and homogeneous in the x- and z-directions, and only allow heterogeneity in the y-direction. We then fix the bottom plate while moving the top plate back and forth in the positive and negative x-directions. This is similar to a Taylor-Couette rheometer geometry, as in previous chapters, and identical to the configuration in Ch. 4.

After quenching the system to a finite working temperature, T, we apply a strain controlled LAOS protocol, with $\dot{\bar{\gamma}} = \gamma_0\omega\cos(\omega t)$. We will consider $\gamma_0 \geq 0.9$, noting that this a lower minimum amplitude than we considered in the SGR model. In this model, an amplitude of $\gamma_0 = \sqrt{\frac{2E}{G}} = \sqrt{2}$, is significant, as it is the amplitude at which elements are likely to yield in every cycle, including the first cycle, regardless of T_0. It is therefore unsurprising that when looking for delayed yielding, we will see more interesting behaviour at slightly lower amplitudes.

As in the SGR model, we also define $\Sigma_{\mathrm{RMS}}(N)$ as the root-mean-square of the stress during the N^{th} cycle, the degree of banding at any point in time, $\Delta\dot{\gamma}(t)$, is the standard deviation of the stress across the sample, and $\langle\dot{\gamma}\rangle(N)$ is the mean of

$\Delta\dot{\gamma}$ during a cycle. We do not seed the system with a perturbation, and instead note that with a finite number of elements on each streamline, there will be some natural variation and stochasticity, and we find that this is sufficient to seed any instabilities.

5.3 Results

We find that, as in the SGR model, some parameter values lead to systems showing yielding after a large number of cycles. This behaviour is shown in Fig. 5.1, which in addition to showing the RMS stress, Σ_{RMS}, also shows the degree of banding as a function of the number of cycles, N, since the inception of shear, revealing that the stress drops are associated with sudden spikes in banding and also that strain heterogeneity slowly accumulates before the system yields. Note that in some cases, the degree of banding appears to drop to very low values, and can oscillate very quickly over several decades; this is in fact an artefact of the averaging process, so for $\langle\dot{\gamma}\rangle < 10^{-7}$, the system is effectively homogeneous and $\langle\dot{\gamma}\rangle$ provides no relevant information.

The left column of Fig. 5.1 shows results for a fixed strain amplitude, $\gamma_0 = 1.15$, and temperature, $T = 10^{-3}$, for various pre-quench temperatures T_0, and reveals that systems with a lower T_0 yield at later times. There appear to be two different steady states with different stresses. The larger of these two stresses is equal to the initial stress of all the systems shown, and is approximately $\gamma_0/\sqrt{2}$, implying that this represents a solid-like state. The alternative steady state, which is reached after a yielding event, instead represents the fluid-like state, and is independent of the initial condition, T_0. We can therefore conclude that the systems for which the stress remains high have not yielded in the time simulated, and remain in their solid-like state. Without simulating for longer, we cannot say for certain whether these systems will ever yield, or whether the higher stress state is a true steady state. We will return to this question below.

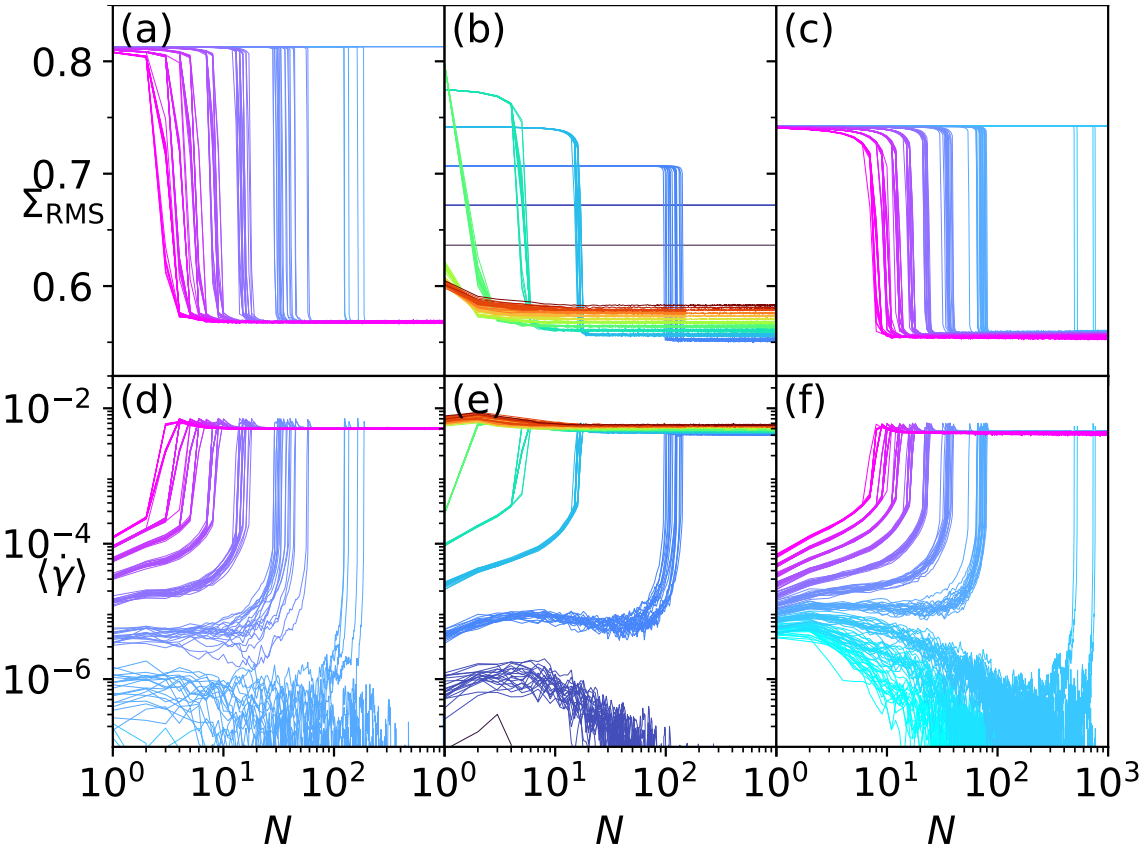

Figure 5.1: Plots of RMS stress, Σ_{RMS}, (top) and mean degree of banidng, $\langle\dot{\gamma}\rangle$, (bottom) as a function of N. Left: $\gamma_0 = 1.15$, $T = 10^{-3}$, $T_0 = 0.001, 0.002, ..., 0.01$ for curves blue to pink. Middle: $T_0 = 10^{-2}$, $T = 7 \times 10^{-3}$, $\gamma_0 = 0.9, 0.95, ..., 1.5$ for curves blue to red. Right: $\gamma_0 = 1.05$, $T_0 = 10^{-2}$, $T_0 = 0.001, 0.002, ..., 0.01$ for curves blue to pink. Curves of the same colour in the same set represent different random seeds.

The middle column of Fig. 5.1 shows systems at fixed $T = 7 \times 10^{-3}, T_0 = 10^{-2}$ and various strain amplitudes. In each run, we again find an initial solid-like state and a final fluid-like state, both of which depend on the strain amplitude. The systems with lower amplitudes do not yield during the time simulated, leaving again the question as to whether or not this is the true steady state. The systems with higher amplitudes yield very quickly, and would not be considered to show delayed yielding. For an intermediate range of amplitudes, we do see a delayed stress drop, and this drop is more delayed at lower amplitude.

The right column of Fig. 5.1 shows systems at fixed $\gamma_0 = 1.05$ and $T_0 = 10^{-2}$ for various T. The behaviour shown is broadly similar to that shown in the left column. We see that the yielding becomes more delayed at lower T, showing a similar trend

to the dependence on T_0, and we still see some systems which do not yield in the time simulated.

To better understand the delay prior to yielding, we now define N^* in the same way as for the SGR model: we identify the cycles at which the stress is at its global maximum and minimum. Provided the minimum is after the maximum, we define N^* as the first cycle for which the stress is less than the midpoint between the maximum and minimum and remains less than the midpoint until the minimum. If the minimum occurs before the maximum, we not consider the system to have yielded and do not define an N^*. To account for the systems that have not yielded during the simulation, but might at some future point, we define the plastic steady state stress, $\Sigma_P(\gamma_0)$, as the lowest steady state value of Σ_{RMS} for any run with a given amplitude. We then consider systems for which $\Sigma_{\text{RMS}} > 1.1\Sigma_P$ in every cycle to have not reached the plastic steady state, and therefore categorize these systems as ones that will either never yield or will yield for some $N > N_{\max}$, with $N_{\max}$ the number of shear cycles that are simulated. We also do not define an N^* for these systems.

We now turn to Fig. 5.2, which shows N^* as a function of various parameters, excluding systems which do not reach their plastic steady state. Panel (a) shows N^* as a function of T_0 for $T = 10^{-3}$ and various amplitudes, with best fit lines to $N^* = A\exp[B/T_0]$. These lines are clearly a good fit to the data. We see that as the initial temperature is decreased, which corresponds to a better annealed initial system, N^* increases, implying later yielding. This follows the same pattern as in the SGR model, in which better annealed systems (with higher t_w) yield later. The plots show no indication of a divergence in N^* at finite T_0, which is supported by the fact that the functional fit has a divergence in N^* as $T_0 \to 0$. Panel (c) shows a very similar plot, now with N^* as a function of T for $T_0 = 10^{-2}$. We see a very similar pattern, and indeed the functional fit that is plotted, $N^* = C\exp[D/T]$, is almost identical to the fit in panel (a).

Panels (b) and (d) of Fig. 5.2 show N^* as a function of amplitude for various

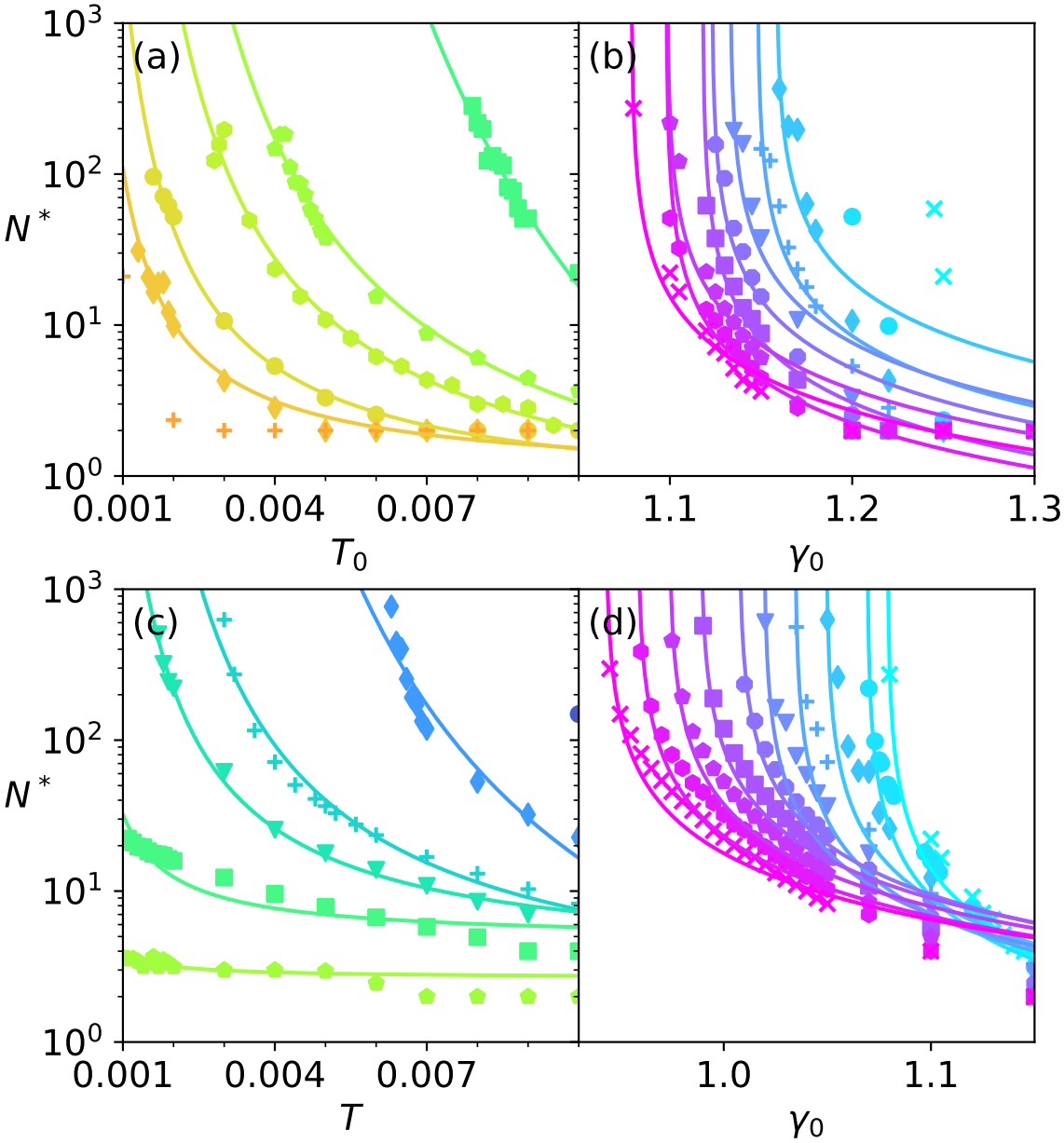

Figure 5.2: a) Yielding cycle, N^*, as a function of initial temperature T_0 for temperature $T = 10^{-3}$ and amplitude $\gamma_0 = 1.1, 1.15, 1.17, 1.2, 1.22, 1.25$ in curves blue to red. Data points are plotted and solid lines show fits to $N^* = Ae^{B/T_0}$. b) N^* as a function of γ_0 for $T = 10^{-3}$ and $T_0 = 0.001, 0.002, ..., 0.01$ in curves blue to pink. Data points are plotted and solid lines show fits to $N^* = \frac{E}{\gamma_0 - \gamma_c}$. c) N^* as a function of T for $T_0 = 10^{-2}$ and $\gamma_0 = 0.95, 1.0, 1.05, 1.07, 1.1, 1.15$ in curves blue to red. Data points are plotted and solid lines show fits to $N^* = Ce^{D/T}$. d) N^* as a function of γ_0 for $T_0 = 10^{-2}$ and $T = 0.001, 0.002, ..., 0.01$ in curves blue to pink. Data points are plotted and solid lines show fits to $N^* = \frac{E}{\gamma_0 - \gamma_c}$.

T and T_0, and we see that N^* increases as the amplitude is decreased, which is again similar to the SGR model. However, we now find that N^* diverges at a finite, temperature-dependent amplitude, and we find that the data provide a good fit to

the function $N^* = E/(\gamma_0 - \gamma_c)$, which is plotted in the solid lines.

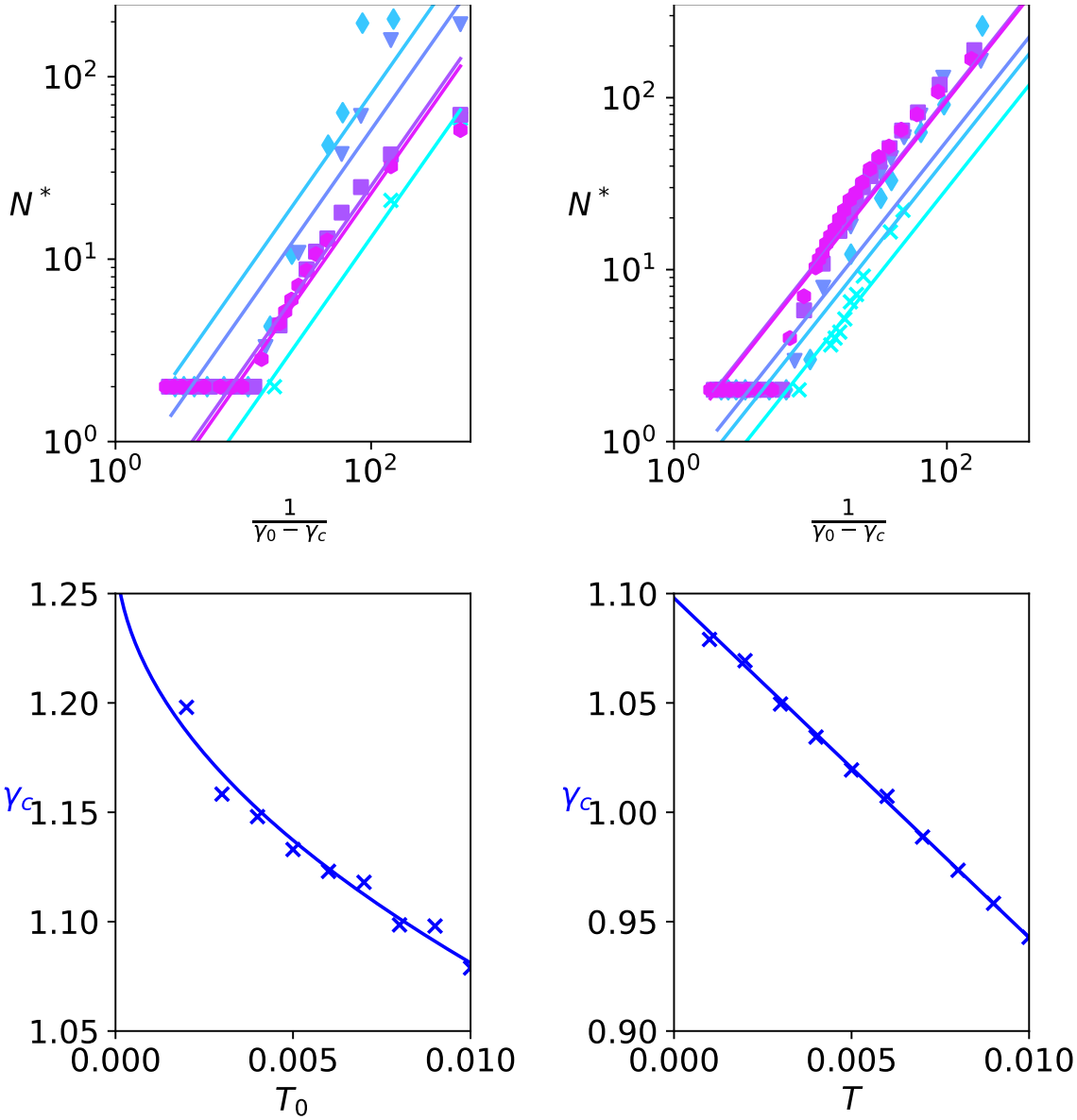

Figure 5.3: Top: yielding cycle, N^*, as a function of $\frac{1}{\gamma_0 - \gamma_c}$, with γ_c a fitting parameter. **a)** $T = 10^{-3}$ and $T_0 = 0.001, 0.002, ..., 0.01$ in curves blue to pink. **b)** $T_0 = 10^{-2}$ and $T = 0.001, 0.002, ..., 0.01$ in curves blue to pink. **c)** Fitting parameter, γ_c, as a function of T_0 at $T = 10^{-3}$. Solid line is best fit to $\gamma_c = A - B\sqrt{T_0}$. **d)** Fitting parameter, γ_c, as a function of T at $T_0 = 10^{-2}$. Solid line is best fit to $\gamma_c = C - DT$.

To examine this further, we turn to Fig. 5.3, which in the top panel shows the same as the right of Fig. 5.2, but rescaled to show a straight line fit. Note that at lower N^* (higher amplitude) the fit breaks down slightly, which is likely because the dependence emerges when N^* is large, as in the SGR model. The bottom panels show γ_c as a function of T and T_0 separately, and we find that the critical amplitude

is linear in T and scales as $\gamma_c = A - B\sqrt{T_0}$.

Having reviewed these graphs, we can now return to the problem of whether or not systems that are in a solid-like state at the end of the simulation would eventually yield, if enough shear cycles were simulated. The systems in the middle columns of Fig. 5.1 that remain in high stress states can be compared to Fig. 5.2b,d and Fig. 5.3, and for these systems we find $\gamma_0 < \gamma_c$, and so we expect them to never yield. The systems in the left and right columns of Fig, 5.2 that remain in high stress states are more puzzling: comparison with the fits in Fig. 5.2a,c suggests that they will yield after some large number of cycles. However, note that γ_c depends on both T and T_0, and inspection of Fig. 5.3c,d reveals that in fact these systems do have $\gamma_0 < \gamma_c$, and therefore we do not expect them to yield. This highlights a subtlety with the fits to T and T_0: although there appears to be no divergence at finite T or T_0, we do expect the trend to break down at some amplitude dependent temperature when $\gamma_c(T_0) > \gamma_0$, and equivalently for T.

We have seen that in the EPM model, many systems show significantly delayed yielding, and the cycle in which they yield, N^* increases as T, T_0 and γ_0 decrease. We have made functional fits of N^* to T, T_0 and γ_0, and find that N^* diverges at a finite critical amplitude, which depends on T and T_0. We have also seen that several systems remain in a solid like state until the end of the simulation, and we predict that these will never yield.

5.3.1 Athermal Limit

To better understand the critical amplitude, we will now examine the athermal limit of the model, when $T = 0$. In this limit, the hopping rate becomes a step function, with $\Gamma = \Gamma_0$ when $|l| > \sqrt{2E}$, and $\Gamma = 0$ otherwise. Recall that before shear begins, the distribution of l takes the form of a Gaussian, with mean 0 and standard deviation $\sqrt{T_0}$. Within each shear cycle, this Gaussian is shifted laterally by a maximum value of γ_0. We define $g = \sqrt{2} - \gamma_0$ which measures the gap between

the centre of the Gaussian at the time of maximum strain and the edge of the energy well. We then assume that, given enough time, every element with $l > 2E$ when strain is at a maximum will yield, and we can then calculate the change in the elastoplastic stress of a streamline from that yielding:

$$\begin{aligned}\sigma_0 =& G\int_g^\infty \frac{1}{\sqrt{2\pi T_0}} e^{-\frac{1}{2}\frac{x^2}{T_0}} \left(x+\sqrt{2}-g\right) dx \\ =& G\left[\sqrt{\frac{T_0}{2\pi}} e^{-\frac{1}{2}\frac{g^2}{T_0}} + \left(\sqrt{2}-g\right)\left(1-\Phi\left(\frac{g}{\sqrt{T_0}}\right)\right)\right],\end{aligned} \tag{5.6}$$

with $\Phi(x) = \frac{1}{\sqrt{2\pi}}\int_{-\infty}^{x} e^{-t^2} dt$. If there are many other streamlines and none of them have elements yielding, the total stress will remain unchanged, and so the maximum strain amplitude of this streamline will change by $\frac{\sigma_0}{\eta\omega}$. This means that in future cycles, the gap between the centre of the Gaussian at maximum strain and the edge of the energy well is $g - g_0$, with $g_0 = \frac{\sigma_0}{\eta\omega}$. Note that this is the maximum change to the amplitude of the streamline, whereas in practice, yielding events on other streamlines are likely to make this lower. There will now be more elements strained past the edge of the energy well, and if we assume that all of these also yield, it will change the total elastoplastic stress by

$$\begin{aligned}\sigma_1 =& G\int_{g-g_0}^{g} \frac{1}{\sqrt{2\pi T_0}} e^{-\frac{1}{2}\frac{x^2}{T_0}} \left(x+\sqrt{2}-g+g_0\right) dx \\ =& G\left[\sqrt{\frac{T_0}{2\pi}}\left(e^{-\frac{1}{2}(g-g_0)^2} - e^{-\frac{1}{2}g^2}\right) + \left(\sqrt{2}-g+g_0\right)\left(\Phi\left(\frac{g}{\sqrt{T_0}}\right) - \Phi\left(\frac{g-g_0}{\sqrt{T_0}}\right)\right)\right].\end{aligned} \tag{5.7}$$

The effect of this will be to push the Gaussian closer to the edge of the energy well, and we can assume that this will continue happening indefinitely, and so we define the elastoplastic stress change after the n^{th} stage as

$$\begin{aligned}\sigma_n =& G\int_{g-g_{n-1}}^{g-g_{n-2}} \frac{1}{\sqrt{2\pi T_0}} e^{-\frac{1}{2}\frac{x^2}{T_0}} \left(x+\sqrt{2}-g+g_{n-1}\right) dx \\ =& G\left[\sqrt{\frac{T_0}{2\pi}}\left(e^{-\frac{1}{2}\left(g-g_{n-1}\right)^2} - e^{-\frac{1}{2}\left(g-g_{n-2}\right)^2}\right)\right. \\ &\left. + \left(\sqrt{2}-g+g_{n-1}\right)\left(\Phi\left(\frac{g-g_{n-2}}{\sqrt{T_0}}\right) - \Phi\left(\frac{g-g_{n-1}}{\sqrt{T_0}}\right)\right)\right],\end{aligned} \tag{5.8}$$

and the associated change in amplitude as

$$\begin{aligned} g_n =& \frac{1}{\eta\omega}\sum_{i=0}^{n}\sigma_i \\ \approx& \frac{G}{\eta\omega}\left[\sqrt{\frac{T_0}{2\pi}}e^{-\frac{1}{2}\left(g-g_{n-1}\right)^2}+\left(\sqrt{2}-g\right)\left(1-\Phi\left(\frac{g-g_{n-1}}{\sqrt{T_0}}\right)\right)\right], \end{aligned} \tag{5.9}$$

where we have neglected terms of the form $g_i\left(\Phi\left(\frac{g-g_{i-1}}{\sqrt{T_0}}\right)-\Phi\left(\frac{g-g_i}{\sqrt{T_0}}\right)\right)$ by assuming that g_i and $g_i - g_{i-1}$ are small and $\frac{g-g_i}{\sqrt{T_0}}$ is large.

The g_i form a series defined by a recurrence relation, which will either converge or diverge. If the series converges, the effect of elements at extreme l yielding is limited, and will perturb the system, but not generate catastrophic yielding. If, on the other hand, the series diverges, enough elements will be able to yield to cause a substantial change to the state of the system. We therefore hypothesise that the conditions for convergence will give a critical amplitude, which we call γ_{co}, below which the system is not able to yield. Note that because of the oscillatory protocol, once elements have yielded, they have a high chance of yielding from a state with an l value of the opposite sign to their first yielding: negative if the first yielding was at positive l. They then have a high chance to yield once more from a state with an l value with the same sign as the first yielding. This reduces the impact on the elastoplastic stress of the streamline that this process generates, and so while $\gamma_0 > \gamma_{co}$ is necessary for yielding, we expect that it will underestimate the critical amplitude. We therefore predict that $\gamma_c > \gamma_{co}$ and there will be some amplitudes for which the g_i diverge, but under LAOS the system is nonetheless unable to yield. Convergence is determined by the sign of $g_n - g_{n-1}$, which we expect to be independent of the prefactor $\frac{G}{\eta\omega}$, and this is indeed what we see following numerical convergence tests.

We are unable to derive an analytic expression for the convergence of g_i, but can test for convergence numerically by calculating successive elements of the sequence. We find that for each T_0, there is a convergence amplitude $\gamma_{co}\left(T_0\right)$, and for amplitudes below this, the sequence converges, while for larger amplitudes it diverges. Fig. 5.4 shows γ_{co} as a function of T_0, and we find that it scales as $\gamma_{co} = \sqrt{2} - B\sqrt{T_0}$, capturing

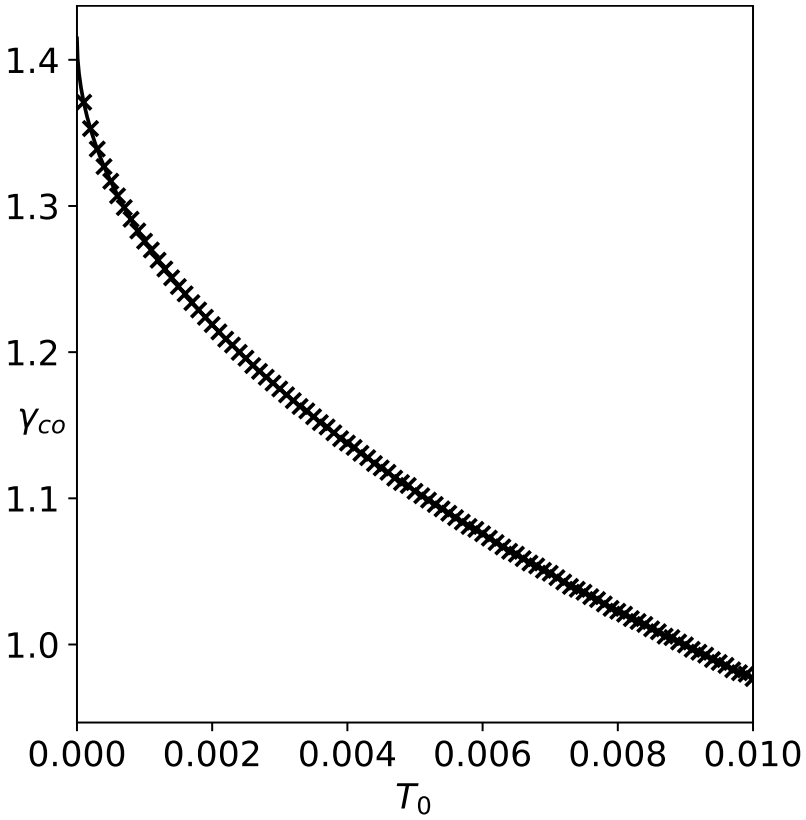

Figure 5.4: Convergence amplitude of Eq. 5.9, γ_{co}, as a function of T_0. Crosses show numerical data points and solid line is best fit to $\gamma_{co} = A - B\sqrt{T_0}$.

the same dependence on T_0 as γ_c. The right most edge of Fig. 5.4 represents the same parameter values as the y-intercept of Fig. 5.3d, and we find that $\gamma_{co} < \gamma_c$ as expected, with $\gamma_{co} \approx 0.9\gamma_c$. The y-intercept of this curve, $\gamma_{co}\,(T_0 = 0)$, is exactly the value we expect, and is the strain at which an element which started with $l = 0$ is sheared out of its energy well. Given that at $T_0 = 0$, $\gamma_{co} = \gamma_c$, and at $T_0 \neq 0$, $\gamma_{co} \approx 0.9\gamma_c$, we therefore suggest that, in the athermal limit, $\gamma_c = \sqrt{2} - \frac{B}{0.9}\sqrt{T_0}$, with B the fitting parameter for γ_{co}.

5.4 Discussion

To understand the phenomena that we have observed, we first consider how the EPM model transitions from a solid-like to a fluid-like state. In the SGR model, the primary measure determining which of these states the material is in was the mean energy well depth. The EPM model, however, has a constant E, and the

distinction is instead based on the distribution of l. If the elements have a very narrow distribution in l at $T = 0$, the material effectively behaves as an elastic solid with a breaking strain: as the system is sheared, the local stress is proportional to the applied strain, until enough strain is applied that some elements have $\frac{1}{2}Gl^2 > E$, at which point there is a sudden plastic relaxation of stress. The same behaviour is broadly observed at low finite T, although there is no strict breaking strain. If, in contrast, the elements have a very broad distribution in l, the rate of plastic relaxation events will be large regardless of the applied strain. The average stress is then controlled by how quickly elements are able to gain local elastic strain after yielding, and so we find that the strain rate is what determines the stress, and the material is in a fluid-like state.

The transition from a solid-like to a fluid-like state is therefore caused by a spreading out of the distribution of elements over l. After annealing, the elements are in a very narrow distribution, and we therefore observe solid-like behaviour. As the system is sheared, individual elements yield stochastically in a way that takes them out of this narrow distribution, and the system transitions towards a fluid-like state.

This helps us to understand the behaviour as a function of temperature: at a higher temperature, there is a higher variation in the yielding rate for elements with $\frac{1}{2}Gl^2 < E$, and so elements are able to more quickly transition into a broad distribution. The origin of the observed behaviour as a function of the initial temperature, T_0, is now also clear: a lower T_0 corresponds to a narrower initial distribution of elements over l, and so it takes longer for this distribution to spread out enough to cause a significant impact on the stress.

To consider the behaviour as a function of amplitude, we note that the delayed yielding is only seen in systems with $\gamma_0 < \sqrt{\frac{2E}{G}}$, which corresponds to the situation in which an element that starts a cycle with $l = 0$ is not sheared past the edge of its energy well. This is because for amplitudes larger than this threshold, most elements have a high chance of yielding each cycle, and this high yielding rate causes the

distribution to spread out much more rapidly. For amplitudes below this threshold, a higher amplitude means that the yielding rate of elements is generally higher, and so the rate at which they leave the initial narrow distribution increases, and it therefore takes less time for the system to transition to a state with a broad distribution of elements in l. This trend continues as γ_0 decreases, until we reach a critical amplitude, at which point not enough elements are able to yield to create a positive feedback loop and cause all the elements to start yielding.

The relation between the yielding event as measured by a stress drop and the growth of a shear band is very similar in the EPM to the SGR model. For a single streamline that has started to transition to a more fluid-like state, its elastoplastic stress will be lower than that of neighbouring streamlines. This causes the strain rate of that streamline to increase, causing it to start yielding faster, and generating a positive feedback loop, leading to a significant variation in strain rate across the system. Once the streamline has fully yielded, its elastoplastic stress cannot decrease further, but it still has a high rate of plastic relaxations, which causes neighbouring streamlines to also start yielding faster. This effect then spreads out across the system, causing a significant fraction of the streamlines to fluidise over a relatively small number of cycles. Once a large fraction of the streamlines have yielded, the unyielded streamlines are pushed to lower amplitudes, and so it may become impossible for them to yield. As in the SGR model, it is therefore unclear whether the heterogeneity that is generated during yielding will eventually completely diffuse, and the system return to a homogeneous state, or whether it will persist indefinitely. We note that while the degree of banding remains high at the end of our simulations, transient shear bands can persist for a considerable length of time [35], and so more shear cycles would need to be simulated to fully answer this question.

By considering the way in which a system yields, we have gained some insight into the behaviour which we observe. We see that the general trends in N^* can all be motivated by considering the dynamics of the model, and in doing so we have been able to consider the situations which we are not able to simulate fully. As a

result, we predict a finite critical amplitude at all temperatures, so that N^* will not continue increasing indefinitely as amplitude decreases. This implies that the systems that did not reach a plastic steady state during our simulation will never yield, no matter how long the simulation is run for.

5.5 Conclusion

We have seen that for a range of parameters, the EPM shows delayed yielding in a very similar way to the SGR model. We have been able to fit the cycle number at yielding to functions of T, T_0 and γ_0, and have explored the general trend of the critical amplitude, γ_c, below which no yielding occurs. We find that significant yielding can occur after a very long delay, even for the parameters explored here, and indeed the divergence of N^* at finite amplitude makes it trivial to propose reasonable parameter values for which the yielding is exceptionally delayed and $N^* > N_T$, with N_T some threshold, which can be arbitrarily large.

One significant difference between the EPM and the SGR model is that in the EPM, we predict that N^* diverges at a finite critical amplitude, and below that threshold there is no yielding. In contrast, recall that in the SGR model we did predict that there would be a yielding event after a number of cycles which increases with decreasing amplitude, but that the magnitude of the stress drop would decrease effectively to zero below a critical amplitude.

For some parameter values, we found that the system remained in a solid-like state for the duration of the simulation and did not show any yielding. After considering the dynamics, we have predicted that these systems would never yield, no matter how long we simulated for. However, this does not mean that those systems have no plastic-like steady state under LAOS, and it may be that reaching a plastic state by shearing at a larger amplitude before reducing the amplitude below the critical amplitude would allow them to reach a plastic steady state. We do, however, predict that under a constant strain amplitude, many systems will never yield.

The fact that the behaviour reported here was observed in two different models suggests that it may be common to many elastoplastic materials. The differences between the results presented in this chapter and the results in Ch. 4 mean that we cannot make detailed, material-invariant predictions, but we can predict that some form of delayed yielding is likely, and that the number of cycles until yielding is a decreasing function of amplitude, within some limits, and is an increasing function of the degree to which the sample is annealed prior to shear.

Some interesting further work would be to more carefully consider and record the distribution of l on each streamline as the system is sheared under this protocol. A detailed understanding of this would likely provide good insight into the yielding process and the trends which were observed. It would also be helpful to consider more fully whether the shear bands that form during yielding will persist indefinitely, or whether they are transient but long-lived. Considering protocols with a varying strain amplitude would be a helpful way to better understand whether or not there are lower stress steady states possible below the critical amplitude, which are simply not accessible in this protocol. Finally, it would be interesting to explore the same phenomenon in a stress controlled protocol to see how similar the behaviour is. This would also provide a more direct connection with a range of interesting existing experimental results [63, 64].

The results presented here may have a significant industrial impact, particularly in combination with the results from the previous chapter, and if supported by experimental work. The characterisation and prediction of the delay before yielding has applications both in manufacturing and in considering the safety of structures. Further, our findings of a finite critical amplitude means that some samples have a very long-lived metastable solid-like state that will nonetheless yield after a large number of cycles, and that that number can be very sensitive to the oscillation amplitude. This high sensitivity could lead to significant uncertainty about a material's response in real world applications where the applied strain amplitude is not precisely controlled. This is potentially significant for range of materials which are already in

use, and for which previous testing showed no yielding on the timescale observed. We hypothesise here that some such materials may still yield at an indeterminate time in the future, particularly if there is even small variation in the strain amplitude, and for this reason we recommend additional caution when materials which behave similarly to this EPM are regularly subjected to a LAOS-like protocol.

Chapter 6

Shape Driven Rigidity Transitions in Epithelial Tissue

6.1 Introduction

Epithelial tissue is a thin layer of tightly packed cells, which lines the outer surfaces of organs and blood vessels in animals. The epithelium generally protects underlying tissue from mechanical, chemical and bacterial hazards [7, 77]. Epithelia can be arranged in a layer a single cell thick (simple epithelium), or in their stratified placement can form layers which are two or more cells deep. In this work, we will only consider simple epithelium, in which we have a 2D plane of cells with a thickness of one cell. Because of their role as protective tissue, epithelial cells need to be capable of changing shape and arrangement in response to external events, such as to fill gaps left by mechanical trauma.

Epithelial cells play a significant role in wound healing [4], and recent work suggests that this may be closely related to a fluidity transition [5] which allows cells to flow past each other and fill in wounds. The experiments in Ref. [5] found that this fluidity transition is closely related to the junctional tension between epithelial cells. Epithelia also play a significant role in embryo development [6, 78], during which

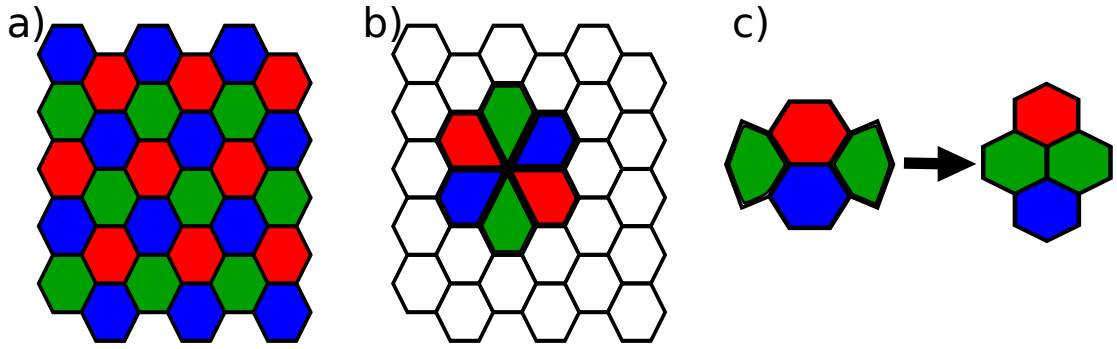

Figure 6.1: Schematic illustration of close-packed polygonal cells. (a) shows a regular hexagonal packing [76]. (b) shows a rosette [76], although note that in normal cellular tissue, the cells forming the rosette would be less regular. (c) shows a T1 transition [75], although these typically happen when the shared edge is much shorter than shown here.

the epithelia rearrange to shape complex tissues as they form and respond to both extrinsic and intrinsic cues to direct cellular morphology. During these processes, the mechanical properties of epithelial tissue and the capability for these mechanical properties to rapidly change are both crucial.

Due to the almost space filling nature of epithelial tissue, individual cells are effectively polygonal in shape, and these polygons must tile in such a way that a 2D plane can be fully covered. The simplest arrangement of this is for each cell to be a regular polygon, such that a collection of these cells is able to tile the plane. The most common such arrangement is a hexagonal packing of cells, as shown in Fig. 6.1a, which is commonly seen in vivo, for example during germband extension in Drosophila embryos [172], as is a semi-regular configuration consisting of pentagons, hexagons and heptagons. Less regular configurations are possible, and in general the cells can be irregular and the arrangement isotropic, and there can be significant variation between cells within a small area of the tissue [76]. During Drosophila gastrulation, cells can form rosettes [76] (see Fig. 6.1b), where more than 4 cells meet at a single vertex, and these cells form quasi-triangular shapes, so that they fit together into an approximate ellipse.

Epithelial cells are also able to locally rearrange themselves through a process known as T1-transitions, which are driven by local forces on cell boundaries [75].

In these processes, a group of neighbouring cells rearrange the interfaces between themselves so that an edge between two specific cells is replaced by an edge between two different cells (see Fig. 6.1c). Because these processes are driven by local forces, they tend to act in a way which relaxes local stresses in the tissue.

Recent experimental work [5,74] suggests that fluidity transitions are an essential part of the epithelial wound healing mechanism. Epithelial tissue was observed to effectively fluidise, allowing individual cells to flow past each other in order to repair the tissue. In addition, a significant number of recent experimental works examining the rheology of epithelial tissue [67–73] and other cell monolayers [173] showed spontaneous transitions between solid-like and fluid-like states, in addition to a range of non-linear rheological responses, including fluidity transitions following deformations, superelasticity and scale-independent stress dispersion and relaxation.

There is a clear motive to generate theoretical models that are able to capture the rich rheological behaviour exhibited by epithelial tissue. Accurately modelling and understanding how and when various phenomena occur has significant potential importance for biomedical applications, which include understanding the growth of tumours and the formation of congenital disorders. One such theoretical approach is the Vertex Model [41, 74, 79–82], in which cells are modelled as individual polygons. Each cell has an area and a perimeter, and the imposition of a free energy allows the calculation of forces on the vertices and/or cell centres. This approach has been successful at capturing several rheological phenomena, including fluidity transitions. In this work we will primarily consider the Vertex Model as used in [41], based on a Voronoi tessellation, which is explained in more detail in Sec. 6.2.

While they capture some interesting biophysics, vertex-based models need to simulate every cell independently, and as a result are computationally expensive, and therefore generally fairly limited in the number of cells they can simulate. It would therefore be advantageous to develop a coarse-grained continuum model capturing the same physics, in which a single grid point might simulate hundreds or thousands of cells. This would allow the simulation of much larger cell areas,

and also make it possible to explore larger scale phenomena, such as shear banding effects. A continuum model for tissue rheology was first proposed in [40], based on a simple trap or soft glassy rheology model. This model predicted a solid fluid transition, and found a structurally significant order parameter in relation to cell shape. This work was built on in [83], in which a mean-field theory was developed, which coupled cell shape and tissue stiffness to cell motility and polarization. The resulting model could be tuned between largely homogeneous states and patterned states, and featured a cell anisotropy parameter as a measure of the rheological properties of the tissue. A similar mean-field continuum model was derived in [84], in which a fluidity transition was also observed as a function of cell elongation. Later, the authors of [174] used a Poisson Bracket formalism to derive equations of motion for coarse-grained fields describing epithelial tissue. However, while these equations were derived, the emergent rheology was not explored in depth.

However, while there have been several attempts at constructing continuum rheological models of epithelial tissue, there are none so far which capture all of the features seen in the Self Propelled Voronoi model presented in [41]. In Sec. 6.2, we will lay out what these features are, and then in this work we will attempt to construct a continuum model which exhibits all of them. This has proven to be a challenging task, and we have so far been unable to construct a single model that captures all these features. Nonetheless, we do present a model, and several variants of it, that improve significantly on previous attempts.

6.2 Self Propelled Voronoi Model

In this section, we summarise the model design and key features of the Self Propelled Voronoi (SPV) Model used in [41], which is a leading approach in individual-cell level modelling of epithelial tissue. This summary is provided as background for the ensuing discussion of continuum models.

6.2.1 Model

The model compromises a 2D layer of cells labelled $i = 1, .., N$, in which the degrees of freedom are the centres of each cell, $\{\mathbf{r_i}\}$. The cellular structure is then determined using a Voronoi tessellation, so that each cell consists of every point which is closer to the centre of that cell than to the centre of any other cell. The result of this is that for any given set of cell centres, the plane is divided into a space filling collection of convex polygons [175], separated by straight edges. To avoid edge effects, Lees-Edward boundary conditions [176] are used, which allows rigorous definitions of cell boundaries which cross the edge of the model space. Once a Voronoi tessellation has been generated for a set of cell centres, the perimeter, P_i, and area, A_i of each cell can be calculated.

The mechanics of the tissue are described by a free energy,

$$E = \sum_{i=1}^{N} \left[K_A \left(A_i - A_0 \right)^2 + K_P \left(P_i - P_0 \right)^2 \right], \tag{6.1}$$

where the sum is over all $i = 1, ..., N$ cells in the packing. A_0 and P_0 are a target cell area and perimeter respectively, and K_A and K_P elastic moduli. The first term generates an energy cost for deviations from the target cell area, and arises from the incompressibility of the cell volume. The second term generates an energy cost for deviations from the target cell perimeter, and is driven by the interfacial tension between cells and the contractility of the cell cortex. The constants K_A, K_P, A_0, P_0 can in principle vary across the tissue (and even in time), but in the work in [41], the tissue was assumed to be homogeneous, and therefore the constants are system parameters, rather than cell parameters, and are furthermore assumed to be time-independent.

These simulations were carried out with a fixed cell number and density, and as a result the average cell area, $\bar{A}$ was constant, and so the authors chose $A_0 = \bar{A}$. Setting the length unit such that $A_0 = 1$, Eq. 6.1 can be non-dimensionalised as

$$E = \sum_{i=1}^{N} \left[\kappa_A \left(a_i - 1 \right)^2 + \left(p_i - p_0 \right)^2 \right], \tag{6.2}$$

with $\kappa_A = k_A\bar{A}/K_P$ the rescaled area elasticity, a_i the non-dimensionalised area, $p_i = P_i/\sqrt{\bar{A}}$ the cell shape index and $p_0 = P_0/\sqrt{\bar{A}}$ the target cell shape index. The shape index, p_i, is a now a single dimensionless quantity which describes the cell shape. For a regular polygon, p_i is a decreasing function of the number of sides, such that for a polygon with n sides, $p_n = 2\sqrt{n\tan(\pi/n)}$, so that $p_\infty \approx 3.54$ (circle), $p_6 \approx 3.72$ (hexagon), $p_5 \approx 3.81$ (pentagon) and $p_4 = 4$ (square). For irregular polygons, the shape index is larger than the shape index for a regular polygon with the same number of sides, and a higher shape index indicates a more elongated polygon. The target cell shape index, p_0, is therefore a crucial parameter, which controls the preferred shape of cells. The force on each cell is then calculated as the spatial derivative of the free energy,

$$\mathbf{F_i} = \partial E/\partial \mathbf{r_i}, \tag{6.3}$$

so that forces act to minimise the free energy when following the dynamical rules prescribed below.

For all the results in Ref. [41], $\kappa_A = 0$, which corresponds to the assumption that cell area fluctuations have a low impact on the tissue dynamics. In practice, their simulations with $\kappa_A = 0$ show only small fluctuations in local cell area, implying that cell area, at least for small numbers of cells as modelled, is controlled primarily by the constraint on $\bar{A}$, without needing a term in the free energy.

The system is sheared according to a quasistatic, simple shear startup protocol. Starting from a strain-free state, the strain is increased in small increments, $\Delta\gamma$ by moving each cell centre according to $\Delta\mathbf{r_i} = \Delta\gamma y_i\hat{\mathbf{x}}$. After each strain step, the free energy is relaxed using the FIRE algorithm [177] by adjusting the locations of the cell centres, until all forces $\mathbf{F_i}$ are vanishingly small. The result is that the system is sheared whilst allowing it to fully relax at each small increment of strain, so that the strain rate is effectively infinitesimal compared to all other timescales in the system.

To calculate the stress response of the system, first we define $\mathbf{l}_{ij}$ as the vector of the junction shared by cells i, j. We can then calculate the tension on that cell edge

from

$$\mathbf{T}_{ij} = \frac{\partial E}{\partial \mathbf{l}_{ij}} = 2\left[(p_i - p_0) + \left(p_j - p_0\right)\right]\hat{\mathbf{l}}_{\mathbf{ij}}. \tag{6.4}$$

The contribution to the stress tensor of a cell edge will be given by the outer product between $\mathbf{T}_{ij}$ and $\mathbf{l}_{ij}$, normalised by the simulation box size, L. The total stress on the tissue is calculated by summing all of these contributions, so that the shear component of stress,

$$\sigma = \sigma_{xy} = \frac{1}{L^2}\sum_{i<j} T_{ij}^x l_{ij}^y. \tag{6.5}$$

We now have a model with one important physical parameter, the target cell shape index, p_0. The model is subjected to quasistatic shear as described above, and at each strain step the stress response is calculated, so that shear-startup stress-strain curves can be plotted.

Note that while this model does not include an explicit mechanism for T1 transitions, they are still present as a mechanism for stress relaxation. However, rather than being generated by a single process, they are a consequence of the Voronoi tessellation, which means that at each strain step, cell edges are redrawn. When combined with the free energy minimisation, this means that cell junctions in which stress can be relaxed through a T1 transition will naturally do so.

6.2.2 Results

The results of [41] and some physical explanations for them are summarised here for comparison to the continuum models we use in Sec. 6.3. We reproduce one full graph from the original paper here, which is sufficient to show the behaviour we will consider.

Critical Strain

For infinitesimal strain, the model shows a linear stress response, with $\Sigma = G_0\left(p_0\right)\gamma$, with G_0 some elastic modulus. For $p_0 < 3.81$, a non-zero G_0 is observed, which

indicates a solid-like stress response. For $p_0 > 3.81$, $G_0 = 0$, and the stress response is therefore fluid-like. We note that 3.81 is the cell shape index for a regular pentagon, and if we assume that the cells are roughly pentagonal, this behaviour can be explained as follows. For $p_0 < 3.81$, the target cell perimeter is less than the minimum possible value (for a pentagon), which is achieved by a regular pentagon. The cells therefore are all close to regular pentagons before shear starts, and the cell edges are all under tension. To deform the system, the cells are all stretched, causing the perimeter to increase more, and the force required to do this scales as

$$F = |\mathbf{F}| = \frac{\partial E}{\partial p} \propto (p - p_0)\,. \tag{6.6}$$

For cell edges which were already under tension, this requires a non-zero force and therefore the elastic modulus is non-zero. For $p_0 > 3.81$, the target cell perimeter is realised by an elongated pentagon, and so at equilibrium the cells all form elongated shapes with this perimeter, and there is no tension on the cell edges. As the system is sheared, the cells can be stretched and rotated, and the force still scales as $(p - p_0)$, except that now $p = p_0$, and so $G = 0$. The transition at $p_0 = 3.81$ therefore implies that at zero strain, the cells are roughly pentagonal, and occurs at the target shape index which separates states in which the target cell perimeter can be realised by pentagonal cells and the state in which it cannot.

We have seen that for infinitesimal strains, the elastic modulus can be zero or non-zero. When $G_0 = 0$, the initial stress response is $\Sigma = 0$. In fact, this is observed to be true not just for infinitesimal strains, but also for small finite strains. We therefore define the critical strain, $\gamma_c(p_0)$, such that for $\gamma < \gamma_c$, $\Sigma(\gamma, p_0) = 0$. As expected, $\gamma_c(p_0 < 3.81) = 0$, and for $p_0 > 3.81$, we find that γ_c is an increasing function of p_0. This is to be understood as follows: for $p_0 > 3.81$, the unsheared state has elongated cells. When shear begins, the stress in the system is relaxed without changing the shape index of the cells by rotating them. This process continues to occur until the point at which the cells are all aligned in the direction of the flow, at which point they start to be stretched by the continued shear. At this point, the

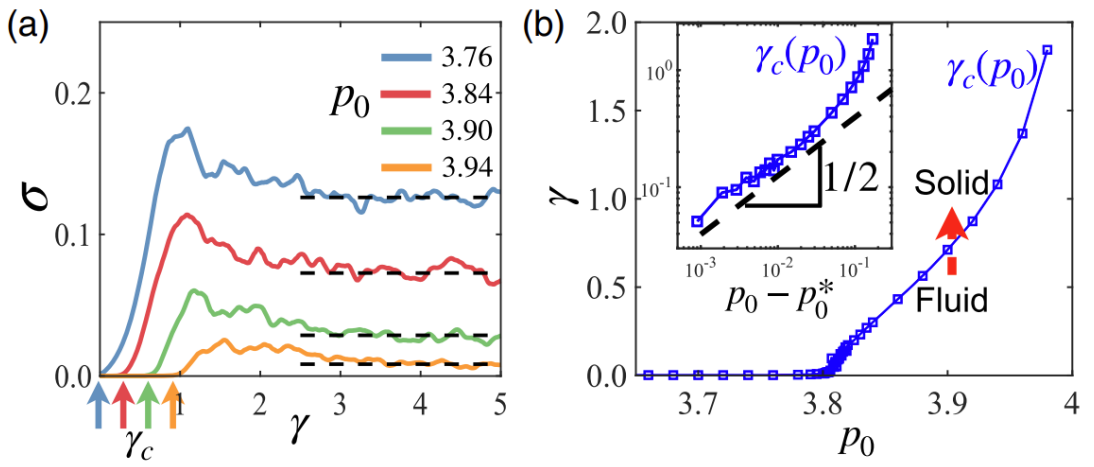

Figure 6.2: (a) Stress vs. strain at different p_0 and $\kappa_A = 0$. An initially fluidlike tissue undergoes strain-driven rigidity above a critical threshold γ_c (location indicated by vertical arrows). (b) The critical strain $\gamma_c(p_0)$ defines a boundary that separates a fluidlike tissue from a solidlike tissue. Inset: γ_c vs p_0 on log-log scale.
Reprinted figure with permission from Junxiang Huang, James O. Cochran, Suzanne M. Fielding, M. Cristina Marchetti, and Dapeng Bi, Phys. Rev. Lett. **128**, 178001, 2022. Copyright (2022) by the American Physical Society [41].

elastic modulus starts to grow, and so a non-zero stress response is observed. The critical strain as function of p_0 is shown in Fig. 6.2b, and Fig. 6.2a shows stress responses for various p_0.

Rigidity Transition

After the critical strain has been attained, we observe a stress response which is an increasing function of strain, until it reaches some maximum, as shown in Fig. 6.2a. After this point, stress typically decreases again until it reaches a steady state value at large strains. Because the simulations are all quasistatic, this steady state stress is exactly the dynamic yield stress of the material, $\Sigma_Y(p_0)$: the minimum stress required for the system to flow in a fluid-like way. It is observed that for $p_0 \gtrsim 4$, $\Sigma_Y \to 0$, and for $p_0 \lesssim 4$, Σ_Y is a decreasing function of p_0. For $p_0 < 4$, the tissue is therefore a yield stress fluid, which, at constant stress, behaves in a solid-like way until the yield stress is reached, after which it yields into a fluid-like state. For $p_0 > 4$, the material is fluid-like, and able to flow continuously for arbitrarily small

stress. For the system to flow continuously at low or zero stress, the stress that is added with each strain step must be relaxed by T1 transitions. The measured dynamic yield stress implies that these transitions are able to happen faster at higher p_0, which is generally associated with more elongated cells.

Strain Hardening

For intermediate strains, $\gamma_c < \gamma < \gamma_m$, with $\gamma_m \sim 1$ the strain at which the maximum stress is observed, stress is an increasing function of strain, and strain stiffening is observed. Rather than having $\Sigma \propto \gamma$, the gradient $d\Sigma/d\gamma$ is seen to increase with time, as shown in Fig. 6.2a. To understand this, recall that in this window, the primary stress response comes from cells being stretched by shear. If we define the elastic modulus as $G(\gamma, p_0) = d\Sigma/d\gamma$, we find that $G \propto dE/dp_0 \propto (p - p_0)$, as seen earlier for $G_0 = G(\gamma = 0)$. However, as the system is being sheared, the cells become more elongated, and so G necessarily increases, generating the strain stiffening observed. The strain stiffening is therefore a direct consequence of the quadratic nature of the $(p - p_0)^2$ term in the free energy.

Stress Overshoot

After the strain stiffening regime, we typically see a stress overshoot in the stress-strain curve. This means that as the strain increases, the stress reaches some maximum value, and then begins to decrease again as the system approaches steady state. The stress maximum at a particular strain rate is generally referred to as the static yield stress, and the presence of a stress overshoot indicates that the static yield stress is greater than the dynamic yield stress. Of particular importance is that these simulations are quasistatic and still show a stress overshoot, meaning that at finite strain rate we would expect to see a non-zero stress overshoot in the limit $\dot{\gamma} \to 0$.

We have now seen several key features of the SPV model, which we hope to also

observe in a continuum model:

1. Solid-fluid transition at $p_0 = 3.81$ for infinitesimal strains
2. A critical strain, $\gamma_c(p_0)$ which must be applied to the system in the fluid state before any stress is measured
3. Strain-hardening at intermediate strains, $\gamma > \gamma_c$ and before the stress overshoot
4. A dynamic yield stress which vanishes at $p_0 = 4$
5. A stress overshoot in the stress-strain curve in the quasistatic limit of $\dot{\gamma} \to 0$

Henceforth, we will refer to these features by their number in this list, as Ft. n.

6.3 Continuum Model

In this section, we aim to derive a continuum model of epithelial rheology, which we will do by considering several variants of a basic model. For each version, we characterise its behaviour and compare it to the key features listed above. All of the versions we consider are at finite strain rate, which is in contrast to the simulations of [41] as just described in Sec. 6.2 above. We use results at $\dot{\gamma} = 10^{-5}$ to approximate the quasistatic limit, and present finite strain rate flow curves of steady state stress as a function of strain rate (see Ch. 2.2.2) to understand the limiting behaviour at infinitesimal strain rate. We will see that some of the model versions work better at higher strain rates, and so also present results at $\dot{\gamma} = 10^{-1}$.

Throughout this section, we use Σ as a shorthand for the shear stress, Σ_{xy}, and set it equal to the elastoplastic stress σ_{xy} without the imposition of a background solvent. The addition of a background solvent would have a negligible effect on the total stress, and as only homogeneous shear is considered, it is not a necessary addition to allow instability to growth of strain heterogeneity. $G = \partial\Sigma/\partial\gamma$ refers to the instantaneous elastic modulus, $\Sigma_f(\dot{\gamma})$ is the steady state stress reached under

shear, $\Sigma_Y = \Sigma_f\left(10^{-5}\right)$ is the steady state stress at low strain rate, which is used as an approximation for the dynamic yield stress, and the critical strain, γ_c, is the earliest strain at which $G > 0.02$. If the maximum stress of a startup curve is less than 0.2 times the maximum stress of any curve at the same strain rate from the same model version, we set $\gamma_c = 0$ and do not plot it. All of these model versions are solved numerically under homogeneous shear startup, in which a fixed finite strain rate is applied instantaneously for all times $t > 0$ (see Ch. 2.2.3). We use the initial conditions for which all the dynamical variables are at stable equilibria in the absence of shear. In situations where the equilibrium state has a variable which is exactly zero, the initial condition used instead sets it to 10^{-10}. This is done because under shear, some model versions have unstable equilibria when a variable is equal to zero.

The derivation of the basic form of the model, presented in Sec. 6.3.1, is credited to Cristina Marchetti, as are the derivations of the adaptations made in Sec. 6.3.4 and Sec. 6.3.5.

Cell Shape Tensor

We first define the variables we will use throughout to describe cellular tissue. The shape of any individual polygonal cell can be described by a rank-2 symmetric tensor, $\hat{\hat{R}}^a_{ij}$, where the superscript ^{a} denotes the a$^{\text{th}}$ cell. While there are several ways to define such a tensor, we will use

$$\hat{\hat{\mathbf{R}}}^a = \frac{1}{n_a}\sum_{\nu\in a}\left(\mathbf{r}^a_\nu - \mathbf{r}_a\right)\otimes\left(\mathbf{r}^a_\nu - \mathbf{r}_a\right), \tag{6.7}$$

where n_a is the number of vertices the cell has, the sum is over the vertices of the cell, $\mathbf{r}^a_\nu$ is the position of the ν-the vertex of the a-th cell, and $\mathbf{r}_a$ is the geometric centre of the cell.

The shape tensor has two eigenvalues, λ^a_1, λ^a_2, and we label them such that $\lambda^a_1 \geq \lambda^a_2$. The eigenvalues are a measure of the cell's extension along its principal axes, and so

for a regular polygon, $\lambda_1 = \lambda_2$. For an irregular polygon, the difference between the eigenvalues gives a measure of cell elongation. We can therefore define a parameter to describe the elongation of the cell,

$$\hat{m} = \frac{\lambda_1 - \lambda_2}{\lambda_1 + \lambda_2}, \tag{6.8}$$

and by definition $0 \leq \hat{m} < 1$. A regular polygon will have $\hat{m} = 0$, and a larger non-zero $\hat{m}$ indicates a more elongated cell.

For a regular polygon, we can calculate the area of the cell from the shape tensor. $\hat{\tilde{R}}^a_{ij}$ will be diagonal with $\lambda^a_1 = \lambda^a_2$, and the sum of the eigenvalues (or the trace of the shape tensor) is exactly the distance from the centre of the cell to each vertex squared. The cell can then be divided into n isosceles triangles, with two sides of length $\sqrt{\lambda^a_1 + \lambda^a_2}$ and one angle of $2\pi/n_a$. The remaining side therefore has a length of $2\sqrt{\lambda^a_1 + \lambda^a_2}\sin(\pi/n_a)$. The perimeter of an n-sided regular cell, then, is

$$P_n = 2n \sin\left(\frac{\pi}{n}\right)\sqrt{\mathrm{Tr}\left[\hat{\tilde{R}}^a\right]}. \tag{6.9}$$

To calculate the area of the cell, we could use the relationships already derived, but we instead attempt to derive an expression based on the other matrix invariant, the determinant. While it is possible to calculate area and perimeter from a single invariant for a cell which is a regular polygon, we wish to generalise these expressions, and so will need expressions involving both invariants. In general, the area should be related to the product of the eigenvalues and the perimeter to their sum, which is indeed what we see for an ellipse. In fact, we are only able to calculate both area and perimeter of a regular polygon from just the trace of the shape tensor *because* there is a one-to-one correspondence between them. We therefore use the fact that for a regular polygon, $2\sqrt{\mathrm{Det}\left[\hat{\tilde{R}}^a\right]}$ is also equal to the distance from the centre of the cell to each vertex squared. Dividing the cell into n isosceles triangles as before, and using this expression to calculate the area of each, we find that the area of a regular n-sided cell is

$$A_n = n \sin\left(\frac{2\pi}{n}\right)\sqrt{\mathrm{Det}\left[\hat{\tilde{R}}^a\right]}. \tag{6.10}$$

These expressions were derived for regular polygons, but we will make the assumption that they are approximately true for polygons that are close to regular. This assumption has been tested by the authors of Ref. [83], who found that for regular polygons whose vertices have been deformed by the application of Gaussian noise up to a noise magnitude of 0.2, these expressions remain an excellent approximation. We now have expressions which allows us to calculate cell area and perimeter provided we know the number of vertices, and these equations can be expressed in terms of the eigenvalues of the shape tensor.

Coarse Graining

So far, we have only considered properties of individual cells, but to construct a continuum model, we will need tissue-scale variables which capture cell level properties. To generate these, we coarse grain the variables we have already constructed, to generate

$$\tilde{\mathbf{R}}\left(\mathbf{r},t\right)=\left[\sum_{a}\hat{\tilde{\mathbf{R}}}^{\mathbf{a}}\delta\left(\mathbf{r}-\mathbf{r}_{\mathbf{a}}\left(\mathbf{t}\right)\right)\right]_{c}, \tag{6.11}$$

$$m\left(\mathbf{r},t\right)=\left[\sum_{a}\hat{m}^{a}A^{a}\delta\left(\mathbf{r}-\mathbf{r}_{a}\left(t\right)\right)\right]_{c}, \tag{6.12}$$

where the sum is over all cells, $\delta\left(\mathbf{x}\right)$ is the 2D Dirac delta function, and $\left[\cdot\right]_{c}$ represents coarse graining. Note that the delta function has units of inverse area, so $\tilde{\mathbf{R}}$ and m are unitless. We now have a tensor and a scalar field which vary smoothly with position and time and describe average properties of the tissue. Note also that $m\geq 0$, and so when we simulate the system, if at any time-step $m<0$, we immediately multiply m by -1, so that m remains positive.

We also define a variable

$$n\left(\mathbf{r},t\right)=\left[\sum_{a}\hat{n}_{\text{eff}}^{a}A^{a}\delta\left(\mathbf{r}-\mathbf{r}_{a}\left(t\right)\right)\right]_{c}, \tag{6.13}$$

which describes the average number of geometric vertices per cell, and is unitless. n_{eff} is the effective vertex number for each cell. Note that there must be an average

of 6 vertices per cell, when vertices are considered to be junctions where three cell boundaries meet, as is typical in vertex modelling. However, with this arrangement, cells can still approximate other polygons, and it is the number of edges that these approximate polygons have which is important when calculating cell area and perimeter from the shape tensor, and which we call n_{eff}. Consider, for example, the face of a standard brick wall. Each brick has 6 vertices according to the definition used in vertex modelling, in which a vertex is a point where three cells are all adjacent to each other. However, each brick is very clearly a quadrilateral in shape, and therefore has 4 geometrical vertices. Robustly defining n_{eff} for a general collection of cells is an open problem which we do not attempt to solve here, but we will allow $n \neq 6$, which corresponds to a situation in which a collection of cells with 6 junctions per cell are behaving as n-gons.

Finally, we separate $\tilde{\mathbf{R}}$ into a traceless matrix and its trace, so that we have

$$R = \text{Tr}\left[\tilde{\mathbf{R}}\right], \tag{6.14}$$

$$R_{ij} = \tilde{R}_{ij} - \delta_{ij}\frac{R}{2}, \tag{6.15}$$

with δ_{xy} the Kronecker delta. Note that our coarse graining operation is linear in all the fields, and so we can also robustly define $\hat{R}^a$ and $\hat{\mathbf{R}}^a$ for each cell.

We now have all the pieces we will need to begin constructing continuum models.

6.3.1 Simple Mean Field Model

We start with the single cell free energy from the Vertex model,

$$E = \kappa_A \left(A_i - A_0\right)^2 + \kappa_P \left(P_i - P_0\right)^2, \tag{6.16}$$

and neglect the first term because for homogeneous tissue with fixed area and cell number, the cell area is constant. To express this in terms of tissue scale properties, we will need to derive an expression for the cell perimeter in terms of $\hat{m}$. For a single

cell, we have

$$A = \mu(n)\sqrt{\lambda_1\lambda_2}, \tag{6.17}$$

$$P = \rho(n)\sqrt{\lambda_1 + \lambda_2}, \tag{6.18}$$

with ρ, μ defined by Eqs. 6.9, 6.10. We will work in units where $A = \mu$, and so $\lambda_1 = 1/\lambda_2$. We therefore have that

$$\hat{m} = \frac{\lambda_1^2 - 1}{\lambda_1^2 + 1}, \tag{6.19}$$

$$\lambda_1 = \sqrt{\frac{1+\hat{m}}{1-\hat{m}}}, \tag{6.20}$$

$$\begin{aligned} P =& \rho\left[\frac{1-\hat{m}}{\sqrt{1-\hat{m}^2}} + \frac{1+\hat{m}}{\sqrt{1-\hat{m}^2}}\right]^{1/2} \\ =& \rho\sqrt{2}\left(1-\hat{m}^2\right)^{-1/4}, \end{aligned} \tag{6.21}$$

$$(P-P_0)^2 = 2\rho^2\left(1-\hat{m}^2\right)^{-1/2} - 2\sqrt{2}\rho P_0\left(1-\hat{m}^2\right)^{-1/4} + P_0^2. \tag{6.22}$$

We now assume that $\hat{m}$ is small, which corresponds to situations in which the cells are close to regular. We also note that since only changes to the free energy are important, we can neglect constant terms. We therefore find that

$$(P-P_0)^2 \approx 2\rho^2\left(1 + \frac{1}{2}\hat{m}^2 + \frac{3}{8}\hat{m}^4\right) - 2\sqrt{2}\rho P_0\left(1 + \frac{1}{4}\hat{m}^2 + \frac{5}{32}\hat{m}^4\right) + \text{const.}, \tag{6.23}$$

$$E = \ldots + \kappa_P\frac{\tilde{\alpha}}{2}\hat{m}^2 + \kappa_P\frac{\tilde{\beta}}{4}\hat{m}^4, \tag{6.24}$$

with

$$\tilde{\alpha} = 2\rho\left(\rho - \frac{P_0}{\sqrt{2}}\right), \tilde{\beta} = \frac{\rho}{2}\left(6\rho - \frac{5}{\sqrt{2}}P_0\right). \tag{6.25}$$

Based on this, we now define the mean field free energy as

$$\epsilon = \text{const.} + \frac{\alpha}{2}m^2 + \frac{\beta}{4}m^4. \tag{6.26}$$

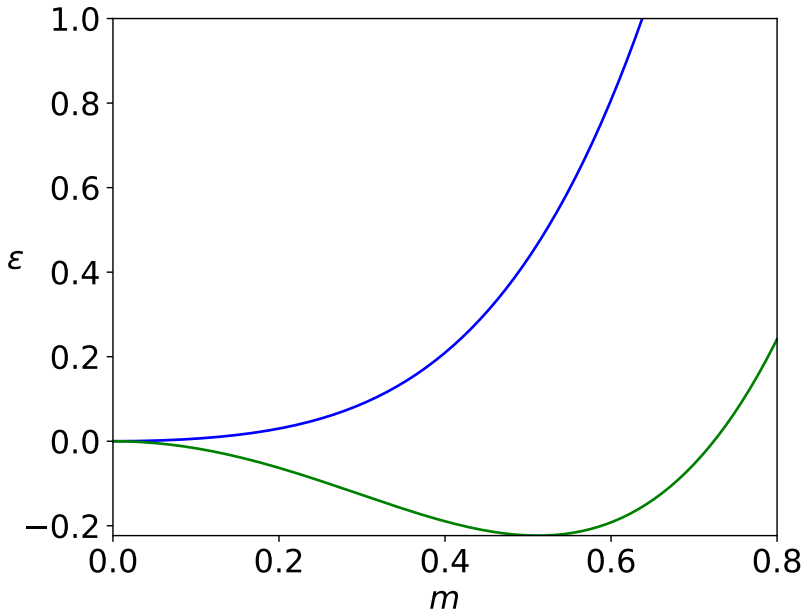

Figure 6.3: Plots of the free energy, ϵ, from Eq. 6.26 as a function of m for $p_0 = 3.75$ (blue) and $p_0 = 4$ (green) with $n = 5$. For the blue curve, $\alpha > 0$ and the minimum is at $m = 0$, while for the green curve, $\alpha < 0$ and $m = 0$ becomes a local maximum, while the minimum occurs at $m = m_0 > 0$.

Setting the target cell shape index $p_0 = P_0/\sqrt{A}$, and including the area terms that have been set to 1, we have that

$$\alpha = 2\rho\left(\rho - p_0\sqrt{\frac{\mu}{2}}\right)\frac{A\kappa_P}{\mu}, \tag{6.27}$$

$$\beta = \frac{\rho}{2}\left(6\rho - 5p_0\sqrt{\frac{\mu}{2}}\right)\frac{A\kappa_P}{\mu}. \tag{6.28}$$

This free energy predicts a bifurcation when α changes sign, which happens at $p_0 = p_0^*(n) \equiv \rho\sqrt{2/\mu}$. For a given n, p_0^* is exactly the shape index of a regular polygon with that number of sides. The free energy therefore has a minimum at some $m > 0$ when p_0 is larger than the shape index of a regular polygon, and at $m = 0$ when the shape index is less than that of a regular polygon, as shown in Fig. 6.3. For $p_0 < p_0^*$, the target cell shape is geometrically impossible for that number of vertices.

In the SPV Model [41], a transition occurs at $p_0 = 3.81 = p_0^*(n = 5)$, which is exactly the transition that this free energy now captures when α changes sign: for $\alpha > 0$, cells are close to regular polygons, and their perimeters have non-zero tension

at equilibrium (the solid phase in the SPV model), and for $\alpha < 0$, the cells are elongated, and their perimeters are all tension-free at equilibrium (the fluid phase in the SPV model). We will therefore set $n = 5$, so that our transition is in the same place.

Dynamical Equations

To derive the dynamical equations for our variables, we use a Poisson Bracket formalism, which is valid for *any* system of close-packed polygons. This derivation was the work of Cristina Marchetti, and is not reproduced here. However, it is closely based on standard results used for liquid crystals, and extremely similar to the derivation in [174]. It should be noted that the derivation in [174] uses different definitions, and as such produces slightly different equations.

Recall from Ch. 2.1.1 that for a velocity field $\mathbf{v}$, we can define the deviatoric rate of strain, d_{ij} and the vorticity, ω_{ij}, as

$$d_{ij} = \frac{1}{2}\left(\partial_i v_j + \partial_j v_i - \delta_{ij}\nabla\cdot\mathbf{v}\right), \tag{6.29}$$

$$\omega_{ij} = \frac{1}{2}\left(\partial_i v_j - \partial_j v_i\right). \tag{6.30}$$

The Poisson Bracket formalism then gives the following form for the time derivatives of R_{ij} and m:

$$\frac{D}{Dt}R_{ij} = Rd_{ij} + R_{ik}d_{kj} + d_{ik}R_{kj} - \delta_{ij}R_{kl}d_{kl} - \Gamma\frac{\delta\mathcal{F}}{\delta R_{ij}}, \tag{6.31}$$

$$\frac{d}{dt}m = \frac{2}{mR}R_{ij}d_{ij} - \Gamma_m\frac{\delta\mathcal{F}}{\delta m}, \tag{6.32}$$

with $\mathcal{F}$ the free energy of the whole system and where

$$\frac{d}{dt} = \partial_t\mathbf{v}\cdot\nabla \tag{6.33}$$

is the convective derivative and

$$\frac{D}{Dt} = \frac{d}{dt} + [\omega, \cdot] \tag{6.34}$$

is the convective and corotational derivative, and $[A, B] = AB - BA$.

There is also an equation for the trace of $\tilde{\mathbf{R}}$, R, generated by this derivation, but for now we will consider R to be constant. This is because we simulate a fixed number of cells in a fixed area, and so some measure of cell size must stay approximately constant by relaxing faster than all other fields. We chose R for this field, as it is the only variable which is directly related to cell size, and is approximately the cell perimeter. Holding R constant therefore corresponds to the assumption that cell perimeter, rather than area is constant, but for small deviations from regular polygons these two scenarios will be approximately equal. For further discussion of this, see Sec. 6.3.3.

Each equation is clearly separated into driving terms, which are coupled to the strain rate tensor, and relaxation terms, which are coupled to the free energy. We will construct the relaxation terms by considering the physics of the system we are modelling.

The relaxational term for m is trivial, as we have already derived a mean field free energy in terms of m. We therefore use Eq. 6.26 as the relevant part of the free energy, and set

$$\frac{\delta \mathcal{F}}{\delta m} = \frac{\partial \epsilon}{\partial m} = \alpha m + \beta m^3. \tag{6.35}$$

For the relaxation terms in R_{ij}, we assume that this will be driven by topological transitions. R_{ij} is a measure of the tissue scale anisotropy, and so it will relax towards zero by reconfigurations of the cells, mainly in the form of T1 transitions. It should therefore include a term proportional to the rate of T1 transitions, and to calculate this we note that in the vertex model, the rate of T1 transitions is roughly proportional to cell elongation. We therefore set this rate to m, and so have that

$$\frac{\delta \mathcal{F}}{\delta R_{ij}} = \frac{m}{\tau_0} R_{ij}, \tag{6.36}$$

with τ_0 the T1 transition timescale.

Applying a shear startup protocol to Eqs.6.31, 6.32 and combining with Eqs.6.35, 6.36, we have that

$$\partial_t R_{xx} = \dot{\gamma} R_{xy} - \frac{m}{\tau_0} R_{xx}, \tag{6.37}$$

$$\partial_t R_{xy} = \dot{\gamma} \left(R - R_{xx}\right) - \frac{m}{\tau_0} R_{xy}, \tag{6.38}$$

$$\partial_t m = \dot{\gamma} \frac{2}{mR} R_{xy} - \frac{1}{\gamma_m} \left(\alpha m + \beta m^3\right), \tag{6.39}$$

with γ_m the shape relaxation timescale. We work in time units in which $\tau_0 = 1$ and set $\gamma_m = 1$ throughout except when explicitly indicated otherwise, which corresponds to setting the shape relaxation rate and T1 transition rate equal. Modifying the ratio of these timescales is seen to have minimal impact on the general qualitative behaviour of all the model versions presented, except where indicated otherwise, and so the exploration of the emergent quantitative phenomenology is left as a future exercise with a successfully constructed continuum model.

To calculate the stress, for now we take that

$$\sigma_{xy} = B R_{xy}, \tag{6.40}$$

and work in units where $B = 1$. For further discussion of this, see Sec. 6.3.2.

Results

The behaviour of this version of the model, which we label version 1, is summarised in Fig. 6.4, and reveals limited success in matching the behaviour seen in the SPV model and set out in Sec. 6.2.

At infinitesimal strains and low strain rate, we do see a transition at $p_0 = 3.81$, which is preserved at high strains, as seen in Fig. 6.4a, in which for $p_0 > 3.81$ the stress is effectively zero at all times. Fig. 6.4c shows how this transition is preserved

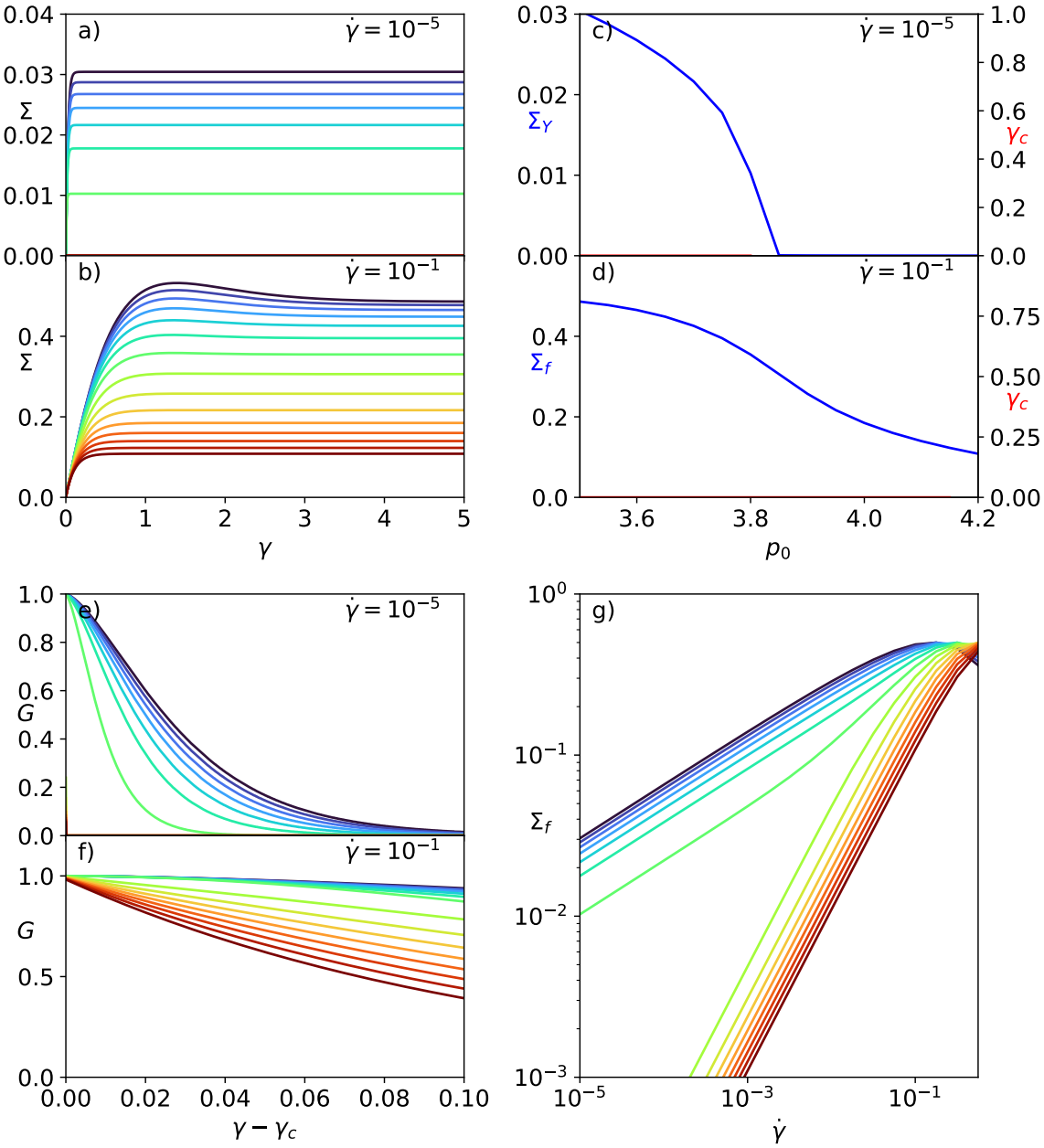

Figure 6.4: Predictions of version 1 of the model, described by Eqs. 6.37, 6.38, 6.39 showing stress as a function of strain at $\dot\gamma = 10^{-5}$ (a) and $\dot\gamma = 10^{-1}$ (b), final stress, $\Sigma_f = \Sigma(\gamma \to \infty)$, and critical strain, γ_c, as a function of p_0 at $\dot\gamma = 10^{-5}$ (c) and $\dot\gamma = 10^{-1}$ (d), instantaneous elastic modulus $G = d\Sigma/d\gamma$ at small strains for $\dot\gamma = 10^{-5}$ (e) and $\dot\gamma = 10^{-1}$ (f) and a flow curve (g) showing final stress as a function of strain rate. Panels a, b, e-g, show $p_0 = 3.50, 3.55, ..., 4.20$ from blue to red. Critical strain is zero for all curves.

in steady state under flow, and appears to show a dynamic yield stress which vanishes at $p_0 = 3.81$ (Ft. 1). However, examination of Fig. 6.4g shows that while there is a qualitative transition, the steady state stress goes to zero at low strain rates for all p_0, and therefore the model has no dynamic yield stress (Ft. 4). Instead, note that

the flow curve shows a power law relationship between stress and strain rate at low strain rate, and the transition seen is instead between exponents in this power law.

Examination of Fig. 6.4a-d shows that at all strain rates, there is no critical strain in this model version (Ft. 2). Similarly, Fig. 6.4e,f show that there is no strain hardening at early strain (Ft. 3), and instead only capture the decreasing gradient of the stress-strain curves as the model approaches its stress maximum. Fig. 6.4a also reveals that the stress overshoot is not present at low strain rates (Ft. 5), although we do see a slight overshoot at high strain rate for some p_0 values.

Indeed, the flow curve highlights a persistent issue with this style of model: the steady state values of the dynamical variables follow power laws in the strain rate. This means that the limiting behaviour as $\dot{\gamma} \to 0$ is exactly the same as the behaviour at $\dot{\gamma} = 0$. This is in contrast to the SPV model, and most vertex models, in which we see a qualitatively different steady state under quasistatic shear than without shear. In the SPV model, $\sigma = 0$ in the unsheared system, but in the steady state under quasistatic shear, we have in general $\sigma \neq 0$, at least for some values of p_0. There is therefore a discrete difference in the stress between zero strain rate and infinitesimal finite strain rate, which is not what we see here for this continuum model.

While this model version does capture some of the desired behaviour, in the form of a transition at $p_0 = 3.81$ which impacts the model at infinitesimal strain (Ft. 1) and in steady state (Ft. 4 qualitatively), it is clearly not a good fit to the SPV Model simulations of [41], and we therefore consider ways in which to adapt it.

6.3.2 Modified Elastic Modulus

To make the first modification, we note that in the previous section, we made an approximation while calculating the stress. Following the Poisson Bracket formalism in full detail, the correct expression for the stress (which we approximated in Eq. 6.40) is

$$\sigma_{ij} = \frac{2}{m} R_{ij} \frac{\delta \mathcal{F}}{\delta m}. \tag{6.41}$$

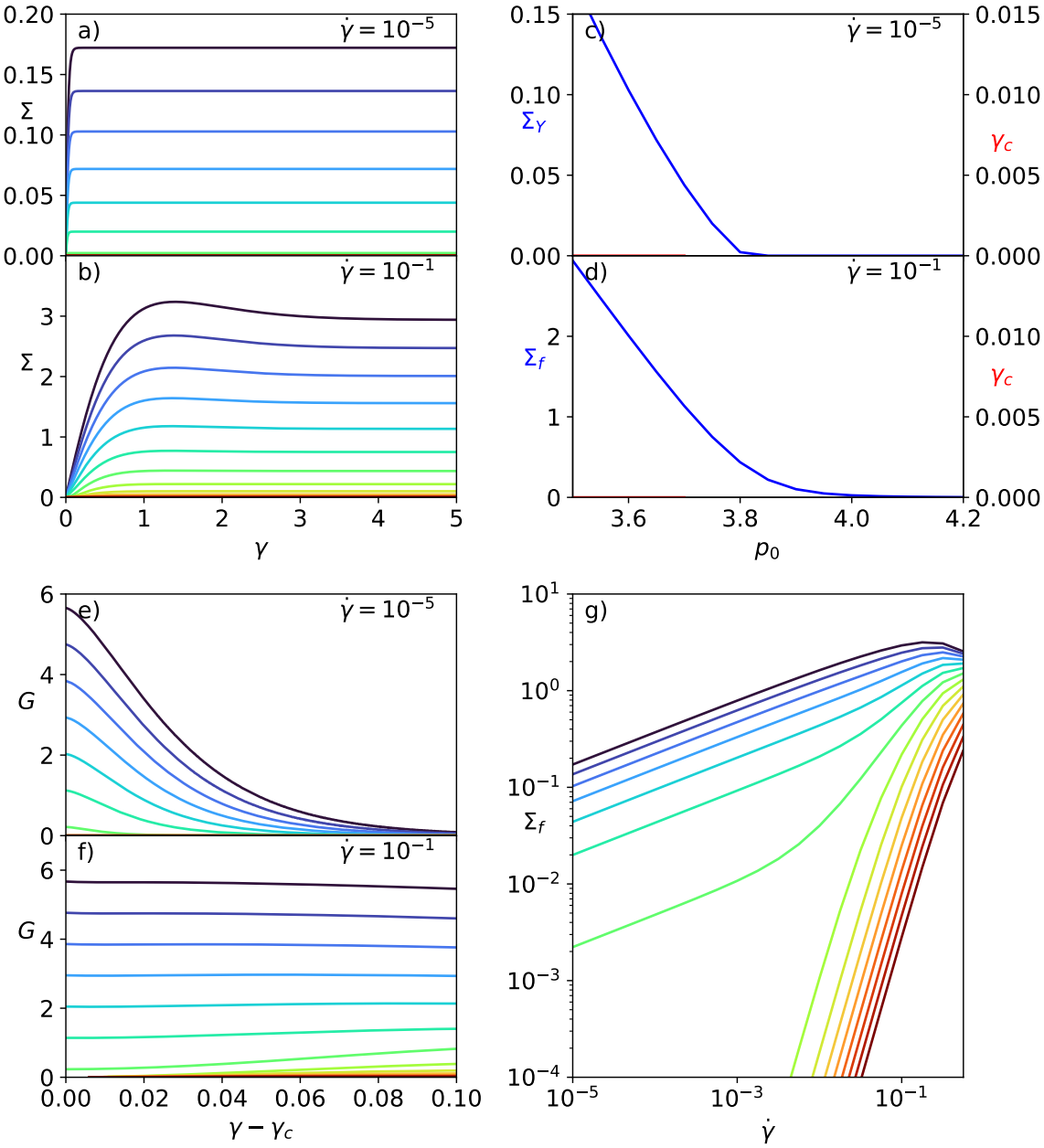

Figure 6.5: Predictions of version 2 of the model, described by Eqs. 6.37, 6.38, 6.39, 6.42 showing stress as a function of strain at $\dot\gamma = 10^{-5}$ (a) and $\dot\gamma = 10^{-1}$ (b), final stress, $\Sigma_f = \Sigma(\gamma \to \infty)$, and critical strain, γ_c, as a function of p_0 at $\dot\gamma = 10^{-5}$ (c) and $\dot\gamma = 10^{-1}$ (d), instantaneous elastic modulus $G = d\Sigma/d\gamma$ at small strains for $\dot\gamma = 10^{-5}$ (e) and $\dot\gamma = 10^{-1}$ (f) and a flow curve (g) showing final stress as a function of strain rate. Panels a, b, e-g, show $p_0 = 3.50, 3.55, ..., 4.20$ from blue to red. Critical strain is zero for all curves.

We therefore now take the stress to be

$$\sigma_{xy} = BR_{xy} = B_0 R_{xy}\left(\alpha + \beta m^2\right), \tag{6.42}$$

now setting $B_0 = 1$.

Recall that in the SPV model, the stress also has a factor which is proportional to dE/dp, and this causes strain hardening at intermediate strains. The new form for the stress includes an equivalent to this term, and so it might be hoped that this will induce strain hardening.

The results of this version of the model, which we label version 2, are summarised in Fig. 6.5, and are broadly similar to those in Sec. 6.3.1. We still see a transition at $p_0 = 3.81$ at low strain rates (Ft. 1), and the flow curve reveals that this represents a qualitative change in the form of the steady state, but the dynamic yield stress is still zero (Ft. 4). There is still no critical strain for any p_0 at any strain rate (Ft. 2) and no stress overshoot at low strain rate (Ft. 5).

We still see no strain hardening (Ft. 3), except for some very weak hardening at high strain rate, which can be understood as follows. When shear begins, $R_{xy} = 0$, and so the loading term in Eq. 6.39 is still zero, meaning that m stays constant at its equilibrium value, while R_{ij} are able to grow. This growth in R_{xy} generates the observed stress increase, which happens at constant elastic modulus. Once $R_{xy} > 0$, the loading term in m becomes non-zero and m is driven away from its equilibrium value, causing an increase in the elastic modulus. However, this happens as R_{ij} are approaching their steady state, and the increasing shear modulus is negligible compared to the decreasing gradient $dR_{xy}/d\gamma$.

This model version still does not capture the behaviour we are looking for, and so we continue to make further modifications. However, as we modify the model further, we will continue to calculate the stress in the way introduced in this section in Eq. 6.42.

6.3.3 Fixing Cell Area

Recall that in Sec. 6.3.1 we set R to be constant, which corresponds to fixing cell perimeter. We now modify that approach, and fix the area of each cell. For a given n, two quantities are sufficient to fully describe each cell for the purposes used here.

Initially we used area and perimeter, which relate directly to the cell shape tensor, then switched to using m and R, with R effectively a measure of perimeter, meaning that the area was in principle calculable. We now switch to describing cells by m and A, which will mean that perimeter and R are both calculable, and will fix A due to assumptions made earlier. As before, we will assume that area relaxation is much faster than any other processes, and so will at all times set R to the value which preserves the cell area.

Without loss of generality, we set $A = \mu(n)$, so that for each cell

$$\lambda_1 = \sqrt{\frac{1+\hat{m}}{1-\hat{m}}}, \tag{6.43}$$

as in Eq. 6.20. We then have that

$$\hat{R} = \lambda_1 + \lambda_2 = \frac{2}{\sqrt{1-\hat{m}^2}}. \tag{6.44}$$

While coarse graining, $\hat{R}$ will be normalised by the cell area, so that

$$R = \frac{2}{\mu(n)} \frac{1}{\sqrt{1-m^2}}. \tag{6.45}$$

This allows to calculate R at each time step, but we will also modify the elastic modulus, so that

$$B \propto \frac{\partial E}{\partial P}, \tag{6.46}$$

with B as defined in Eq. 6.42 and P the perimeter. We have that

$$P = \rho\sqrt{\hat{R}}, \tag{6.47}$$

$$\frac{\partial E}{\partial P} = 2(P - P_0) = 2\left(\rho\sqrt{\hat{R}} - P_0\right), \tag{6.48}$$

so after coarse graining

$$\frac{\partial E}{\partial P} = 2\sqrt{A}\left(\rho\sqrt{R} - p_0\right), \tag{6.49}$$

and we set

$$B = B_0\left(\rho\sqrt{R} - p_0\right). \tag{6.50}$$

By expanding in powers of m, it can be shown that close to the transition, this modulus

$$\left(\rho\sqrt{R} - p_0\right) \propto \alpha + \left(\beta - \frac{5}{4}\alpha\right) m^2, \tag{6.51}$$

and so for small $m, \alpha/\beta$ (near the transition), these two expressions are approximately equivalent.

The results of this version of the model, which we label version 3, are shown in Fig. 6.6 and shown limited improvement from the previous version. We still have a transition at $p_0 = 3.81$ (Ft. 1), but the dynamic yield stress is still zero (Ft. 4). We also still see no critical strain (Ft. 2), no strain hardening (Ft. 3) and no stress overshoot at low strain rate (Ft. 5).

Fig. 6.6d reveals that we now have a non-monotonicity in the steady state stress at high strain rates. This is likely due to the new small discrepancy between the form of the free energy used in the elastic modulus and the form used in the relaxation term for m, and while this difference is insignificant at low strain rate, it becomes significant at high strain rate.

We clearly need to construct a new iteration of the model in order to capture the desired behaviour. We will keep Eq. 6.45, which ensures that the cell area is kept constant rather than cell perimeter, as this corresponds well to the situation we are modelling. However, due to the behaviour we see at high strain rate, we will revert to Eq. 6.41 for the elastic modulus, and ensure that the form of the free energy we use to calculate the modulus is the same as the form used for the relaxation term in m.

6.3.4 Solid Phase Shape Deviations

To make the next modification to the model, we consider the model in its solid phase ($p_0 < p_0^*$) at equilibrium. As currently constructed, m will relax exponentially towards zero, and the equilibrium state has $m = 0$. Recall that $\hat{m}$ describes the elongation of a single cell and is positive-defined, so that $\hat{m} \geq 0$. As a result, even

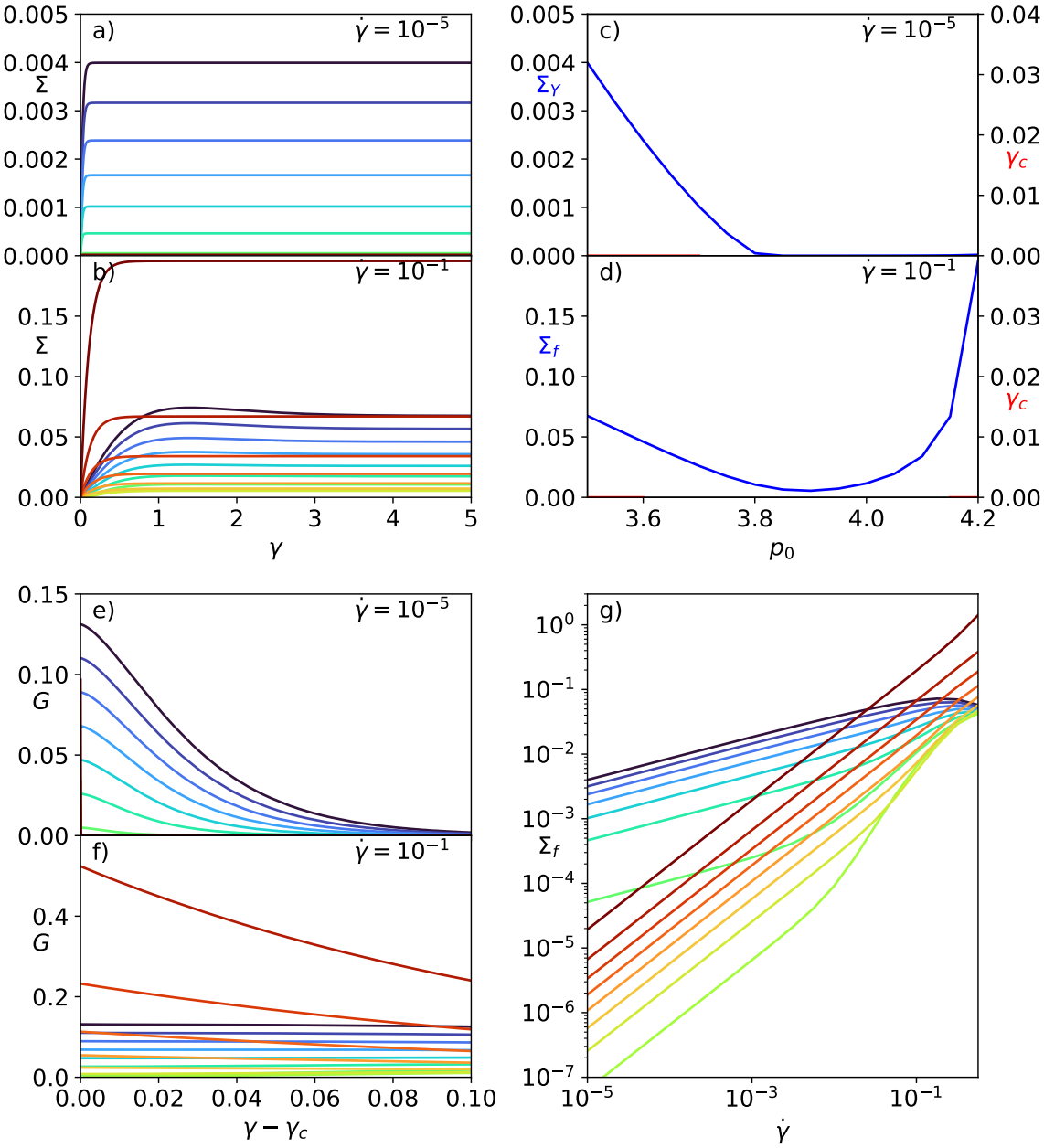

Figure 6.6: Predictions of version 3 of the model, described by Eqs. 6.37, 6.38, 6.39, 6.45, 6.50 showing stress as a function of strain at $\dot\gamma = 10^{-5}$ (a) and $\dot\gamma = 10^{-1}$ (b), final stress, $\Sigma_f = \Sigma(\gamma \to \infty)$, and critical strain, γ_c, as a function of p_0 at $\dot\gamma = 10^{-5}$ (c) and $\dot\gamma = 10^{-1}$ (d), instantaneous elastic modulus $G = d\Sigma/d\gamma$ at small strains for $\dot\gamma = 10^{-5}$ (e) and $\dot\gamma = 10^{-1}$ (f) and a flow curve (g) showing final stress as a function of strain rate. Panels a, b, e-g, show $p_0 = 3.50, 3.55, ..., 4.20$ from blue to red. Critical strain is zero for all curves.

if there are only small local fluctuations in $\hat{m}$, the coarse graining will average over some positive values of $\hat{m}$, but no negative values, and so the coarse grained value $m > 0$. We therefore expect that small random fluctuations will in general give $m \neq 0$, even for $p_0 < p_0^*, \dot\gamma = 0$.

Examination of the SPV model reveals that this is indeed the case, and it is found that without shear, for $p_0 < p_0^*$, $m \approx m_s$, with $m_s = 0.159$. We therefore aim to modify our equations such that m relaxes to some $m_s \neq 0$, which we set from the SPV model

We start with the free energy from Eq. 6.26, and now use a Lagrange multiplier with Karush-Kuhn-Tucker conditions [178, 179] to minimise it under the constraint $m \geq m_s$:

$$\mathcal{L}(m, \lambda) = \frac{\alpha}{2} m^2 + \frac{\beta}{4} m^4 + \lambda (m - m_s). \tag{6.52}$$

This is minimised when

$$\frac{\partial \mathcal{L}}{dm} = \alpha m + \beta m^3 + \lambda = 0, \tag{6.53}$$

$$\frac{\partial \mathcal{L}}{d\lambda} = m - m_s = 0, \tag{6.54}$$

which is satisfied by

$$m^* = m_s, \lambda^* = -\left(\alpha + \beta m_s^2\right) m_s. \tag{6.55}$$

We use this to construct a new free energy,

$$\bar{\epsilon} = \frac{\alpha}{2} m^2 + \frac{\beta}{4} m^4 - m m_s \left(\alpha + \beta m_s^2\right), \tag{6.56}$$

which is minimised by the value of m which minimises Eq. 6.26 when it is subject to the constraint $m \geq m_s$. We will use this free energy for the relaxation of m, and it has minima at

$$m = m_s \text{ for } \alpha > -3\beta m_s^2, \tag{6.57}$$

$$m = -\frac{m_s}{2} + \frac{1}{2}\sqrt{-4\frac{\alpha}{\beta} - 3m_s^2} \text{ for } \alpha < -3\beta m_s^2. \tag{6.58}$$

Note that the transition point has been perturbed to lower α, which is as expected: for $-3\beta m_s^2 < \alpha < 0$, the steady state of the previous free energy was $0 < m < m_s$, whereas that whole range now has $m = m_s$ at equilibrium. Despite this shift in the transition, we still use $n = 5$.

Eq. 6.39 is now replaced by

$$\partial_t m = \dot{\gamma}\frac{2}{mR}R_{xy} - \frac{1}{\gamma_m}\left(\alpha m + \beta m^3 - m_s\left(\alpha + \beta m_s^2\right)\right), \tag{6.59}$$

and the stress is calculated as

$$\sigma_{xy} = \frac{2}{m - m_s}R_{xy}\frac{\delta\mathcal{F}}{\delta m} = B_0 R_{xy}\left[\alpha + \beta\left(m^2 + m m_s + m_s^2\right)\right]. \tag{6.60}$$

The results of this version of the model, which we label version 4, are shown in Fig. 6.7, and still show little improvement. The dynamic yield stress is still zero (Ft. 4), and the transition at low strain rate (Ft. 1) is now shifted to $p_0 \approx 3.9$, as expected. We still see no critical strain, no strain hardening and no stress overshoot at low strain rate (Ft. 2,3,5).

We therefore need a new iteration of the model, and as the latest modification has had minimal impact on the results and is not related to the original model assumptions, we will not continue with this form for the free energy, and instead will revert to Eq. 6.26. In addition to this logical premise, exploring the below model versions with the addition of this modification reveals that it can produce undesired behaviour.

6.3.5 Cellular Tilt

For the next modification, we note that there is a degree of freedom for each cell that has so far been neglected. Recall that in the SPV model, the critical strain is a result of the fact that as strain starts, the cells initially tilt without stretching, before beginning to elongate once the tilt is saturated. We now modify the model to account for this tilt.

From this point on, we set $n = 4$, which will change the transition point to $p_0 = 4$. This is not for any physical reason, but because the symmetry of a quadrilateral makes the following derivation possible, while it has not yet been successfully carried out for general n.

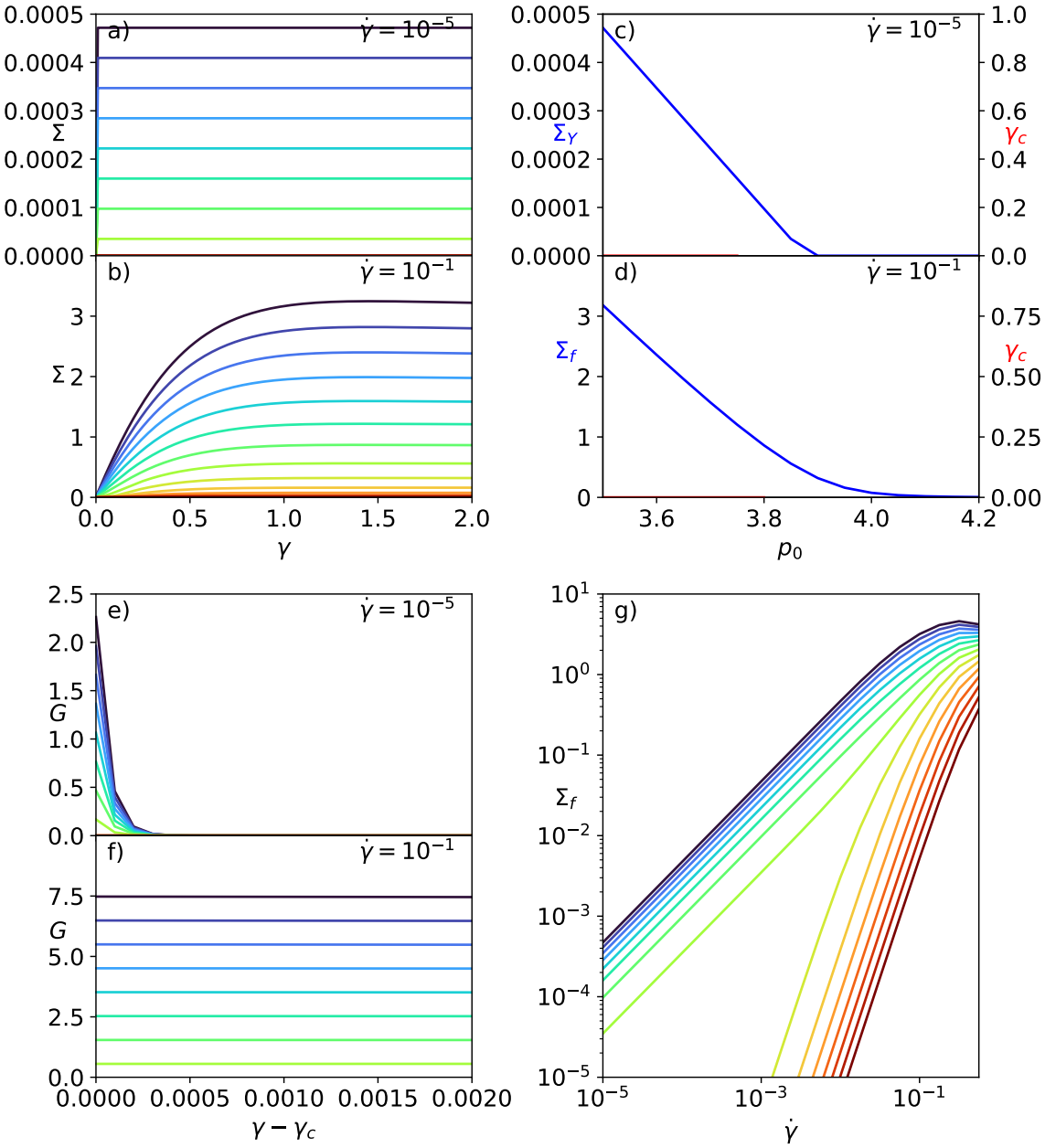

Figure 6.7: Predictions of version 4 of the model, described by Eqs. 6.37, 6.38, 6.59, 6.45, 6.60 showing stress as a function of strain at $\dot\gamma = 10^{-5}$ (a) and $\dot\gamma = 10^{-1}$ (b), final stress, $\Sigma_f = \Sigma(\gamma \to \infty)$, and critical strain, γ_c, as a function of p_0 at $\dot\gamma = 10^{-5}$ (c) and $\dot\gamma = 10^{-1}$ (d), instantaneous elastic modulus $G = d\Sigma/d\gamma$ at small strains for $\dot\gamma = 10^{-5}$ (e) and $\dot\gamma = 10^{-1}$ (f) and a flow curve (g) showing final stress as a function of strain rate. Panels a, b, e-g, show $p_0 = 3.50, 3.55, ..., 4.20$ from blue to red.

Consider a rectangle with sides length a_1, a_2 and vertices at $\mathbf{r}^a$ which is deformed into a parallelogram by a transformation D_{ij} so that the new vertices are at $\mathbf{r}_i'^a =$

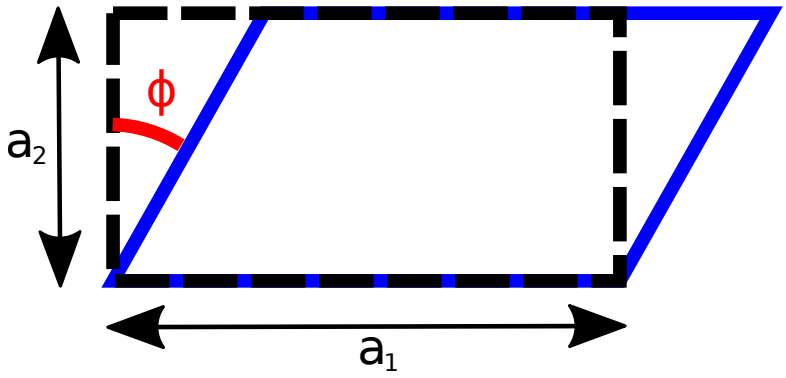

Figure 6.8: Sketch of a quadrilateral being deformed such that it tilts.

$D_{ij}\mathbf{r}_j^a$, as shown in Fig. 6.8, with

$$\mathbf{D} = \begin{bmatrix} 1 & \tan\phi \\ 0 & 1 \end{bmatrix}, \tag{6.61}$$

so that $|\mathbf{D}| = 1$. The modified shape tensor is now

$$\hat{\tilde{\mathbf{R}}} = \mathbf{D} \cdot \hat{\tilde{\mathbf{R}}}_\mathbf{0} \cdot \mathbf{D}^\mathbf{T}, \tag{6.62}$$

with

$$\hat{\tilde{\mathbf{R}}}_\mathbf{0} = \frac{1}{4}\begin{bmatrix} a_1^2 & 0 \\ 0 & a_2^2 \end{bmatrix}, \tag{6.63}$$

$$\hat{\tilde{\mathbf{R}}} = \frac{1}{4}\begin{bmatrix} a_1^2 + a_2^2\tan^2\phi & a_2^2\tan\phi \\ a_2^2\tan\phi & a_2^2 \end{bmatrix}. \tag{6.64}$$

The determinant and trace of $\hat{\tilde{\mathbf{R}}}$ are now given by

$$\mathrm{Det}\left[\hat{\tilde{\mathbf{R}}}\right] = \frac{a_1^2 a_2^2}{16} = \frac{A^2}{16}, \tag{6.65}$$

$$\mathrm{Tr}\left[\hat{\tilde{\mathbf{R}}}\right] = \frac{1}{4}\left[a_1^2 + a_2^2\left(1 + \tan^2\phi\right)\right]. \tag{6.66}$$

Calculating ϕ

If we take the undeformed cell to be a square of area $A = 1$, we have that

$$\hat{\tilde{\mathbf{R}}} = \frac{1}{4}\begin{bmatrix} 1+\tan^2\phi & \tan\phi \\ \tan\phi & 1 \end{bmatrix}, \tag{6.67}$$

and the traceless shape tensor

$$\hat{\mathbf{R}} = \frac{1}{4}\begin{bmatrix} \frac{\tan^2\phi}{2} & \tan\phi \\ \tan\phi & -\frac{\tan^2\phi}{2} \end{bmatrix}, \tag{6.68}$$

so that

$$\hat{R}_{ij}\hat{R}_{ji} = \frac{\tan^2\phi}{8}\left(1+\frac{1}{4}\tan^2\phi\right) \approx \frac{1}{8}\tan^2\phi, \tag{6.69}$$

with the approximation for small ϕ. While this is strictly derived for a square, we will assume that it is approximately correct for other quadrilaterals with small m. Noting that upon coarse graining, the shape tensor will be normalised by the cell area, which we have set to 1, we can therefore calculate ϕ in mean field from

$$\tan^2\phi = 8R_{ij}R_{ji}. \tag{6.70}$$

Free Energy

To derive the new free energy, we first set $A = 1$ (note that $\mu(4) = 4$), which gives us that

$$\hat{R} = \frac{1}{2}\frac{1}{\sqrt{1-\hat{m}^2}}. \tag{6.71}$$

The perimeter of the deformed cell is then given by

$$\begin{aligned} P =& 4\sqrt{\hat{R} + 2\sqrt{\mathrm{Det}\left[\hat{\tilde{\mathbf{R}}}\right]\left(1+\tan^2\phi\right)}} \\ =& 4\sqrt{\frac{1}{2}\frac{1}{\sqrt{1-\hat{m}^2}} + \frac{\sqrt{1+\tan^2\phi}}{2}}. \end{aligned} \tag{6.72}$$

We set

$$q \equiv \sqrt{\frac{1}{2}+\frac{1}{2}\sqrt{1+\tan^2\phi}}, \tag{6.73}$$

so that

$$\begin{aligned} P =& 4\sqrt{\frac{1}{2}\frac{1}{\sqrt{1-\hat{m}^2}}+q^2-\frac{1}{2}} \\ \approx& 4\sqrt{\frac{1}{2}\left(\frac{\hat{m}^2}{2}+\frac{3}{8}\hat{m}^4\right)+q^2}, \end{aligned} \tag{6.74}$$

where as usual, we assume $\hat{m}$ to be small. Considering only the perimeter term in the free energy, we then expand $(P - P_0)$ up to quartic terms in $\hat{m}$ and find that

$$E = \kappa_P \left[\zeta + \frac{\tilde{\alpha}}{2}\hat{m}^2 + \frac{\tilde{\beta}}{4}\hat{m}^4\right], \tag{6.75}$$

with

$$\zeta = \left(P_0 - 4q\right)^2, \tag{6.76}$$

$$\tilde{\alpha} = 2\left(4q - P_0\right)\frac{1}{q}, \tag{6.77}$$

$$\tilde{\beta} = \frac{1}{4}\left(48q^3 - 12P_0q^2 + P_0\right)\frac{1}{q^3}. \tag{6.78}$$

We now define the critical shape index,

$$p_c\left(\phi\right) = 4q = 4\sqrt{\frac{1}{2}+\frac{1}{2}\sqrt{1+\tan^2\phi}} \approx 4\left(1+\frac{1}{8}\tan^2\phi\right). \tag{6.79}$$

Noting that $p_0^*\left(n=4\right) = 4$ and $A = 1$, we can now construct the mean-field free energy:

$$\epsilon = \text{const.} + \frac{\alpha}{2}m^2 + \frac{\beta}{4}m^4, \tag{6.80}$$

with

$$\alpha = 8\left(p_c - p_0\right)\frac{1}{p_c} \approx 2\left(p_0^* - p_0\right) + \frac{1}{4}p_0^*\tan^2\phi + \mathcal{O}\left(\tan^4\phi\right), \tag{6.81}$$

$$\begin{aligned} \beta =& 16\left(\frac{3}{4}p_c - \frac{3}{4}p_0 + \frac{p_0}{p_c^2}\right)\frac{1}{p_c} \\ \approx& \frac{1}{4}\left(12p_0^* - 11p_0\right) + \frac{1}{4}\tan^2\phi\left(\frac{3}{2}p_0^* - p_0\right) + \mathcal{O}\left(\tan^4\phi\right), \end{aligned} \tag{6.82}$$

where we are also assuming $\tan^2\phi$ to be small. From here, we will also neglect the $\tan^2\phi$ terms in the equation for β, and we use Eq. 6.70 to substitute in for ϕ, giving our final expressions:

$$\alpha = 2\left[p_0^*\left(1 + R_{ij}R_{ij}\right) - p_0\right], \tag{6.83}$$

$$\beta = \frac{1}{4}\left[12p_0^* - 11p_0\right]. \tag{6.84}$$

For $p_0 < p_0^*$, we still have that $\alpha > 0, \beta > 0$, and so the equilibrium state has $m = 0$, as before. For $p_0 > p_0^*$ (and $p_0 < 12p_0^*/11$, which is a limit of the approximations we have taken), in equilibrium, $R_{ij} = 0$, so $m > 0$, but then as the system is sheared, R_{ij} grow, and α also grows as a result of the cells tilting, until $\tan\phi$ becomes saturated when R_{ij} reach their steady state values. This means that there are now two process affecting the free energy as shear begins: the changes in m which existed previously and the changes in ϕ, which modify the behaviour of m.

However, this actually means that as the system is strained, m gets further from the free energy minimum, which will have the effect of increasing the elastic modulus. To counteract this, we set $\gamma_m = 10^{-2}$, which corresponds to making m relax much faster than R_{ij}. This will allow the value of m to slowly decrease while following the free energy minimum as $\tan\phi$ increases, until ϕ reaches its maximum, at which point m is forced away from the free energy minimum.

Results

The results of this version of the model, which we label version 5, are shown in Fig. 6.9, and reveal behaviour that is broadly similar to previous model versions, but with some improvements. The model now successfully displays a clear critical strain at high strain rates (Ft. 2), and also succeeds in showing some strain hardening at high strain rates (Ft. 3), although fails to capture a dynamic yield stress (Ft. 4) and fails to show a stress overshoot at low strain rate (Ft. 5), despite a very pronounced overshoot at high strain rate. At low strain rates the transition (Ft. 1)

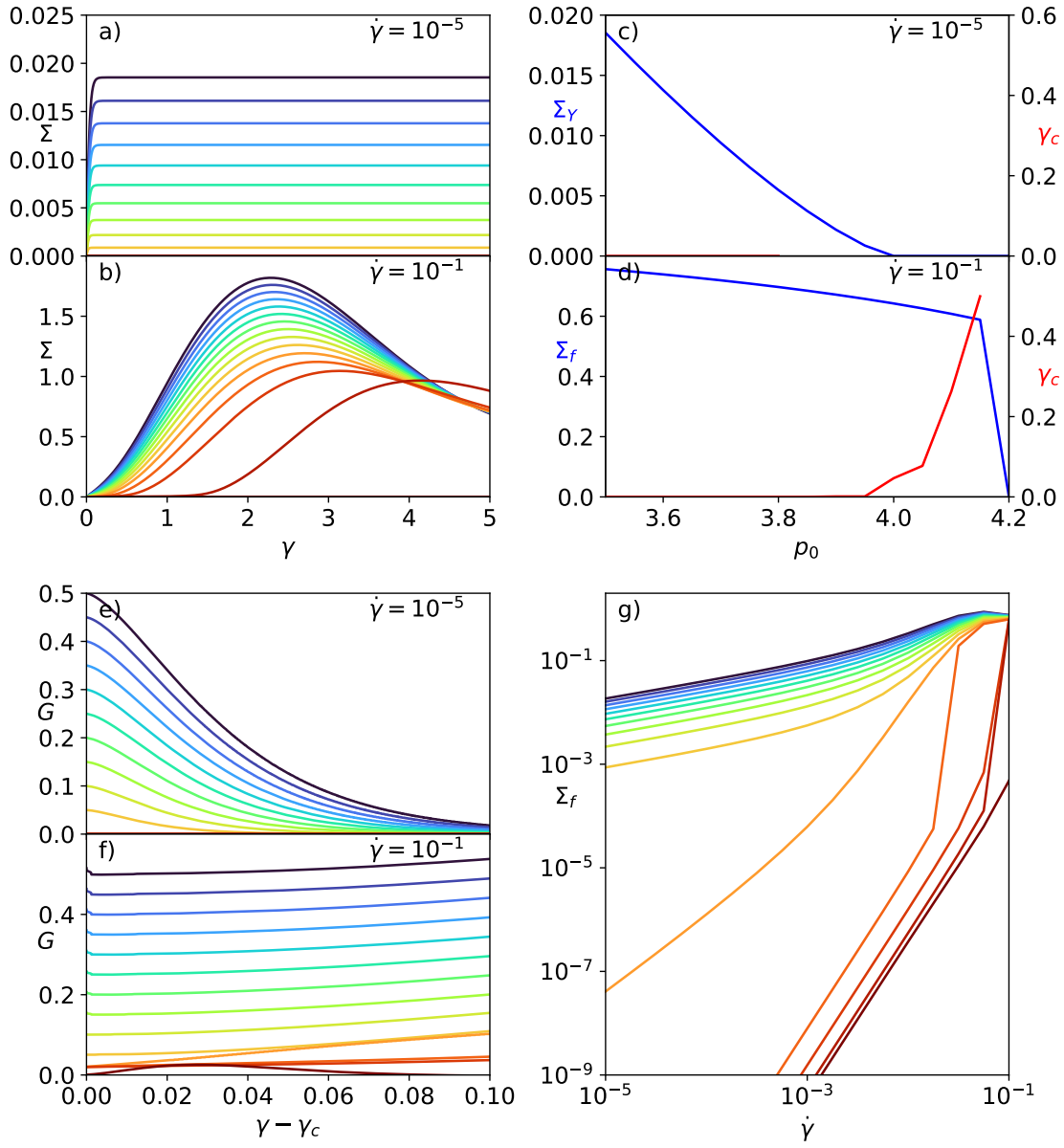

Figure 6.9: Predictions of version 5 of the model, described by Eqs. 6.37, 6.38, 6.39, 6.45, 6.42, 6.83, 6.84 with $\gamma_m = 10^{-2}$ showing stress as a function of strain at $\dot\gamma = 10^{-5}$ (a) and $\dot\gamma = 10^{-1}$ (b), final stress, $\Sigma_f = \Sigma(\gamma \to \infty)$, and critical strain, γ_c, as a function of p_0 at $\dot\gamma = 10^{-5}$ (c) and $\dot\gamma = 10^{-1}$ (d), instantaneous elastic modulus $G = d\Sigma/d\gamma$ at small strains for $\dot\gamma = 10^{-5}$ (e) and $\dot\gamma = 10^{-1}$ (f) and a flow curve (g) showing final stress as a function of strain rate. Panels a, b, e-g, show $p_0 = 3.50, 3.55, ..., 4.20$ from blue to red.

is now shifted to $p_0 = 4$, as expected from changing to $n = 4$.

While there is still no critical strain at low strain rate, the high strain rate plots show that there is now a critical strain, which emerges at $p_0 \approx 3.95$ and grows with increasing p_0, until some larger value of p_0, at which point the stress response at all

times drops to almost zero, and the critical strain is poorly defined. The emergence of a second critical point at a lower p_0 than the critical point for the final stress has occurred naturally, and is a significant success of this model version.

This model version also shows a new, unexpected emergent phenomenon: discontinuous shear thickening. Inspection of Fig. 6.9g shows that for $p_0 > 4$, there is some finite strain rate $\dot{\gamma}_t$ at which there is a discontinuity in the flow curve, so that the steady state stress for a strain rate immediately below $\dot{\gamma}_t$ is different to the steady state stress for a strain rate immediately above $\dot{\gamma}_t$, $\Sigma_f(\dot{\gamma}_t - \delta\dot{\gamma}) \neq \Sigma_f(\dot{\gamma}_t + \delta\dot{\gamma})$ in the limit $\delta\dot{\gamma} \to 0$. This effect was not observed in the SPV model, but this is to be expected as it is a finite strain rate process, and the SPV simulations are quasistatic.

This model version has shown improved success from previous versions, and we now have a critical strain at high strain rates (Ft. 2), and two separate transition points in p_0 (Ft. 1,4). An interesting new phenomenon has also emerged in the form of discontinuous shear thickening. However, there is still no critical strain at low strain rates (Ft. 2), no dynamic yield stress (Ft. 4), limited strain hardening (Ft. 3) and no stress overshoot at low strain rate (Ft. 5), so we will explore further modifications to the model.

6.3.6 Dynamic Fluidity

The derivation of the variation of the model presented in this section is credited to Suzanne Fielding.

A significant recurring problem so far has been that for all the model versions, their steady state in the limit $\dot{\gamma} \to 0$ is equal to their behaviour at zero strain rate, which means that the majority of the interesting phenomenology occurs at high strain rate, and is absent at low strain rate. Inspection of Eqs. 6.37, 6.38, 6.39 reveals that generating a discontinuity at infinitesimal strain rate will require a significant change to the model.

Previously, we used m as the T1 transition rate, which governs the relaxation

of R_{ij}. We now introduce an additional scalar field, a, which is used as a dynamic fluidity controlling the T1 rate. Eqs. 6.37, 6.38 now become

$$\partial_t R_{xx} = \dot{\gamma} R_{xy} - a R_{xx}, \tag{6.85}$$

$$\partial_t R_{xy} = \dot{\gamma} \left(R - R_{xx} \right) - a R_{xy}, \tag{6.86}$$

while the equation for $\partial_t m$ remains as before. a then has its own dynamical equation, which we construct phenomenologically:

$$\partial_t a = 2\sqrt{d_{ij} d_{ij}} a \left(1 - \tau_0 a \right) - a^2, \tag{6.87}$$

which for shear startup becomes

$$\partial_t a = \sqrt{2} \dot{\gamma} a \left(1 - \tau_0 a \right) - a^2. \tag{6.88}$$

In steady state,

$$a = \frac{\sqrt{2}\dot{\gamma}}{1 + \sqrt{2}\tau_0 \dot{\gamma}} \approx \sqrt{2}\dot{\gamma}, \tag{6.89}$$

where the approximation is at low strain rate. Crucially, this steady state value is independent of R_{ij}, which was not the case for the previous T1 transition rate, m. The result of this is that at low strain rates, including the limit $\dot{\gamma} \to 0$, the steady state values of R_{ij} are given by

$$R_{xx} = \frac{R}{3}, R_{xy} = \frac{R\sqrt{2}}{3}. \tag{6.90}$$

By contrast, without shear, the steady state values are $R_{xx} = R_{xy} = 0$, although this does require the assumption that random noise ensures a is not exactly zero at all times while in equilibrium. The imposition of an infinitesimal strain rate therefore generates a discrete jump in the steady state, which is exactly what we were searching for.

The results of this version of the model, which we label version 6, are shown in Fig. 6.10, and show significant success. There is now a clear dynamic yield stress (Ft.

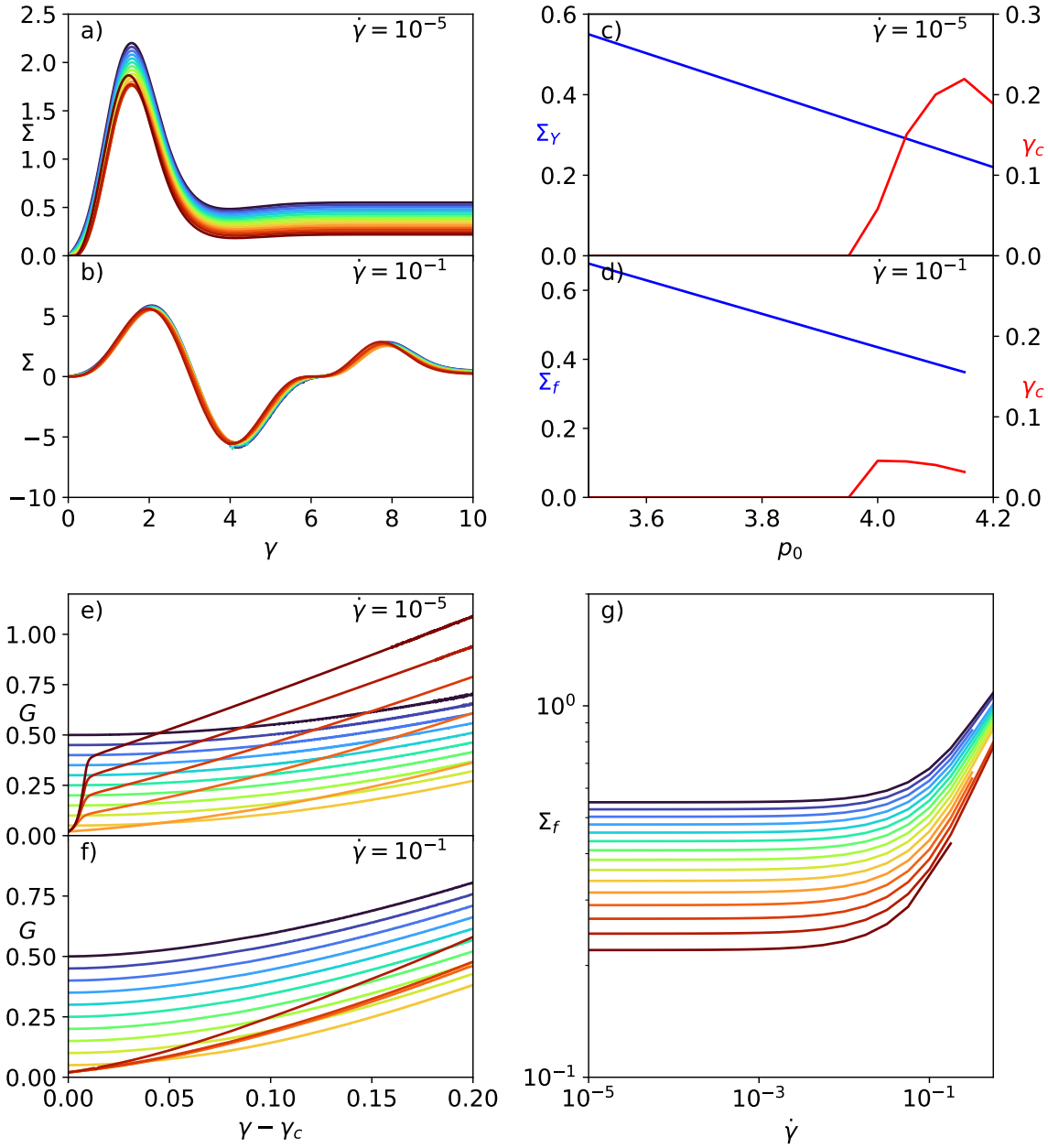

Figure 6.10: Predictions of version 6 of the model, described by Eqs. 6.85, 6.86, 6.39, 6.87, 6.45, 6.42, 6.83, 6.84 with $\gamma_m = 1$ showing stress as a function of strain at $\dot\gamma = 10^{-5}$ (a) and $\dot\gamma = 10^{-1}$ (b), final stress, $\Sigma_f = \Sigma(\gamma \to \infty)$, and critical strain, γ_c, as a function of p_0 at $\dot\gamma = 10^{-5}$ (c) and $\dot\gamma = 10^{-1}$ (d), instantaneous elastic modulus $G = d\Sigma/d\gamma$ at small strains for $\dot\gamma = 10^{-5}$ (e) and $\dot\gamma = 10^{-1}$ (f) and a flow curve (g) showing final stress as a function of strain rate. Panels a, b, e-g, show $p_0 = 3.50, 3.55, ..., 4.20$ from blue to red. Missing data in panel (g) are runs where numerical issues prevented the completion of the simulation before steady state was reached.

4), and Fig 6.10c shows that this should indeed vanish at some $p_0 > 4$. However, the approximations we made in deriving this model version are only valid for $p_0 < 4.21$, (at which point $-\alpha = \beta$ when $\phi = 0$) and so for now we are unable to simulate the

model above the transition.

We also have a critical strain at high and low strain rate (Ft. 2), and this vanishes for $p_0 \lesssim 3.9$, which is lower than the value at which the dynamic yield stress should vanish. Although both critical p_0 values are higher than their counterparts in the SPV model, note that we have assumed $n = 4$; if we had instead assumed $n = 5$, we would expect a transition which we see occur at $p_0 = 4$ to occur at $p_0 = 3.81$. In fact, the projected x-intercept of the dynamic yield stress is close to $p_0^*(n = 3)$, which implies that perhaps simulating at $n = 5$ would also shift the transition point in the dynamic yield stress to be close to $p_0 = 4$.

Inspection of Fig. 6.10e,f reveals that this model version also shows significant strain hardening, at both high and low strain rate (Ft. 3). At low strain rate, there appears to be a significant region in which the shear modulus grows linearly with strain, which is consistent with the hardening we might expect to see from the quadratic term in the free energy, which generates a linear term in the elastic modulus.

Fig. 6.10a reveals that we do have a stress overshoot at low strain rate (Ft. 5). However, examination of Fig. 6.11, which shows the overshoot height (stress maximum minus final stress) as a function of strain rate, including for startup curves not shown in Fig. 6.10, reveals that the overshoot height decreases with strain rate and appears to tend to zero as $\dot{\gamma} \to 0$, which implies that in the quasistatic limit this overshoot would disappear.

Fig. 6.10b shows unusual behaviour at high strain rate, and in fact there are several numerical issues with simulating in that regime. Previously, all the stress-strain curves have either increased monotonically towards steady state or shown a single stress overshoot before relaxing to steady state. Now instead, we see a curve with multiple stationary points, and a considerable period of negative stress. A negative stress does not make physical sense - it implies that to shear the system in one direction, a force would need to be applied in the opposite direction. This is not behaviour which has been seen in vertex models or experimental data, and we

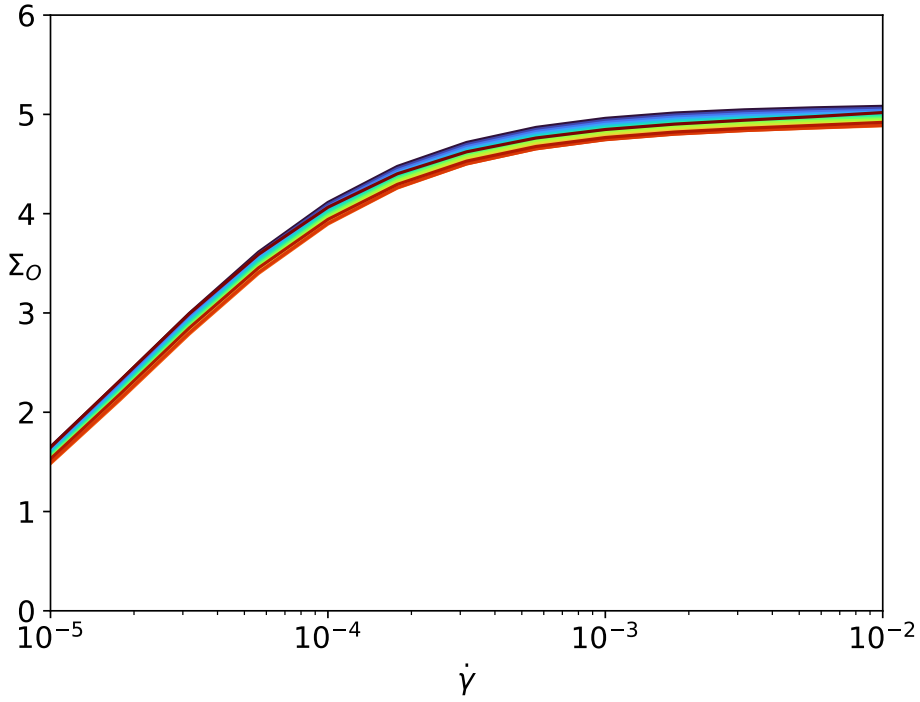

Figure 6.11: Overshoot height, Σ_O, as a function of strain rate, $\dot{\gamma}$, for $p_0 = 3.50, 3.55, ..., 4.20$ from blue to red.

suggest that it is an artefact of imperfect transient dynamics, likely caused by the complex interactions between the four dynamic scalar fields, and we would expect an improved model to not show this behaviour.

The data that we are able to generate suggests an important transition at some p_0 outside of our simulation range. In an attempt to observe this, we will make an additional assumption, and set $\beta = \beta\,(p_0 = 4) = 1$. This avoids the issues associated with $\beta \leq 0$, and moves the point at which $-\alpha\,(\phi = 0) = \beta$ to $p_0 = 4.5$. With some careful dynamics, we can simulate past this, provided that in steady state $-\alpha < \beta$, although the transient behaviour of the startup curves will show slightly different behaviour for $p_0 > 4.5$. We label this model version 6b.

The results for the regime in which there are no numerical issues are summarised in Fig 6.12. The behaviour for $p_0 < 4.2$ is very similar to Fig. 6.10, and we are now able to see how the dynamic yield stress vanishes at $p_0 \approx 4.65$ (Ft. 4). Fig. 6.12g shows that we now have two qualitatively different forms of flow curve: for $p_0 \lesssim 4.65$, the steady state stress tends to a constant as $\dot{\gamma} \to 0$, while for $p_0 \gtrsim 4.65$,

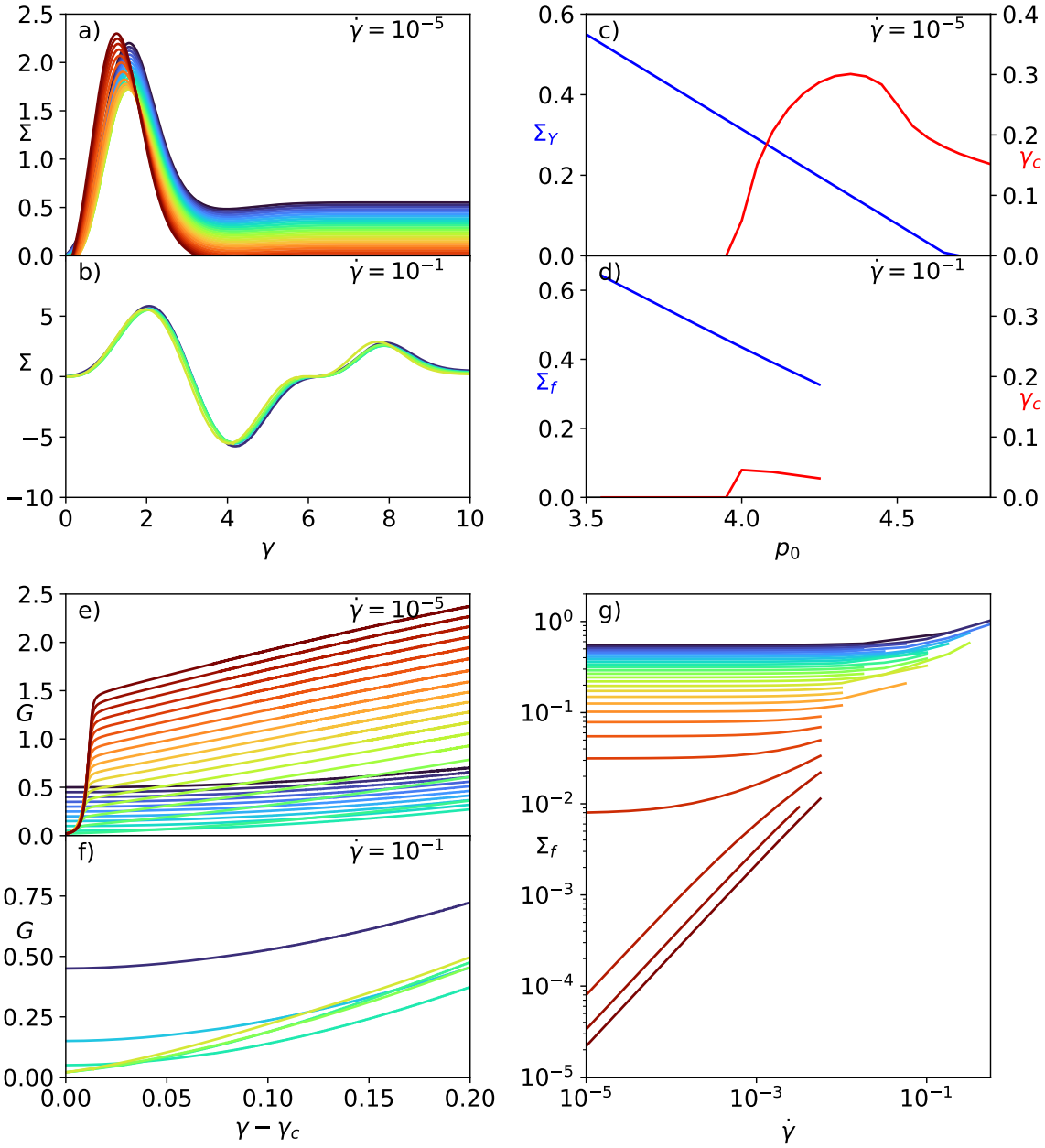

Figure 6.12: Predictions of version 6b of the model, described by Eqs. 6.85, 6.86, 6.39, 6.87, 6.45, 6.42, 6.83, with $\beta = 1$ showing stress as a function of strain at $\dot\gamma = 10^{-5}$ (a) and $\dot\gamma = 10^{-1}$ (b), critical strain, γ_c, as a function of p_0 at $\dot\gamma = 10^{-5}$ (c) and $\dot\gamma = 10^{-1}$ (d), instantaneous elastic modulus $G = d\Sigma/d\gamma$ at small strains for $\dot\gamma = 10^{-5}$ (e) and $\dot\gamma = 10^{-1}$ (f) and a flow curve (g) showing final stress as a function of strain rate. Panels a, b, e-g, show $p_0 = 3.50, 3.55, ..., 4.80$ from blue to red. Missing data in panel (g) are runs where numerical issues prevented the completion of the simulation before steady state was reached.

the steady state stress is a power law in strain rate, and so vanishes as $\dot\gamma \to 0$. Note that while the critical strain appears to be non-monotonic in p_0 at low strain rate, the point at which the curve changes direction coincides with the point where model

assumptions begin to break down, so the values of γ_c at high p_0 may be inaccurate.

This latest model version, although not perfect at capturing the behaviour of the SPV model, is therefore able to capture qualitatively at least four of the phenomena we were searching for: we have a solid-fluid transition for infinitesimal strains at $p_0 \approx 3.9$ (Ft. 1), a critical strain which must be applied to the system in the fluid state before any stress is measured (Ft. 2), strain hardening at intermediate strains (Ft. 3) and a dynamic yield stress which vanishes at $p_0 \approx 4.65$ (Ft. 4). We see a stress overshoot at low strain rate (Ft. 5), but it appears that the height of the overshoot, $\Sigma_O \to 0$ in the quasistatic limit.

6.4 Conclusion

We have constructed and presented a number of variants of a continuum model of epithelial tissue in an attempt to capture the key behaviour seen in simulations of the SPV model, as described in Sec. 6.2. The simplest model versions presented showed only limited success, but the final model versions presented capture a significant portion of the qualitative behaviour. All of them share the same basic approach, using a coarse grained cell shape tensor and cell elongation parameter, with dynamical equations derived from a Poisson bracket formalism, and a free energy constructed from the form used in the vertex model. While none of the model versions presented capture perfectly the behaviour of the SPV model from [41], or indeed any other published vertex models, the final continuum model does capture a significant portion of the desired behaviour, and represents a good approximation to the SPV model. The behaviour of our final model version in the quasistatic limit is, in fact, qualitatively very similar to [41], and the main difference is in the values of the model parameters at which key transitions occur: the SPV model has a transition between solid-like and fluid-like states without shear at $p_0 = 3.81$ and a dynamic yield stress which vanishes at $p_0 \approx 4$, while the final version of this model has a transition in the absence of shear at $p_0 = 4$ and a dynamic yield stress which vanishes at $p_0 \approx 4.65$.

However, we were aiming to construct a model which worked at finite strain rate as well as low strain rate, and the final model shows some unexpected and unphysical behaviour at higher strain rates.

For the derivation of all the model versions presented, it was necessary to make several assumptions and approximations, which limit the window in which the model is valid. In the final version presented, this window became small enough that there was some interesting behaviour outside of it. To address this in a future model, it would be interesting to derive the free energy in terms of m for fixed cell area instead of perimeter. To do so is trivial for the early model versions presented, and tends to leave looser limits on the model validity. In following that approach, R would need to be calculated to preserve cell perimeter, instead of area, and the result would model a system of cells in which the cell area varies with time, although within certain small limits due to the constraint of constant perimeter.

The reader may also note that in addition to the model versions presented here, there are many others which could be constructed by combining the parts in different ways, and most model versions have at least one constant which could be varied. A significant fraction of these additional variations have been explored by the author, and this work represents an attempt to present the most interesting ones in a logical order. However, it is completely plausible that there are other interesting but unexplored models that can be generated from these analyses, and perhaps one of these matches the behaviour of the SPV model even better than the ones presented.

In presenting a number of these model versions, we have shown the utility and necessity of several different model features, and the results show that there are two adaptations to the simplest model, based on that presented in [174], which are necessary.

Firstly, the analysis in Sec. 6.3.5 proved to be necessary to generate a critical strain, and was particularly effective in combination with a dynamic fluidity. It therefore seems that including a hidden variable for cellular tilt is an effective way to generate two degrees of freedom in the tissue's response to shear. The introduction

of ϕ into the free energy means that for $p_0 > p_0^*$, the free energy has a series of degenerate minima at different ϕ, and as the system is sheared, it moves between these minima in a very similar way to the SPV model. In the model presented here, this was directly coupled to the cell shape tensor and incorporated into the free energy, although there are other possible ways to generate this effect.

Secondly, the fact that the model version presented in Sec. 6.3.6 is the only one with a non-zero dynamic yield stress suggests that the original formulation with only R_{ij} and m as dynamical variables is insufficient, and therefore those dynamical equations need to be modified to generate a difference between the quasistatic steady state and the unsheared steady state. The coupling of the system to a dynamic scalar fluidity, or some other field which can act as a fluidity, has therefore been shown to be necessary to capture the desired behaviour at low strain rate. For the model to have a dynamic yield stress, there must be a dynamic scalar field introduced in addition to R_{ij} and m, which has a final value a_f such that

$$\lim_{\dot{\gamma}\to 0}\left[a_f\left(\dot{\gamma}\right)\right] \propto \dot{\gamma}, \tag{6.91}$$

with a_f independent of R_{ij} at low strain rates. There are other possibilities for the dynamics of this field than were presented in this work, and in future work, it would be interesting to see a derivation for this fluidity from the physical properties of epithelial tissue, and such a derivation would identify the fluidity with a specific process from the SPV model.

The most successful model versions presented here were all derived for $n = 4$, despite significant evidence from SPV and vertex model simulations and experimental work that a value of $n = 5$ or 6 would be more appropriate. This was done because several symmetry properties of quadrilaterals had to be used in the derivation, but the result is that some of the model versions show transitions at different values of p_0 than are seen in the SPV model. Additional interesting further work would be to attempt a derivation for the free energy accounting for cellular tilt at general n, or even specific $n \neq 4$.

Several of the model versions that have been presented show the signatures of interesting, non-trivial rheological phenomena, which have not been explored in this work. A significant number of the model versions have flow curves which appear to be non-monotonic, allowing the possibility for shear banding when simulated with heterogeneous flow allowed. This is in agreement with SPV simulations, in which distinct bands can form with low internal strain rates and a very high strain rate between them, typically at high p_0 and large strain [41, 180]. One model version also showed discontinuous shear thickening in its flow curve, which can also generate interesting phenomena under heterogeneous shear.

To summarise, we have presented an attempt at exploring the emerging field of continuum modelling of epithelial tissue. While we did not have complete success, we have presented several very good model versions, and made clear steps in the direction of constructing a fully successful continuum model of epithelial tissue. From the results presented here, there are many obvious lines of further investigation open, and it is our hope that some of these will lead to further advancement of this field.

Chapter 7

Conclusions

In this thesis, we have studied yielding transitions in a variety of soft matter systems under multiple shear protocols. Three of the models we considered, the thermal fluidity model, the SGR model and the EPM, were designed to capture the behaviour of a range of soft materials, and as such each of them could be used to model a variety of amorphous systems, such as foams, emulsions or colloidal glasses [38]. In the thermal fluidity model, we studied yielding transitions under shear startup, and characterised them based on the rate at which they happen. In the SGR model and EPM, we studied yielding transitions under a LAOS protocol, and characterised when they occur. In all three of these models, shear banding instabilities were very closely related to the yielding transition, and the development of heterogeneity within the system allowed a much faster fluidisation. The remaining set of models we considered were aimed at capturing tissue rheology. We did not study or characterise the yielding transitions in these models in as much detail, instead focussing on the derivation of a successful model. However, this section of the thesis nonetheless represents an important step forward in studying the yielding transitions seen in epithelial tissue. We now summarise the findings of each chapter in turn, and suggest avenues for further study.

7.1 Ductile and Brittle Yielding in Soft Glassy Materials

Summary of Main Results

In Ch. 3, we examined a thermal fluidity model under a shear startup protocol. We found that the system undergoes a solid to fluid yielding transition under shear, and we investigated how fast this transition is. We categorised the yielding as "ductile" or "brittle" yielding based on how quickly it occurred, although we found that it was not possible to draw a qualitative distinction based only on the yielding speed. Instead, we found that the maximum degree of shear banding was the most effective way to distinguish between ductile and brittle yielding. We found that there is a strain rate threshold, which we termed the diffusion limit, and for strain rates below this threshold, yielding is always ductile. Outside of this limit, we found that brittle yielding occurs when the magnitude of the stress drop during the yielding event is sufficiently large, and this regime corresponds to the dimensionless product $\dot{\gamma}t_w$ being above some threshold. In the brittle regime, we found that the stress drop occurred faster as a function of strain at lower strain rate and higher ageing time prior to shear.

We found that the yielding transition was closely related to a shear banding instability, and that a state of initially uniform shear was unstable to the growth of small heterogeneous shear rate perturbations while the stress is relaxing as a function of strain. In all situations, we found that heterogeneity began to grow as the stress decreased, but only in some situations (large stress drop) was it able to grow enough to have a significant impact on the system. Once the degree of banding was of the same order of magnitude as the applied strain rate, the system entered a non-linear regime in which the degree of banding grew very rapidly. This rapid growth generated locally negative shear rates, and the effect of these was to fluidise the system much more rapidly, leading to fast, brittle yielding.

We also concluded that in this model, ductile and brittle were the two extrema of a common yielding phenomenon. We found that both occurred in systems that had an overshoot of stress as a function of strain, with no need for an overhang. Rather, the only qualitative distinction between the two types of yielding was in the degree of banding that was associated with the yielding event. This conclusion is in contrast to the conclusions of Ref. [43], in which the authors proposed that brittle yielding is associated with a system that has a stress overhang as a function of strain, while ductile yielding occurs in systems with a stress overshoot.

Possible Further Work

The results presented here were also compared in Ref. [44] to similar results for athermal systems, and it was found that at low strain rate, brittle yielding is seen in all systems with a stress overshoot, regardless of the size of this overshoot. What remains unstudied, to this author's knowledge, is the transition between the behaviour observed in thermal systems and that seen in athermal systems. Some interesting further work would therefore be to examine the behaviour in a thermal model at a range of temperatures, and consider the limit as temperature goes to zero. This would hopefully elucidate how the behaviour transitions between the two extremes we have seen, and provide further understanding of the mechanism that drives this difference.

It would also be helpful to see further results on this topic from experiments and particle simulations, particularly given that the discussion remains open in the literature about the distinction between ductile and brittle yielding [181–184]. Because of the low strain rates in our study and others [43, 45] (some of which are in the limit of shear rate $\dot{\gamma} \to 0$), these experiments will be time-consuming. It would also be interesting to see further theoretical results from a wider variety of models, which would help to identify which of the features we see are related to the specific assumptions of certain models, and which represent general physical principles.

7.2 Delayed Yielding in the Soft Glassy Rheology Model in Large Amplitude Oscillatory Shear

Summary of Main Results

In Ch. 4, we considered the SGR model under a LAOS protocol, and found that in certain regimes of imposed strain amplitude and degree of sample annealing prior to shear, it showed very delayed significant yielding. We characterised the number of cycles before failure, N^*, and found that N^* follows a power law in the sample age prior to shear, t_w. As a result, we hypothesised that arbitrarily delayed yielding is possible, as is delayed yielding at any large amplitude, provided that t_w is taken large enough. We also found that N^* increases as the strain amplitude, γ_0 decreases, but found no divergence in N^* at finite amplitude.

However, we also found that there was a critical strain amplitude, $\gamma_c \approx \sqrt{2}$, below which the magnitude of the stress drop during the yielding transition effectively goes to zero. We therefore proposed that for large t_w, if $\gamma_0 > \gamma_c$, the system yields from a solid-like to a fluid-like state, while for $\gamma_0 < \gamma_c$, the system yields from a solid-like state to a slightly softer solid-like state. Regardless of the magnitude of the stress drop, however, the cycle at which the yielding occurs was determined by the typical time before an individual element yields for the first time, and this trend continues smoothly on both sides of the critical amplitude.

Possible Further Work

Some interesting further work would be to compare our results to additional experimental results. While the basic phenomenon that we observe is well established experimentally [63, 64], to this author's knowledge, no one has yet characterised the dependence of N^* on the input parameters in real materials. It would also be interesting to carry out very similar theoretical work in a stress controlled protocol, which would provide a more direct link with the existing experimental literature [63, 64].

It would also be interesting to further investigate whether or not the shear bands that form during the yielding event represent a steady state of the system or are only transient. We do not see significant decay during the time simulated, but note that we only simulate for a short window after the yielding event. It would also be interesting to simulate the system at a range of effective noise temperatures, and analyse the dependence of N^* on temperature.

7.3 Delayed Yielding in an Elastoplastic Model Under Large Amplitude Oscillatory Shear

Summary of Main Results

In Ch. 5, we considered an EPM under a LAOS protocol, and found broadly similar results to those of Ch. 4. For a range of parameters, we found the model to show delayed yielding with a significant stress drop. We were able to fit the yielding cycle, N^*, as a function of both the working temperature and the pre-quench temperature, finding $N^* = A\exp(B/T)$ and $N^* = C\exp(D/T_0)$, which predict divergences only happening as T and T_0 go to zero. As in the SGR model, we found that N^* increases as the strain amplitude decreases. In contrast to the SGR model, however, in the EPM we found that N^* diverges at a finite critical amplitude, based on the fitting function $N^* = E/(\gamma_0 - \gamma_c)$. We furthermore characterised the dependence of the fitting parameter γ_c on both T and T_0.

We found some parameter regimes for which yielding did not occur during the time we simulated for, with the system instead remaining in solid-like states. We concluded that these systems would never yield, following our analysis of the critical amplitude. We also examined analytically the athermal limit, finding a T_0-dependent critical amplitude, below which the effect of elements yielding was insufficient to have a significant impact on the state of the system. This amplitude was found to be slightly less than the value of the critical amplitude at which N^* diverges, when

extrapolated to zero temperature.

Possible Further Work

As in the SGR model, it would be interesting to compare these results to further experimental work, and to carry out additional simulations with a stress controlled protocol [63, 64]. It would also be helpful to simulate this process in the athermal limit, to better understand the limiting behaviour. Furthermore, we note that although we have made many functional fits to parameters, we are so far unable to characterise their dependence in a single function as $N^* = f(\gamma_0, T, T_0)$. Further exploration of the three-dimensional parameter space may help to map out such a function.

It would also be interesting to examine more closely the distribution of l among the elastoplastic elements before, during and after the yielding event. This would hopefully shed further light on the yielding process, and the reasons for the various functional forms.

7.4 Shape Driven Rigidity Transitions in Epithelial Tissue

Summary of Main Results

In Ch. 6, we attempted to derive a continuum model of the rheology of epithelial tissue. In doing so, we were aiming to capture a number of rheological features which were exhibited in simulations of the cellular level Voronoi model in Ref. [41]. Although we were unable to derive a model that captured all of these features, we did present some model variants that captured several key features. These included a solid-fluid transition as a function of the shape index for infinitesimal strains, a critical strain that must be applied before any stress accumulates in the system,

strain hardening at intermediate strains, a dynamic yield stress that vanishes at a different value of the target shape index to the transition value for small strains, and a stress overshoot at finite strain rate. We were not able to reproduce the precise numerical transition points from the Voronoi model, nor did we predict a stress overshoot in the quasistatic limit. Our most successful model at low strain rates also showed some unphysical behaviour at high strain rates.

While presenting several versions of a continuum model, we were able to establish key ingredients that will be necessary in any continuum model of epithelial tissue rheology in order to capture the phenomena observed in the Voronoi model [41]. The first of these was accounting for cellular tilt under strain, which in this work was done by including a hidden variable for cellular tilt, coupled to the coarse grained shape tensor. We note that other similar approaches may be successful, such as including cellular tilt as an independent dynamical variable. The second key feature is an extra dynamical field in addition to the cell shape tensor and cell elongation parameter, which is coupled to the remaining fields in such a way as to generate symmetry breaking in the quasistatic limit, so that the model's steady state is different under an applied quasistatic shear when compared to its unsheared steady state. In this work, we introduced an additional scalar fluidity with a phenomenological dynamical equation, although we again note that there may be other approaches that would satisfy this requirement. For example, recent work in Ref. [185] presents a continuum model that includes a scalar fluidity with a dynamical equation that depends on the cell perimeter, and the model also includes a dynamical equation for cell perimeter rather than elongation.

Possible Further Work

Given that we were not able to derive a continuum model capable of capturing all of the phenomena observed in Ref. [41], we hope that there will be further attempts to do so, building on the work carried out here. It would be particularly interesting to further explore the introduction of a scalar fluidity parameter, and attempt to tie

this more strongly to the physics of the system. This may well provide new insight into the precise form of its dynamical equation. It would also be interesting to see a derivation of the impact of cellular tilt carried out for general vertex number n. The work presented here relies on symmetry properties of quadrilaterals to account for cellular tilt, although some of the earlier derivations of basic concepts were presented for general n. In addition to this, a continuum model in which n is allowed to vary, either as a dynamical variable or by coupling it to other fields, may lead to some interesting discoveries. This is currently possible for the early model versions presented in this work, but not in the later versions, which are at fixed n. This approach may help to capture the behaviour that occurs at different special values of the target shape index in the Voronoi model. We also note that in Voronoi model simulations and in vivo, changes to the effective vertex number are often associated with changes to material properties [40, 72, 186].

In addition to further attempts at deriving a more advanced model, it would be interesting to see the behaviour of some of these models when heterogeneous shear is allowed. Many of the model versions presented here have features that are indicative of a system that will become banded under shear. In addition to this, Voronoi model simulations even with small numbers of cells seem to show effects that appear similar to shear banding [41,180]. Modelling these systems at a continuum level with heterogeneity would help to connect them to the length scales that are important in real systems, and to understand the effect that shear banding has in epithelial rheology. To this author's knowledge, there are no extant experimental studies of shear banding effects in epithelial tissue, and so it would also be interesting for such a study to be carried out, and to compare the results of such a study to theoretical predictions.

7.5 Closing Remarks

In this thesis, we have explored some of the rich variety and complexity of yielding transitions in amorphous materials. Our theoretical study has been motivated by existing experimental studies, and leaves open a number of testable predictions, as discussed above. We have seen that despite the range of materials, models and shear protocols considered here, yielding transitions still occur throughout, and there are a remarkable number of similarities between them which tie the separate studies together.

I hope that the work presented here will lead to further experimental and theoretical investigation, and that this leads to new insight, understanding and predictive power of yielding transitions in amorphous materials.

Bibliography

[1] P. Coussot and F. Gaulard, *Gravity flow instability of viscoplastic materials: The ketchup drip*, Physical Review E **72** (Sep, 2005) .

[2] P. J. Fellows, *Food processing technology*. Woodhead Publishing Series in Food Science, Technology and Nutrition. Woodhead Publishing, Cambridge, England, 3 ed., June, 2009.

[3] D. M. Teegarden, *Polymer chemistry*. National Science Teachers Association, Arlington, TX, Mar., 2004.

[4] I. Pastar, O. Stojadinovic, N. C. Yin, H. Ramirez, A. G. Nusbaum, A. Sawaya et al., *Epithelialization in wound healing: A comprehensive review*, Advances in Wound Care **3** (Jul, 2014) 445–464.

[5] R. J. Tetley, M. F. Staddon, D. Heller, A. Hoppe, S. Banerjee and Y. Mao, *Tissue fluidity promotes epithelial wound healing*, Nature Physics **15** (Aug, 2019) 1195–1203.

[6] S. Thowfeequ, M. J. Stower and S. Srinivas, *Epithelial dynamics during early mouse development*, Current Opinion in Genetics &amp Development **72** (Feb, 2022) 110–117.

[7] J. A. Eurell and B. L. Frappier, eds., *Dellmann's textbook of veterinary histology*. Lippincott Williams and Wilkins, Philadelphia, PA, 6 ed., May, 2006.

[8] *The IUPAC compendium of chemical terminology*, International Union of Pure and Applied Chemistry (IUPAC), Research Triangle Park, NC, Jan., 2021.

[9] D. Bonn, M. M. Denn, L. Berthier, T. Divoux and S. Manneville, *Yield stress materials in soft condensed matter*, Reviews of Modern Physics **89** (Aug, 2017) .

[10] Y. Nagase and K. Okada, *Heterogeneous behavior after yielding of solid suspensions*, Journal of Rheology **30** (Dec, 1986) 1123–1142.

[11] T. Divoux, C. Barentin and S. Manneville, *From stress-induced fluidization processes to herschel-bulkley behaviour in simple yield stress fluids*, Soft Matter **7** (2011) 8409.

[12] A. Kurokawa, V. Vidal, K. Kurita, T. Divoux and S. Manneville, *Avalanche-like fluidization of a non-brownian particle gel*, Soft Matter **11** (2015) 9026–9037.

[13] T. Gibaud, D. Frelat and S. Manneville, *Heterogeneous yielding dynamics in a colloidal gel*, Soft Matter **6** (2010) 3482.

[14] S.-F. Lin and R. S. Brodkey, *Rheological properties of slurry fuels*, Journal of Rheology **29** (Apr, 1985) 147–175.

[15] S. A. Khan, C. A. Schnepper and R. C. Armstrong, *Foam rheology: III. measurement of shear flow properties*, Journal of Rheology **32** (Jan, 1988) 69–92.

[16] D. Weaire, *The rheology of foam*, Current Opinion in Colloid &amp Interface Science **13** (Jun, 2008) 171–176.

[17] C. Hédreul and G. Frens, *Foam stability*, Colloids and Surfaces A: Physicochemical and Engineering Aspects **186** (Jul, 2001) 73–82.

[18] J. M. P. Papenhuijzen, *The role of particle interactions in the rheology of dispersed systems*, Rheologica Acta **11** (Mar, 1972) 73–88.

[19] T. Mason, *New fundamental concepts in emulsion rheology*, Current Opinion in Colloid &amp Interface Science **4** (Jun, 1999) 231–238.

[20] T. Tadros, *Fundamental principles of emulsion rheology and their applications*, Colloids and Surfaces A: Physicochemical and Engineering Aspects **91** (Nov, 1994) 39–55.

[21] A. Sun and S. Gunasekaran, *Yield stress in foods: Measurements and applications*, International Journal of Food Properties **12** (Jan, 2009) 70–101.

[22] N. Koumakis and G. Petekidis, *Two step yielding in attractive colloids: transition from gels to attractive glasses*, Soft Matter **7** (2011) 2456.

[23] G. Petekidis, D. Vlassopoulos and P. N. Pusey, *Yielding and flow of sheared colloidal glasses*, Journal of Physics: Condensed Matter **16** (Sep, 2004) S3955–S3963.

[24] K. N. Nordstrom, E. Verneuil, P. E. Arratia, A. Basu, Z. Zhang, A. G. Yodh et al., *Microfluidic rheology of soft colloids above and below jamming*, Physical Review Letters **105** (Oct, 2010) .

[25] M. Siebenbürger, M. Fuchs and M. Ballauff, *Core–shell microgels as model colloids for rheological studies*, Soft Matter **8** (2012) 4014.

[26] A. N. Gent and S. Madan, *Plastic yielding of partially crystalline polymers*, Journal of Polymer Science Part B: Polymer Physics **27** (Jun, 1989) 1529–1542.

[27] H. Sun and S.-Q. Wang, *Shear and extensional rheology of entangled polymer melts: Similarities and differences*, Science China Chemistry **55** (Feb, 2012) 779–786.

[28] M. Hermes and P. S. Clegg, *Yielding and flow of concentrated pickering emulsions*, Soft Matter **9** (2013) 7568.

[29] S. Torquato and F. H. Stillinger, *Jammed hard-particle packings: From kepler to bernal and beyond*, Reviews of Modern Physics **82** (Sep, 2010) 2633–2672.

[30] G. Parisi and F. Zamponi, *Mean-field theory of hard sphere glasses and jamming*, Reviews of Modern Physics **82** (Mar, 2010) 789–845.

[31] D. J. Durian, *Foam mechanics at the bubble scale*, Physical Review Letters **75** (Dec, 1995) 4780–4783.

[32] T. Mason, J. Bibette and D. Weitz, *Yielding and flow of monodisperse emulsions*, Journal of Colloid and Interface Science **179** (May, 1996) 439–448.

[33] J. Paredes, M. A. J. Michels and D. Bonn, *Rheology across the zero-temperature jamming transition*, Physical Review Letters **111** (Jul, 2013) .

[34] P. Olsson and S. Teitel, *Herschel-bulkley shearing rheology near the athermal jamming transition*, Physical Review Letters **109** (Sep, 2012) .

[35] R. L. Moorcroft, M. E. Cates and S. M. Fielding, *Age-dependent transient shear banding in soft glasses*, Physical Review Letters **106** (Feb., 2011) .

[36] P. Sollich, *Rheological constitutive equation for a model of soft glassy materials*, Physical Review E **58** (Jul, 1998) 738–759.

[37] S. M. Fielding, M. E. Cates and P. Sollich, *Shear banding, aging and noise dynamics in soft glassy materials*, Soft Matter **5** (2009) 2378–2382.

[38] A. Nicolas, E. E. Ferrero, K. Martens and J. Barrat, *Deformation and flow of amorphous solids: Insights from elastoplastic models*, Rev. Mod. Phys. **90** (Dec, 2018) 045006.

[39] D. Rodney, A. Tanguy and D. Vandembroucq, *Modeling the mechanics of amorphous solids at different length scale and time scale*, Modelling and Simulation in Materials Science and Engineering **19** (Nov, 2011) 083001.

[40] D. Bi, X. Yang, M. C. Marchetti and M. L. Manning, *Motility-driven glass and jamming transitions in biological tissues*, Physical Review X **6** (Apr, 2016) .

[41] J. Huang, J. O. Cochran, S. M. Fielding, M. C. Marchetti and D. Bi, *Shear-driven solidification and nonlinear elasticity in epithelial tissues*, Physical Review Letters **128** (Apr, 2022) .

[42] E. C. Bingham, *An investigation of the laws of plastic flow*, Bulletin of the Bureau of Standards **13** (Aug., 1916) 309.

[43] M. Ozawa, L. Berthier, G. Biroli, A. Rosso and G. Tarjus, *Random critical point separates brittle and ductile yielding transitions in amorphous materials*, Proceedings of the National Academy of Sciences **115** (June, 2018) 6656–6661.

[44] H. J. Barlow, J. O. Cochran and S. M. Fielding, *Ductile and brittle yielding in thermal and athermal amorphous materials*, Physical Review Letters **125** (Oct, 2020) .

[45] M. Popović, T. W. J. de Geus and M. Wyart, *Elastoplastic description of sudden failure in athermal amorphous materials during quasistatic loading*, Physical Review E **98** (Oct., 2018) .

[46] S. Suresh, *Fatigue of Materials*. Cambridge Solid State Science. Cambridge University Press, 1998.

[47] E. Anderson and T. L. Anderson, *Fracture mechanics*. CRC Press, Boca Raton, FL, 3 ed., June, 2005.

[48] H. L. Ewalds and R. J. H. Wanhill, *Fracture Mechanics*. Butterworth-Heinemann, Oxford, England, May, 1984.

[49] R. Ritchie, *Mechanisms of fatigue-crack propagation in ductile and brittle solids*, International Journal of Fracture **100** (1999) 55–83.

[50] A. A. Griffith, *VI. the phenomena of rupture and flow in solids*, Philosophical Transactions of the Royal Society of London. Series A **221** (Jan, 1921) 163–198.

[51] F. Rouyer, S. Cohen-Addad, R. Höhler, P. Sollich and S. M. Fielding, *The large amplitude oscillatory strain response of aqueous foam: Strain localization and full stress fourier spectrum*, The European Physical Journal E **27** (Nov, 2008) 309–321.

[52] B. Saint-Michel, T. Gibaud, M. Leocmach and S. Manneville, *Local oscillatory rheology from echography*, Physical Review Applied **5** (Mar, 2016) .

[53] K. Hyun, M. Wilhelm, C. O. Klein, K. S. Cho, J. G. Nam, K. H. Ahn et al., *A review of nonlinear oscillatory shear tests: Analysis and application of large amplitude oscillatory shear (LAOS)*, Progress in Polymer Science **36** (Dec, 2011) 1697–1753.

[54] R. H. Ewoldt, A. E. Hosoi and G. H. McKinley, *New measures for characterizing nonlinear viscoelasticity in large amplitude oscillatory shear*, Journal of Rheology **52** (Nov, 2008) 1427–1458.

[55] R. H. Ewoldt, P. Winter, J. Maxey and G. H. McKinley, *Large amplitude oscillatory shear of pseudoplastic and elastoviscoplastic materials*, Rheologica Acta **49** (Dec, 2009) 191–212.

[56] K. Hyun, S. H. Kim, K. H. Ahn and S. J. Lee, *Large amplitude oscillatory shear as a way to classify the complex fluids*, Journal of Non-Newtonian Fluid Mechanics **107** (Dec, 2002) 51–65.

[57] A. S. Poulos, J. Stellbrink and G. Petekidis, *Flow of concentrated solutions of starlike micelles under large-amplitude oscillatory shear*, Rheologica Acta **52** (May, 2013) 785–800.

[58] C. J. Dimitriou, R. H. Ewoldt and G. H. McKinley, *Describing and prescribing the constitutive response of yield stress fluids using large amplitude oscillatory shear stress (LAOStress)*, Journal of Rheology **57** (Jan, 2013) 27–70.

[59] F. Renou, J. Stellbrink and G. Petekidis, *Yielding processes in a colloidal glass of soft star-like micelles under large amplitude oscillatory shear (LAOS)*, Journal of Rheology **54** (Nov, 2010) 1219–1242.

[60] J. Kim, D. Merger, M. Wilhelm and M. E. Helgeson, *Microstructure and nonlinear signatures of yielding in a heterogeneous colloidal gel under large amplitude oscillatory shear*, Journal of Rheology **58** (Sep, 2014) 1359–1390.

[61] M. C. Rogers, K. Chen, M. J. Pagenkopp, T. G. Mason, S. Narayanan, J. L. Harden et al., *Microscopic signatures of yielding in concentrated nanoemulsions under large-amplitude oscillatory shear*, Physical Review Materials **2** (Sep, 2018) .

[62] M. Korhonen, K. Wallgren, A. Puisto, M. Alava and V. Vuorinen, *Shear localization in large amplitude oscillatory shear (LAOS) flows of particulate suspensions*, Physical Review Fluids **6** (Mar, 2021) .

[63] C. Perge, N. Taberlet, T. Gibaud and S. Manneville, *Time dependence in large amplitude oscillatory shear: A rheo-ultrasonic study of fatigue dynamics in a colloidal gel*, Journal of Rheology **58** (Sep, 2014) 1331–1357.

[64] T. Gibaud, C. Perge, S. B. Lindström, N. Taberlet and S. Manneville, *Multiple yielding processes in a colloidal gel under large amplitude oscillatory stress*, Soft Matter **12** (2016) 1701–1712.

[65] R. Radhakrishnan and S. M. Fielding, *Shear banding of soft glassy materials in large amplitude oscillatory shear*, Physical Review Letters **117** (Oct, 2016) .

[66] R. Radhakrishnan and S. M. Fielding, *Shear banding in large amplitude oscillatory shear (LAOStrain and LAOStress) of soft glassy materials*, Journal of Rheology **62** (Mar, 2018) 559–576.

[67] X. Trepat, L. Deng, S. S. An, D. Navajas, D. J. Tschumperlin, W. T. Gerthoffer et al., *Universal physical responses to stretch in the living cell*, Nature **447** (May, 2007) 592–595.

[68] N. Khalilgharibi, J. Fouchard, N. Asadipour, R. Barrientos, M. Duda, A. Bonfanti et al., *Stress relaxation in epithelial monolayers is controlled by the actomyosin cortex*, Nature Physics **15** (May, 2019) 839–847.

[69] E. Sadeghipour, M. A. Garcia, W. J. Nelson and B. L. Pruitt, *Shear-induced damped oscillations in an epithelium depend on actomyosin contraction and e-cadherin cell adhesion*, eLife **7** (Nov, 2018) .

[70] E. Latorre, S. Kale, L. Casares, M. Gómez-González, M. Uroz, L. Valon et al., *Active superelasticity in three-dimensional epithelia of controlled shape*, Nature **563** (Oct, 2018) 203–208.

[71] C. Malinverno, S. Corallino, F. Giavazzi, M. Bergert, Q. Li, M. Leoni et al., *Endocytic reawakening of motility in jammed epithelia*, Nature Materials **16** (Jan, 2017) 587–596.

[72] L. Atia, D. Bi, Y. Sharma, J. A. Mitchel, B. Gweon, S. A. Koehler et al., *Geometric constraints during epithelial jamming*, Nature Physics **14** (Apr, 2018) 613–620.

[73] M. Czajkowski, D. M. Sussman, M. C. Marchetti and M. L. Manning, *Glassy dynamics in models of confluent tissue with mitosis and apoptosis*, Soft Matter **15** (2019) 9133–9149.

[74] R. J. Tetley and Y. Mao, *The same but different: cell intercalation as a driver of tissue deformation and fluidity*, Philosophical Transactions of the Royal Society B: Biological Sciences **373** (Sep, 2018) 20170328.

[75] C. Bertet, L. Sulak and T. Lecuit, *Myosin-dependent junction remodelling controls planar cell intercalation and axis elongation*, Nature **429** (Jun, 2004) 667–671.

[76] R. Nagpal, A. Patel and M. C. Gibson, *Epithelial topology*, BioEssays **30** (2008) 260–266.

[77] Marieb, *Human Anat phys school ed.* Benjamin-Cummings Publishing Co., Subs. of Addison Wesley Longman, Reading, PA, 3 ed., Jan., 1995.

[78] J. Firmino, D. Rocancourt, M. Saadaoui, C. Moreau and J. Gros, *Cell division drives epithelial cell rearrangements during gastrulation in chick*, Developmental Cell **36** (Feb, 2016) 249–261.

[79] D. B. Staple, R. Farhadifar, J. C. Röper, B. Aigouy, S. Eaton and F. Jülicher, *Mechanics and remodelling of cell packings in epithelia*, The European Physical Journal E **33** (Oct, 2010) 117–127.

[80] S. Tong, N. K. Singh, R. Sknepnek and A. Kosmrlj, *Linear viscoelastic properties of the vertex model for epithelial tissues*, PLOS Computational Biology **18** (Jan, 2022) e1010135.

[81] M. Popović, V. Druelle, N. A. Dye, F. Jülicher and M. Wyart, *Inferring the flow properties of epithelial tissues from their geometry*, New Journal of Physics **23** (Mar, 2021) 033004.

[82] C. Duclut, J. Paijmans, M. M. Inamdar, C. D. Modes and F. Jülicher, *Nonlinear rheology of cellular networks*, Cells & Development **168** (Dec, 2021) 203746.

[83] M. Czajkowski, D. Bi, M. L. Manning and M. C. Marchetti, *Hydrodynamics of shape-driven rigidity transitions in motile tissues*, Soft Matter **14** (2018) 5628–5642.

[84] M. Popović, A. Nandi, M. Merkel, R. Etournay, S. Eaton, F. Jülicher et al., *Active dynamics of tissue shear flow*, New Journal of Physics **19** (Mar, 2017) 033006.

[85] W. R. Schowalter, *Mechanics of non-Newtonian fluids*. Pergamon Press, Jan., 1978.

[86] P. Leishangthem, A. D. S. Parmar and S. Sastry, *The yielding transition in amorphous solids under oscillatory shear deformation*, Nature Communications **8** (Mar, 2017) .

[87] J. Lubliner, *Plasticity Theory*. Dover Books on Engineering. Dover Publications, Mineola, NY, Feb., 2008.

[88] W.-F. Chen and D.-J. Han, *Plasticity for Structural Engineers*. J Ross Publishing, Boca Raton, FL, Apr., 2007.

[89] R. L. Huston and H. Josephs, *Practical Stress Analysis in Engineering Design, Third Edition*. Mechanical Engineering. CRC Press, Boca Raton, FL, 3 ed., Sept., 2008.

[90] R. C. Hibbeler, *Mechanics of materials*. Pearson, Upper Saddle River, NJ, 6 ed., July, 2004.

[91] M. E. Cates and S. M. Fielding, *Rheology of giant micelles*, Advances in Physics **55** (Nov, 2006) 799–879.

[92] L. D. Landau and E. M. Lifshitz, *Fluid Mechanics*. Butterworth-Heinemann, Oxford, England, 2 ed., Aug., 1987.

[93] G. K. Batchelor, *Conventions and notation*, in *An Introduction to Fluid Dynamics*, pp. xviii–xviii. Cambridge University Press, Cambridge, Feb., 2000.

[94] D. Rees, *Basic engineering plasticity*. Butterworth-Heinemann, Woburn, MA, Aug., 2006.

[95] C. Truesdell and R. Toupin, *The classical field theories*, in *Principles of Classical Mechanics and Field Theory / Prinzipien der Klassischen Mechanik und Feldtheorie*, pp. 226–858. Springer Berlin Heidelberg, 1960. DOI.

[96] W. Montijo, *Continuum theory*, in *Continuum Mechanics for Engineers, Second Edition*. CRC Press, June, 1999.

[97] F. Irgens, *Continuum Mechanics*. Springer, Berlin, Germany, Jan., 2008.

[98] C. W. Macosko, *Rheology*. John Wiley & Sons, Nashville, TN, Aug., 1994.

[99] E. J. Hemingway, H. Kusumaatmaja and S. M. Fielding, *Edge fracture in complex fluids*, Physical Review Letters **119** (Jul, 2017) .

[100] L. D. Landau, E. M. Lifshits and E. M. Lifshitz, *Fluid Mechanics: Vol 6*. Course of Theoretical Physics. Butterworth-Heinemann, Oxford, England, Jan., 1987.

[101] G. G. Stokes, *On the theories of the internal friction of fluids in motion, and of the equilibrium and motion of elastic solids*, in *Mathematical and Physical Papers*, vol. 1, pp. 75–129. Cambridge University Press. DOI.

[102] M. Cloitre, *Yielding, Flow, and Slip in Microgel Suspensions: From Microstructure to Macroscopic Rheology*. Wiley, Jan, 2011.

[103] H. A. Barnes, *A review of the slip (wall depletion) of polymer solutions, emulsions and particle suspensions in viscometers: its cause, character, and cure*, Journal of Non-Newtonian Fluid Mechanics **56** (Mar, 1995) 221–251.

[104] E. C. Bingham, *Fluidity and plasticity.* McGraw-Hill, 1922.

[105] W. H. Herschel and R. Bulkley, *Konsistenzmessungen von gummi-benzollösungen*, Kolloid-Zeitschrift **39** (Aug, 1926) 291–300.

[106] J.-F. Berret, *Transient rheology of wormlike micelles*, Langmuir **13** (Apr, 1997) 2227–2234.

[107] T. Divoux, M. A. Fardin, S. Manneville and S. Lerouge, *Shear banding of complex fluids*, Annual Review of Fluid Mechanics **48** (Jan, 2016) 81–103.

[108] O. Diat, D. Roux and F. Nallet, *Effect of shear on a lyotropic lamellar phase*, Journal de Physique II **3** (Sep, 1993) 1427–1452.

[109] J.-F. Berret, Y. Séréro, B. Winkelman, D. Calvet, A. Collet and M. Viguier, *Nonlinear rheology of telechelic polymer networks*, Journal of Rheology **45** (Mar, 2001) 477–492.

[110] P. Tapadia, S. Ravindranath and S.-Q. Wang, *Banding in entangled polymer fluids under oscillatory shearing*, Physical Review Letters **96** (May, 2006) .

[111] Y. T. Hu, *Steady-state shear banding in entangled polymers?*, Journal of Rheology **54** (Nov, 2010) 1307–1323.

[112] J. Goyon, A. Colin, G. Ovarlez, A. Ajdari and L. Bocquet, *Spatial cooperativity in soft glassy flows*, Nature **454** (Jul, 2008) 84–87.

[113] R. Besseling, L. Isa, P. Ballesta, G. Petekidis, M. E. Cates and W. C. K. Poon, *Shear banding and flow-concentration coupling in colloidal glasses*, Physical Review Letters **105** (Dec, 2010) .

[114] T. Divoux, D. Tamarii, C. Barentin and S. Manneville, *Transient shear banding in a simple yield stress fluid*, Phys. Rev. Lett. **104** (May, 2010) 208301.

[115] S. A. Rogers, D. Vlassopoulos and P. T. Callaghan, *Aging, yielding, and shear banding in soft colloidal glasses*, Phys. Rev. Lett. **100** (Mar, 2008) 128304.

[116] J. K. G. Dhont, M. P. Lettinga, Z. Dogic, T. A. J. Lenstra, H. Wang, S. Rathgeber et al., *Shear-banding and microstructure of colloids in shear flow*, Faraday Discussions **123** (Sep, 2002) 157–172.

[117] K. Kang, M. P. Lettinga, Z. Dogic and J. K. G. Dhont, *Vorticity banding in rodlike virus suspensions*, Physical Review E **74** (Aug, 2006) .

[118] S. Lerouge and P. D. Olmsted, *Non-local effects in shear banding of polymeric flows*, Frontiers in Physics **7** (Jan, 2020) .

[119] C. Grand, J. Arrault and M. E. Cates, *Slow transients and metastability in wormlike micelle rheology*, Journal de Physique II **7** (Aug, 1997) 1071–1086.

[120] P. D. Olmsted, *Perspectives on shear banding in complex fluids*, Rheologica Acta **47** (Mar, 2008) 283–300.

[121] N. Spenley, X. Yuan and M. Cates, *Nonmonotonic Constitutive Laws and the Formation of Shear-Banded Flows*, Journal de Physique II **6** (1996) 551–571.

[122] R. Benzi, T. Divoux, C. Barentin, S. Manneville, M. Sbragaglia and F. Toschi, *Unified theoretical and experimental view on transient shear banding*, Physical Review Letters **123** (Dec, 2019) .

[123] J. M. Adams, S. M. Fielding and P. D. Olmsted, *Transient shear banding in entangled polymers: A study using the rolie-poly model*, Journal of Rheology **55** (Sep, 2011) 1007–1032.

[124] E. Miller and J. P. Rothstein, *Transient evolution of shear-banding wormlike micellar solutions*, Journal of Non-Newtonian Fluid Mechanics **143** (Apr, 2007) 22–37.

[125] R. L. Moorcroft and S. M. Fielding, *Criteria for shear banding in time-dependent flows of complex fluids*, Physical Review Letters **110** (Feb, 2013) .

[126] S. Ravindranath, S.-Q. Wang, M. Olechnowicz and R. P. Quirk, *Banding in simple steady shear of entangled polymer solutions*, Macromolecules **41** (Mar, 2008) 2663–2670.

[127] P. L. DeVries and J. E. Hasbun, *A first course in computational physics*. Jones and Bartlett, Sudbury, MA, 2 ed., May, 2010.

[128] J. Crank and P. Nicolson, *A practical method for numerical evaluation of solutions of partial differential equations of the heat-conduction type*, Mathematical Proceedings of the Cambridge Philosophical Society **43** (Jan, 1947) 50–67.

[129] T. Cebeci, *Convective heat transfer*. springer, 2002.

[130] P. Niyogi, *Introduction to Computational Fluid Dynamics*. Pearson Education, Philadelphia, PA, 2006.

[131] T. Divoux, C. Barentin and S. Manneville, *Stress overshoot in a simple yield stress fluid: An extensive study combining rheology and velocimetry*, Soft Matter **7** (2011) 9335.

[132] G. P. Shrivastav, P. Chaudhuri and J. Horbach, *Yielding of glass under shear: A directed percolation transition precedes shear-band formation*, Physical Review E **94** (Oct, 2016) .

[133] T. Sentjabrskaja, P. Chaudhuri, M. Hermes, W. C. K. Poon, J. Horbach, S. U. Egelhaaf et al., *Creep and flow of glasses: strain response linked to the spatial distribution of dynamical heterogeneities*, Scientific Reports **5** (Jul, 2015) .

[134] G. Picard, A. Ajdari, L. Bocquet and F. Lequeux, *Simple model for heterogeneous flows of yield stress fluids*, Phys. Rev. E **66** (Nov, 2002) 051501.

[135] R. M. Dudley, *Uniform central limit theorems*. No. 63. Cambridge university press, 1999.

[136] N. Klingbeil, *A total dissipated energy theory of fatigue crack growth in ductile solids*, International Journal of Fatigue **25** (Feb, 2003) 117–128.

[137] S. Pradhan and B. K. Chakrabarti, *Failure due to fatigue in fiber bundles and solids*, Physical Review E **67** (Apr, 2003) .

[138] K. Binder and W. Kob, *Glassy materials and disordered solids: An introduction to their statistical mechanics (revised edition)*. World Scientific Publishing, Singapore, Singapore, Feb., 2011.

[139] D. Fenistein and M. van Hecke, *Wide shear zones in granular bulk flow*, Nature **425** (Sept., 2003) 256–256.

[140] S. M. Fielding, M. E. Cates and P. Sollich, *Shear banding, aging and noise dynamics in soft glassy materials*, Soft Matter **5** (2009) 2378–2382.

[141] J. M. Brader, T. Voigtmann, M. Fuchs, R. G. Larson and M. E. Cates, *Glass rheology: From mode-coupling theory to a dynamical yield criterion*, Proceedings of the National Academy of Sciences **106** (Aug., 2009) 15186–15191.

[142] M. Lulli, R. Benzi and M. Sbragaglia, *Metastability at the yield-stress transition in soft glasses*, Physical Review X **8** (May, 2018) .

[143] T. Divoux, D. Tamarii, C. Barentin, S. Teitel and S. Manneville, *Yielding dynamics of a herschel–bulkley fluid: a critical-like fluidization behaviour*, Soft Matter **8** (2012) 4151.

[144] M. E. Cates and P. Sollich, *Tensorial constitutive models for disordered foams, dense emulsions, and other soft nonergodic materials*, Journal of Rheology **48** (Jan, 2004) 193–207.

[145] H. J. Barlow, *Theory and simulation of shear flow instabilities in complex fluids*, Ph.D. thesis, Durham University, Jul, 2020.

[146] P. Sollich and M. E. Cates, *Thermodynamic interpretation of soft glassy rheology models*, Physical Review E **85** (Mar, 2012) .

[147] J. P. Heller and M. S. Kuntamukkula, *Critical review of the foam rheology literature*, Ind. Eng. Chem. Res. **1987** (1987) 318–325.

[148] C. Monthus and J.-P. Bouchaud, *Models of traps and glass phenomenology*, Journal of Physics A: Mathematical and General **29** (Jul, 1996) 3847–3869.

[149] S. M. Fielding, P. Sollich and M. E. Cates, *Aging and rheology in soft materials*, Journal of Rheology **44** (Mar, 2000) 323–369.

[150] M. Warren and J. Rottler, *Mechanical rejuvenation and overaging in the soft glassy rheology model*, Physical Review E **78** (Oct, 2008) .

[151] G. Yin and M. J. Solomon, *Soft glassy rheology model applied to stress relaxation of a thermoreversible colloidal gel*, Journal of Rheology **52** (May, 2008) 785–800.

[152] D. M. Hoyle and S. M. Fielding, *Age-dependent modes of extensional necking instability in soft glassy materials*, Physical Review Letters **114** (Apr, 2015) .

[153] J. D. Eshelby, *The determination of the elastic field of an ellipsoidal inclusion, and related problems*, Proceedings of the Royal Society of London. Series A. Mathematical and Physical Sciences **241** (Aug, 1957) 376–396.

[154] S. Rogers, *Large amplitude oscillatory shear: Simple to describe, hard to interpret*, Physics Today **71** (Jul, 2018) 34–40.

[155] K. S. Cho, *Large amplitude oscillatory shear*, in *Viscoelasticity of Polymers*, pp. 545–599. Springer Netherlands, 2016. DOI.

[156] G. P. Wadsworth, *Introduction to probability and random variables*. Hassell Street Press, Sept., 2021.

[157] P. Sollich, F. Lequeux, P. Hébraud and M. E. Cates, *Rheology of soft glassy materials*, Physical Review Letters **78** (Mar, 1997) 2020–2023.

[158] S. M. Fielding, *Shear banding in soft glassy materials*, Reports on Progress in Physics **77** (Oct, 2014) 102601.

[159] P. Sollich, *Soft glassy rheology*, in *Molecular Gels*, pp. 161–192. Springer-Verlag, 2006. DOI.

[160] I. Fuereder and P. Ilg, *Nonequilibrium thermodynamics of the soft glassy rheology model*, Physical Review E **88** (Oct, 2013) .

[161] M. Kaushal and Y. M. Joshi, *Analyzing aging under oscillatory strain field through the soft glassy rheology model*, The Journal of Chemical Physics **144** (Jun, 2016) 244504.

[162] G. Picard, A. Ajdari, F. Lequeux and L. Bocquet, *Slow flows of yield stress fluids: Complex spatiotemporal behavior within a simple elastoplastic model*, Physical Review E **71** (Jan, 2005) .

[163] D. Fiocco, G. Foffi and S. Sastry, *Encoding of memory in sheared amorphous solids*, Physical Review Letters **112** (Jan, 2014) .

[164] E. E. Ferrero, K. Martens and J.-L. Barrat, *Relaxation in yield stress systems through elastically interacting activated events*, Physical Review Letters **113** (Dec, 2014) .

[165] K. Chen, P. Bak and S. P. Obukhov, *Self-organized criticality in a crack-propagation model of earthquakes*, Physical Review A **43** (Jan, 1991) 625–630.

[166] J. Lin, A. Saade, E. Lerner, A. Rosso and M. Wyart, *On the density of shear transformations in amorphous solids*, EPL (Europhysics Letters) **105** (Jan, 2014) 26003.

[167] K. Martens, L. Bocquet and J.-L. Barrat, *Spontaneous formation of permanent shear bands in a mesoscopic model of flowing disordered matter*, Soft Matter **8** (2012) 4197.

[168] A. Nicolas, K. Martens and J.-L. Barrat, *Rheology of athermal amorphous solids: Revisiting simplified scenarios and the concept of mechanical noise temperature*, EPL (Europhysics Letters) **107** (Aug, 2014) 44003.

[169] M. Popović, T. W. J. de Geus, W. Ji and M. Wyart, *Thermally activated flow in models of amorphous solids*, Physical Review E **104** (Aug, 2021) .

[170] P. Hébraud and F. Lequeux, *Mode-coupling theory for the pasty rheology of soft glassy materials*, Physical Review Letters **81** (Oct, 1998) 2934–2937.

[171] V. V. Bulatov and A. S. Argon, *A stochastic model for continuum elasto-plastic behavior. i. numerical approach and strain localization*, Modelling and Simulation in Materials Science and Engineering **2** (Mar, 1994) 167–184.

[172] A.-K. Classen, K. I. Anderson, E. Marois and S. Eaton, *Hexagonal packing of drosophila wing epithelial cells by the planar cell polarity pathway*, Developmental Cell **9** (Dec, 2005) 805–817.

[173] A. R. Harris, L. Peter, J. Bellis, B. Baum, A. J. Kabla and G. T. Charras, *Characterizing the mechanics of cultured cell monolayers*, Proceedings of the National Academy of Sciences **109** (Sep, 2012) 16449–16454.

[174] A. Hernandez and M. C. Marchetti, *Poisson-bracket formulation of the dynamics of fluids of deformable particles*, Physical Review E **103** (Mar, 2021) .

[175] S. Boyd and L. Vandenberghe, *Convex Optimization*. Cambridge University Press, Cambridge, England, Mar., 2004.

[176] M. P. Allen and D. J. Tildesley, *Computer Simulation of Liquids*. Oxford University Press, 08, 2022.

[177] E. Bitzek, P. Koskinen, F. Gähler, M. Moseler and P. Gumbsch, *Structural relaxation made simple*, Physical Review Letters **97** (Oct, 2006) .

[178] B. Beavis and I. Dobbs, *Optimisation and stability theory for economic analysis*. Cambridge University Press, Cambridge, England, Feb., 1990.

[179] W. Karush, *Minima of functions of several variables with inequalities as side conditions*, in *Traces and Emergence of Nonlinear Programming*, pp. 217–245. Springer Basel, July, 2013. DOI.

[180] M. Merkel, *From cells to tissues: Remodeling and polarity reorientation in epithelial tissues*, Ph.D. thesis, der Fakultät Mathematik und Naturwissenschaften der Technischen Universität Dresden, Dec, 2014.

[181] D. Richard, C. Rainone and E. Lerner, *Finite-size study of the athermal quasistatic yielding transition in structural glasses*, The Journal of Chemical Physics **155** (Aug, 2021) 056101.

[182] M. Ozawa, L. Berthier, G. Biroli and G. Tarjus, *Rare events and disorder control the brittle yielding of well-annealed amorphous solids*, Physical Review Research **4** (Jun, 2022) .

[183] J. Pollard and S. M. Fielding, *Yielding, shear banding, and brittle failure of amorphous materials*, Physical Review Research **4** (Oct, 2022) .

[184] S. Rossi, G. Biroli, M. Ozawa, G. Tarjus and F. Zamponi, *Finite-disorder critical point in the yielding transition of elasto-plastic models*, .

[185] S. M. Fielding, J. O. Cochran, J. Huang, D. Bi and M. C. Marchetti, *Constitutive model for the rheology of biological tissue*, Oct., 2022. 10.48550/ARXIV.2210.02893.

[186] R. Etournay, M. Popović, M. Merkel, A. Nandi, C. Blasse, B. Aigouy et al., *Interplay of cell dynamics and epithelial tension during morphogenesis of the drosophila pupal wing*, eLife **4** (Jun, 2015) .

[187] P. Coussot, Q. D. Nguyen, H. T. Huynh and D. Bonn, *Viscosity bifurcation in thixotropic, yielding fluids*, Journal of Rheology **46** (May, 2002) 573–589.

[188] G. Marrucci and N. Grizzuti, *The free energy function of the doi-edwards theory: Analysis of the instabilities in stress relaxation*, Journal of Rheology **27** (1983) 433–450.

[189] W. H. Press, S. A. Teukolsky, W. T. Vetterling and B. P. Flannery, *Numerical Recipes in C*. Cambridge University Press, 2 ed., 2002.

[190] P. K. Jaiswal, I. Procaccia, C. Rainone and M. Singh, *Mechanical yield in amorphous solids: A first-order phase transition*, Physical Review Letters **116** (Feb, 2016) .

[191] C. Schuh, T. Hufnagel and U. Ramamurty, *Mechanical behavior of amorphous alloys*, Acta Materialia **55** (Jul, 2007) 4067–4109.

[192] T. Gibaud, C. Barentin and S. Manneville, *Influence of boundary conditions on yielding in a soft glassy material*, Physical Review Letters **101** (Dec, 2008) .

[193] T. Gibaud, C. Barentin, N. Taberlet and S. Manneville, *Shear-induced fragmentation of laponite suspensions*, Soft Matter **5** (2009) 3026.

[194] P. Kollmannsberger and B. Fabry, *Linear and nonlinear rheology of living cells*, Annual Review of Materials Research **41** (Aug, 2011) 75–97.

[195] Y. Fujii, Y. Ochi, M. Tuchiya, M. Kajita, Y. Fujita, Y. Ishimoto et al., *Spontaneous spatial correlation of elastic modulus in jammed epithelial monolayers observed by AFM*, Biophysical Journal **116** (Mar, 2019) 1152–1158.

[196] R. Farhadifar, J.-C. Röper, B. Aigouy, S. Eaton and F. Jülicher, *The influence of cell mechanics, cell-cell interactions, and proliferation on epithelial packing*, Current Biology **17** (Dec, 2007) 2095–2104.

[197] J. Ranft, M. Basan, J. Elgeti, J.-F. Joanny, J. Prost and F. Jülicher, *Fluidization of tissues by cell division and apoptosis*, Proceedings of the National Academy of Sciences **107** (Nov, 2010) 20863–20868.

[198] T. Bittig, O. Wartlick, A. Kicheva, M. González-Gaitán and F. Jülicher, *Dynamics of anisotropic tissue growth*, New Journal of Physics **10** (Jun, 2008) 063001.

[199] C. Blanch-Mercader, J. Casademunt and J. F. Joanny, *Morphology and growth of polarized tissues*, The European Physical Journal E **37** (May, 2014) .

[200] P. Recho, J. Ranft and P. Marcq, *One-dimensional collective migration of a proliferating cell monolayer*, Soft Matter **12** (2016) 2381–2391.

[201] W.-T. Yeh and H.-Y. Chen, *Hydrodynamics of stratified epithelium: Steady state and linearized dynamics*, Physical Review E **93** (May, 2016) .

[202] M. Paoluzzi, L. Angelani, G. Gosti, M. C. Marchetti, I. Pagonabarraga and G. Ruocco, *Alignment interactions drive structural transitions in biological tissues*, Physical Review E **104** (Oct, 2021) .

[203] G. Picard, A. Ajdari, F. Lequeux and L. Bocquet, *Elastic consequences of a single plastic event: A step towards the microscopic modeling of the flow of yield stress fluids*, The European Physical Journal E **15** (Nov, 2004) 371–381.

[204] O. Gonzalez and A. M. Stuart, *A First Course in Continuum Mechanics*. Cambridge University Press, Jan, 2001, 10.1017/cbo9780511619571.

[205] A. Davey, *The growth of taylor vortices in flow between rotating cylinders*, Journal of Fluid Mechanics **14** (Nov, 1962) 336–368.

[206] B. Evans and D. L. Kohlstedt, *Rheology of rocks*, in *AGU Reference Shelf*, pp. 148–165. American Geophysical Union, Mar, 2013. DOI.

[207] M. Ohnaka, *The physics of rock failure and earthquakes*. Cambridge University Press, Cambridge, England, Apr., 2013.

[208] C. Derec, G. Ducouret, A. Ajdari and F. Lequeux, *Aging and nonlinear rheology in suspensions of polyethylene oxide–protected silica particles*, Physical Review E **67** (Jun, 2003) .

[209] W. Letwimolnun, B. Vergnes, G. Ausias and P. Carreau, *Stress overshoots of organoclay nanocomposites in transient shear flow*, Journal of Non-Newtonian Fluid Mechanics **141** (Feb, 2007) 167–179.

[210] T. Divoux, C. Barentin and S. Manneville, *Stress overshoot in a simple yield stress fluid: An extensive study combining rheology and velocimetry*, Soft Matter **7** (2011) 9335.